Quantum transport in Dirac materials and their heterostructures

Muhammad Zubair

A Thesis

in

The Department

of

Physics

Presented in Partial Fulfillment of the Requirements

for the Degree of

Doctor of Philosophy (Physics) at

Concordia University

Montréal, Québec, Canada

March 2022

CONCORDIA UNIVERSITY

School of Graduate Studies

This is to certify that the thesis prepared

By: **Muhammad Zubair**

Entitled: **Quantum transport in Dirac materials and their heterostructures**

and submitted in partial fulfillment of the requirements for the degree of

Doctor of Philosophy (Physics)

complies with the regulations of this University and meets the accepted standards with respect to originality and quality.

Signed by the Final Examining Committee:

_____ Chair
Dr. Dmitry Korotkin

_____ External Examiner
Dr. João Milton Pereira Junior

_____ Examiner
Dr. Pablo Bianucci

_____ Examiner
Dr. Saurabh Maiti

_____ Supervisor
Dr. Panagiotis Vasilopoulos

Approved by _____
Valter Zazubovits, Chair
Department of Physics

_____ 2022

_____
Andre Roy, Dean
Faculty of Arts and Science

Abstract

Quantum transport in Dirac materials and their heterostructures

Muhammad Zubair, Ph.D.

Concordia University, 2022

This thesis explores the transport and optical properties of novel two dimensional (2D) materials such as graphene or graphene nanoribbons, transition metal dichalcogenides (TMDCs), and some heterostructures based on them. To study these systems, we use a tight-binding, one-particle Hamiltonian and take its low-energy limit near the Dirac points. Diagonalizing the Hamiltonian gives the eigenvalues and eigenvectors which we use to evaluate linear response formulas for the conductivities in various systems, e.g., bilayer TMDCs in the presence or absence of magnetic and electric fields. We study in detail physical properties such as the quantum Hall effect, the quantum spin-Hall effect, and optical properties for one-body collisions of electrons with, e.g., impurities. We also consider heterostructures, made by encapsulating graphene monolayers on suitable substrates, e.g., TMDCs. In addition, we discuss the influence of an off-resonant light on valley-controlled transport in such systems and predict, among other things, topological phase transitions induced by such a light. Finally, we address the optical response of armchair graphene nanoribbons (AGNRs) as a function of the photon frequency. Also, we assess the influence of elastic scattering by impurities on the diffusive (Drude-type) contribution to the current in these nanoribbons.

Acknowledgments

I dedicated this thesis to my father Naseer Ahmad, May Allah grant him eternal peace in paradise.

Contents

List of Figures

List of Tables

List of Publications

(1) **Quantum magnetotransport in bilayer MoS_2: influence of perpendicular electric field**

M. **Zubair**, M. Tahir, P. Vasilopoulos and K. Sabeeh, Phys. Rev. B, **96**, 045405 (2017).

(2) **Magneto-optical properties of bilayer transition metal dichalcogenides**

M. **Zubair**, M. Tahir, and P. Vasilopoulos, Phys. Rev. B, **98**, 155402 (2018).

(3) **Transport in armchair graphene nanoribbons and in ordinary waveguides**

M. **Zubair**, M. Bahrami, and P. Vasilopoulos, J. Appl. Phys. **126**, 164304 (2019).

(4) **Influence of interface induced valley-Zeeman and spin-orbit couplings on transport in heterostructures of graphene on WSe_2**

M. **Zubair**, P. Vasilopoulos, and M. Tahir, Phys. Rev. B, **101**, 165436 (2020).

(5) **Valley-controlled transport in graphene/ WSe_2 heterostructures under an off-resonant polarized light**

M. **Zubair**, P. Vasilopoulos, and M. Tahir, Phys. Rev. B, submitted (2021).

(6) **N. B.** We mark the references above by (x), $x = 1 - 6$, to distinguish them from those at the end of the thesis, marked by $[x]$, $x = 1 - 281$.

Chapter 1

Novel two-dimensional materials

A wide variety of materials, ranging from graphene to topological insulators were found to have a common low-energy fermionic dispersion that resembles massless Dirac particles, rather than the usual free particle parabolic dispersion of the Schrödinger type, conventionally referred to as Schrödinger fermions. Materials having this unifying emergent Dirac fermion spectral character are now referred to as Dirac materials. In general, they have a linear electron and hole dispersion near the Dirac point.

Since the discovery of graphene, Dirac materials have become a very hot topic in solid state physics both theoretically and experimentally because of their prominent mechanical, optical, electrical and magnetic properties. Recently, graphene has attracted a lot of attention of the scientific community in the field of spintronics, due to its large electronic mobility, low spin-orbit coupling (SOC), negligible hyperfine interaction and gate unability. For a clear example, it has been proven that graphene exhibits a longest spin relaxation length even measured at room temperature. So, in this quest, the field has moved beyond graphene in searching for new 2D materials (e.g., silicene, MoS_2 and WSe_2 etc.) including their van der Waals heterostructures and nanoribbons. The novel heterostructures provide a testbed for inducing new functionalities in layered materials, e.g., proximity induced SOC in graphene on transition metal dichalcogenides (TMDCs) and rendering them appropriate for the emerging fields of spintronics and valleytronics.

In this chapter we provide an overview of these new 2D materials. While some of them are ahead from one another, from the point of view of technological applications and new emerging

fields, such as spintronics and valleytronics, graphene is not a suitable candidate for spintronics applications due to its vanishing gap. In contrast, TMDCs, due to their large band gaps and giant SOC are suitable for these fields and very promising. Further, a large SOC in graphene can be induced by placing it on TMDCs and thus making it useful in these fields.

1.1 Graphene

The study of two-dimensional (2D) materials begun with the first theoretical model of a 2D sheet of sp^2 bonded carbon atoms by Wallace in 1947 [1] who investigated the relevant electronic band structure. After that, a 2D sheet of carbon atoms was prepared by using the method of chemical reduction of exfoliated graphite [2] in 1962. In the late 60s, it was observed on a platinum surface as a disordered structure in ultrahigh vacuum [3]. In 2004, after a long time, Geim and Novoselov experimentally isolated a single layer of graphite, namely graphene, and investigated its electronics properties [4]. To isolate such a single layer, Novoselov and his coworkers pulled off graphene from graphite by applying the scotch-tape method. In this regard, they were awarded the Nobel prize in 2010 for their groundbreaking discovery of 2D graphene [5]. After that, the family of 2D materials has grown appreciably.

The carbon atoms in graphene are arranged in 2D hexagonal lattice. Interestingly, graphene has attracted the intensive research attention from both the academia and industry due to its rich physics [6, 7, 8] and high mobility [9]. Furthermore, it is a fundamental building block for manufacturing various types of well-known allotropes such as 3D graphite, 1D carbon nanotubes, and 0D fullerene as shown in Fig. 1.1. Due to a strong interest in graphene, publications have been approximated as 4×10^4 in number or more from 2004 up till now [10]. Further, books on graphene have also been published which show that the field has matured to some extent [11]. Moreover, graphene has extraordinary properties such as high surface area, high Young's modulus, 2.3 % absorption in the white light spectrum and excellent thermal conductivity. Due to these important properties, graphene carries tremendous potential as material for energy storage and generation [12, 13, 14], hybrid materials [15, 16], chemical sensors [17, 18], DNA sequencing [19, 20, 21], and high-speed electronics [22] and optical [12] devices. Some potential applications of feasible uses of graphene

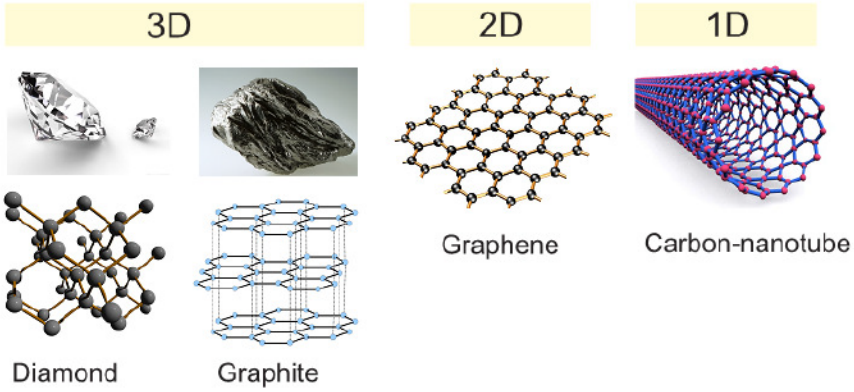

Figure 1.1: The different allotropes of carbon. The idea is taken from Ref. [23].

are given below:

1.1.1 Solar cells

The materials that have the ability to absorb sunlight are used to manufacture solar cells. Before the invention of graphene, the electrodes were prepared by using indium tin oxide (ITO). This material was very costly. Nowadays, solar cells based on graphene, in which graphene's sheets are used as electrodes, have also been suggested. They might be quite cheap as compared to ITO [24].

1.1.2 Graphene-based display screens

In Ref. [25], it was claimed that due to the large conductivity of graphene, we can use it as transparent sheet. Because of this property, graphene is used in organic light-emitting diodes (OLED), which have a wider use in display screens. Earlier material that was used in OLED was indium, which is costly and poisonous. Accordingly, replacing it with graphene will reduce the cost remarkably. Further, elastic screens can also be designed using graphene [26].

1.1.3 Transistors based on graphene

Graphene has linear dispersion and zero gap at the Charge Neutrality Point (CNP) or Dirac point. Accordingly, its mobility is found to be 4×10^4 cm^2/ (V.s) [27] at room temperature, whereas it is 2×10^5-10^6 cm^2/(V.s) at low temperature [28, 29]. Thus, it can be used in high-mobility nanoelectronics. For instance, field-effect Transisters (FET) based on graphene have been manufactured

recently [30, 22].

1.2 Hexagonal Boron nitride

Hexagonal Boron nitride (hBN) has been found to consist of a similar lattice structure as that found for the carbons of graphene in that it consists of equal numbers of boron and nitrogen atoms. Sheets of hBN are composed of alternating boron and nitrogen atoms in a honeycomb arrangement consisting of sp^2-bonded 2D layers. This structure means that hBN powder is traditionally used as a lubricant [31]. The pristine hBN sheets are intrinsically insulators or wide band gap semiconductors (approximately 5.9 eV) [32]. Because of its good electrical insulation property, hBN has been applied as a charge leakage barrier layer for use in electronic equipment [33]. It can also be used as a host for single photon emitters in the infrared and ultraviolet regions of the spectrum [34] with potential applications in quantum communication and quantum information science.

1.3 Silicene

The silicon analog of graphene, called silicene, is a new 2D material that has been predicted to be stable [35] and has currently been synthesized on a Ag(111) or MoS_2 surface [36, 37]. Though there is some controversy as to how its free-standing version can be really synthesized [38], it has attracted a great deal of attention [39, 40, 41] because, contrary to graphene, it has a strong spin-orbit interaction (SOI). In addition, the Dirac cones in silicene are similar to those of graphene. This similarity results from the fact that carbon and silicon belong to the same column in the periodic table of elements. The strong SOI of silicene is predicted to open a gap with a width of approximately 1.55 meV [39] between the low-energy Dirac-like cones, which is appropriate for the observation of the quantum spin-Hall effect. It has also been predicted that the created gap can be tuned [40] by applying an external electric field E_z perpendicular to the silicene sheet. The tunability of the band gap is a consequence of the buckled structure, with one of the two sublattices of the honeycomb lattice shifted vertically with respect to the other.

1.4 Transition metal dichalcogenides

During the past few years, two-dimensional materials have attracted a lot of attention of the scientific community due to their peculiar electronic properties. Further, they are easy to produce and have potential applications in future nanoelectronic devices [42]. In this regards, graphene has been widely studied, because it has a simple structure but very rich physics. However, it has limited application in the fabrication of logical circuits and optoelectronic devices due to its zero band gap. Therefore, other 2D materials have been grown for fulfilling this gap e.g., transition metal dichalcogenides (TMDCs) which were discovered recently [43]. They constitute another family of 2D materials with large direct band gap [44, 45, 46] and giant intrinsic SOC [43, 47]. The general chemical formula of TMDCs is MX_2 in which hexagonal layer of transition metal atoms (M= Mo, W) is sandwitched between the two layers of chalcogenides atoms (X=S, Se). This particular combination of layers of different atoms forms the hexagon with M and X_2 atoms located at the alternating corners as can be seen in Fig. 1.2.

Surprisingly, 2D crystals of TMDCs show often very different properties from those of their 3D counterparts [45, 44]. Further, TMDCs are also shaped into mono and few layers. Recently, it has been demonstrated by experiment that multilayer TMDCs are indirect-gap semiconductor while monolayer TMDCs are direct-gap ones [45]. The value of direct band gap is in the visible frequency range. This feature is very useful for optoelectronic's applications e.g., light-emiting diodes. Recently, a transistor was also fabricated based on a MoS_2 monolayer, which is an extensively studied material within the family of TMDCs, with 200 $cm^2/(V.s)$ mobility value at room temperature [48]. Moreover, MoS_2 has been used as a main component in various nanoelectronic devices, such as amplifiers, photodetectors, thin film transistors, and logical circuits [48, 49, 50, 51], due to its excellent electronic properties. In addition, several other remarkable properties of TMDCs monolayers have been investigated theoretically and experimentally [52, 53, 54, 55, 56, 57, 58], e.g., magneto-optical spectra and magnetotransport.

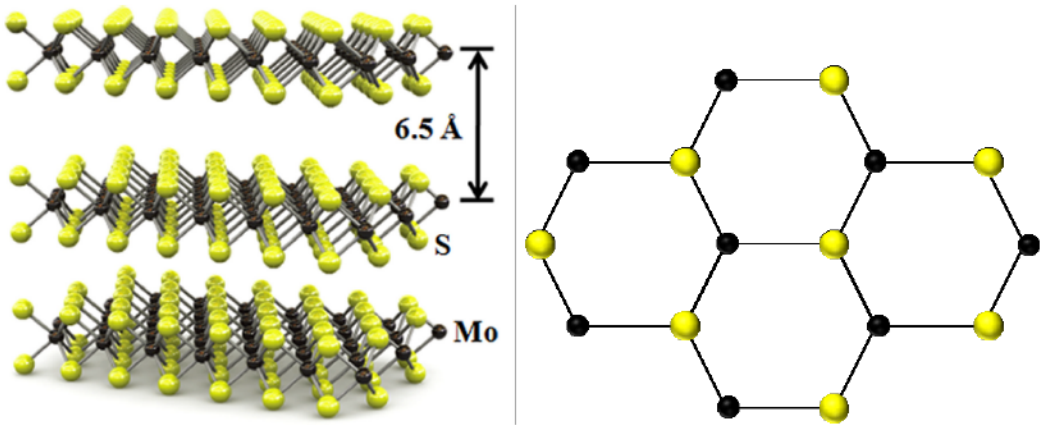

Figure 1.2: Left panel: The atomic structure of layered MoS_2. Different sheets of MoS_2 are composed of three atomic layers S-Mo-S, where Mo and S are covalently bonded. Right panel: A top view of the honeycomb lattice, emphasizing the inversion symmetry breaking.

1.5 Novel van der Waals heterostructures

In reality, it is a demanding task to create the one conclusive material by combining the different ingredients. However, we have some successful examples such as composite materials and III-V heterostructures that revolutionized many aspects of our lives. But, we still required such strategies that solve the problem for mixing and matching crystals of different properties to create the combinations with predetermined attributes and functionalities. In this regard, 2D materials play their role for creating the heterostructures with a variety of properties. After the discovery of graphene, the family of 2D materials with a wide range of properties is expanding day by day. Further, the family of 2D materials comprises of insulators (e.g., hexagonal boron nitride (hBN)), semiconductors (e.g., MoS_2), and metals (e.g., $NbSe_2$). Also, experiments reveal that these materials are stable at ambient conditions. Moreover, the study of familiar phenomena, like superconductivity and ferromagnetism, lead to many thought-provoking questions due to the lack of long range order.

Furthermore, a plethora of exciting phenomena appears when we start to assemble the crystals in one stack. When graphene interacts with hBN that combination opens the possibility to measure the Hofstadter butterfly effect and topological currents in such a system. Also, designer heterostructures give rise to the proximity effect that allows the study of tunneling and drag effects. The optically active herterostructures can be created by using the semiconducting monolayers. The devices such as tunneling transistors, resonant tunneling diodes, and light-emitting diodes based on novel van der

waals heterostructures have also been started to emerge.

1.5.1 Modification of spectrum of graphene on hBN

Graphene on hBN leads to the formation of Moiré patterns where electrons feel the periodic scattering potential. This leads to the reconstruction of the electronic spectrum at the wave vectors which are determined by the periodicity of the Moiré structure. This modification of the energy spectrum has been observed first in scanning tunneling microscopy [62] and later in transport [63, 64, 65] and capacitance measurements [66]. Further, secondary Dirac points appear in both the conduction and valence bands [67]. The energy range in which reconstruction of the spectrum occurs is estimated to be about 50 meV, which can be determined by the strength of the van der Waals interaction between graphene and hBN. Moreover, such a reconstruction creates an asymmetry between graphene's sublatices and leads to the opening of a gap in the spectrum.

1.5.2 Devices based on plasmon

Plasmons in graphene have attracted a lot of attention because the plasmonic frequency [68] can be tuned by changing the carrier concentration. Also, plasmonic as well as phonon polaritonic properties have been studied in other 2D materials. For example, hBN has polar dielectric properties and thus supports surface phonon polaritons with very low optical losses [69].

Van der Waals heterostructures provide a playground to examine a number of new polaritonic effects. Scattering of graphene plasmons by impurities can be eliminated when graphene is encapsulated with hBN in comparison with bare graphene [70]. Further, hybridization between the plasmonic modes of different layers of graphene can be achieved by sandwiching the multilayers of graphene separated by hBN spacers. It is further controlled by the external gate voltage [71]. Also, it is possible in such heterostructure to enter a regime on which a plasmonic polariton in graphene and a phonon polariton in hBN coexist. A new collective mode, called plasmon-phonon polariton [72, 73], has been formed due to the strong coupling between these two. Both amplitude and wavelength can be controlled by gating graphene.

Moreover, the formation of Moiré patterns in aligned graphene/hBN heterostructure further modifies the graphene-plasmon spectrum. Zone folding results in secondary Dirac points [67],

which allow a new type of vertical transitions. Such transitions are immediately reflected in the modified damping factor, which exhibits a maximum at such Fermi energies [74]. It has also been predicted that new plasmonic modes, with carrier density dependence characteristic of parabolic electronic bands, should appear in the vicinity of van Hove singularities in the reconstructed spectrum [74].

1.5.3 Tunneling devices

Graphene can be combined with semiconductor and insulating 2D crystals to create a tunnel junction [75]. The use of hBN as a tunneling barrier is particularly attractive due to its large band gap ($\approx$ 6 eV), low number of impurity states within the barrier, and high breakdown field. Because the position of the Fermi energy and the DOS in graphene can be varied by external gate, the same applies for the tunneling current, which allows such structures to be used as field effect tunneling transistors (FETTs) [76].

Furthermore, the highest on-off ratio for FETTs can be achieved if the changes in the Fermi energy in graphene are comparable with the gap in the tunneling barrier if hBN is replaced with WS_2 (on-off ratio of 10^6) [77] or MoS_2 (on-off ratio of 10^3 to 10^4, probably because of the presence of impurity bands) [76]. In addition to logic applications, tunneling in van der Waals heterostructures was exploited for memory devices [78] with a floating gate, logic circuits [79], radio-frequency oscillators [80], and resonant tunneling diodes [81].

1.5.4 Van der Waals heterostructures for photovoltaic applications

Combinations of graphene, as a channel material, and TMDCs, as light-sensitive material, allow the creation of simple and efficient phototransistors [82]. Combining materials with different work functions can lead to photoexcited electrons and holes accumulated in different layers, giving rise to indirect excitons e.g., as has been observed for the pairs MoS_2/WSe_2 [83] and $MoSe_2$/WSe_2 [84]. Such excitons typically have long lifetimes, and their binding energy could be tuned by controlling the distance between the semiconductor layers. Thus, the more efficient photovoltaic devices can be created by combining thin layers of TMDCs [85] or metal chalcogenides [86] with graphene.

1.5.5 Light-emitting diodes

The p-n junctions described above can be operated in the regime of electrical injection of the charge carriers, which leads to electron-hole recombination and light emission [87]. However, such arrangement is limited by the requirements of synthesizing p- and n-type materials, which have not yet been demonstrated for all 2D crystals.

A more straightforward arrangement is the carrier injection from highly conductive transparent electrodes directly into the 2D material in a vertical structure. However, such a scheme requires careful control of the dwell time of the injected electrons and holes in the semiconductor crystal, because photoemission is a slow process in comparison with the characteristic time required to penetrate the junction between graphene and the semiconductor. Thus, two to three layers of hBN have been used [88] to increase the time electrons and holes spend inside the monolayer TMDC, allowing their radiative recombination. The quantum efficiency in devices based on WSe_2 increases with increasing temperature and injection current, reaching 20% at room temperature [89].

1.6 Experimental methods to synthesis the 2D materials

Mechanical and liquid-phase exfoliations are two common methods used to separate individual sheets from stacked 2D layered crystals by breaking the weak van der Waals bonds between the layers. The sheets with perfect crystalline structures can be obtained by mechanical exfoliation [4, 90, 44]. Thus, these sheets are used to explore the intrinsic properties of the materials. However, yield from this method is very low.

Liquid-phase exfoliation creates dispersions of 2D layered materials in various solvents or aqueous surfactant solutions with the assistance of sonication. Here sonication results in the exfoliation of the layered crystals into single-layer and multilayer sheets stabilized by interactions with the solvent or a surfactant. Such dispersion can easily form films by vacuum filtration with thicknesses that range from nanometers to tens of micrometers. Compared with mechanical exfoliation, solution-based exfoliation is an efficient method for producing large quantities of layered materials [91, 92, 93]. Although it should be noted that control of the number of layers and the lateral size is difficult, such liquid exfoliation methods also allow easy functionalization of the individual sheets

[94, 95] and the formation of novel composite materials [91, 92, 96].

In addition to the above solution-based exfoliation, wet chemical reactions were also explored as a means to synthesize 2D materials sheets. For instance, few-layer BN sheets using the reaction between boric acid with urea at 900 °C under an N_2 atmosphere has been synthesized [97].

In contrast with either the exfoliation methods or wet chemical reactions, in which control of the layer number and the lateral size of 2D materials sheets is difficult, a dry chemical vapor deposition (CVD) method has also been extensively explored. The aim was to synthesize 2D layered materials on a large scale [98, 99] with the promise of fine control over the number of layers and the crystalline structures.

Surface segregation like the CVD method is another feasible method for the large-scale synthesis of graphene. It has the potential to control the number of graphene layers [100, 101] and hence was also used to synthesize h-BN layers [102]. Further, because the CVD growth of h-BN films unusally involves explosive and toxic chemical and gases, this kind of surface segregation approach is much simpler and safe.

1.7 Organization of the thesis

The thesis consists of 7 chapters including this introductory one. Chapters 2 - 6 have published works and their corresponding additional materials are included as appendices at the end of the dissertation. Concluding remarks as well as future directions are given in the last chapter. To further orient the reader, a brief overview regarding each chapters is provided below.

- Chapter 2 presents very briefly the material of our published work **"quantum magnetotransport in bilayer MoS_2: influence of perpendicular electric field"**, Ref. (1). Bilayer MoS_2 has a four-fold spin and valley degeneracies intrinsically. Therefore, it has limited applications in the newly emerging fields of spintronics and valleytronics. To make it useful in these areas, we proposed in this study that a significant amount of spin and valley splittings can be achieved by applying to it perpendicular electric and magnetic fields. Also, we studied its spin and valley-resolved Hall and longitudinal conductivities. We pointed out that such a

transport study could be pertinent to making Hall effect-based sensing devices, e.g., temperature or pressure sensors etc. This very brief chapter, which is not part of the thesis, is included to only show how it naturally lead to the studies of chapters 3 - 6.

- In chapter 3, we present the results of the manuscript **"magneto-optical properties of bilayer transition metal dichalcogenides"**, Ref. (2). In this work, we assessed the spin and valley dependent optical response of bilayer TMDCs by evaluating the conductivity expressions in the linear response regime in the presence and absence of electric and magnetic fields. We found that this optical response could be very useful in designing optical devices, such as LEDs etc., based on the spin and valley degrees of freedom.

- In chapter 4, we will address transport in graphene/ WSe_2 heterostructures. We will discuss the effect of different types of symmetry breaking terms, such as band gap and SOC etc., on the electronic dispersion as well as on ac and dc transport in this heterostructure. We will show that these symmetry breaking terms can be obtained from a tight-binding model. In addition, we study screening effects by taking into account the relaxation time for short- and long-range impurity potentials on the diffusive contribution to the current. The findings of this chapter **"Influence of interface induced valley-Zeeman and spin-orbit couplings on transport in heterostructures of graphene on WSe_2"** has been published in Ref. (3).

- Chapter 5 comprises the results of our submitted manuscript **"Valley-controlled transport in graphene/ WSe_2 heterostructures under an off-resonant polarized light"**, Ref. (5). In this work, we predict that we can induce the valley splitting by shining an off-resonant, circularly polarized light on the heterostructure. Also, we studied the effect of such a light on the transport coefficients, namely the Hall and diffusive conductivities, which can be used in building devices like valley valves, valley filters, etc.

- In the second-to-last chapter, we present the findings of our published work **"Transport in armchair graphene nanoribbons and in ordinary waveguides"**, Ref. (4). We found a transition from a semiconducting to a metallic state in armchair graphene nanoribbons as a function of the number of rows contrary to ordinary waveguides where no such transitions

exist. Also, we discussed the effect of the number of rows on the optical transport coefficients which are useful for the development of infrared photodetectors.

Chapter 2

Quantum magnetotransport in bilayer MoS_2: Influence of perpendicular electric field

2.1 Abstract

We first derive the energy dispersion of bilayer MoS_2 in the presence of a perpendicular electric field E_z. We show that the band gap and layer splitting can be controlled by the field E_z. Away from the k point, the intrinsic SOC splitting increases in the conduction band but is weakly affected in the valence band. We then analyze the band structure in the presence of a perpendicular magnetic field B and the field E_z, including spin and valley Zeeman terms, and evaluate the Hall and longitudinal conductivities. We discuss the numerical results as functions of the fields B and E_z for finite temperatures. The field B gives rise to a significant spin splitting in the conduction band, to a beating in the Shubnikov-de Haas (SdH) oscillations when it's weak, and to their splitting when it's strong. The Zeeman terms and E_z suppress the beating and change the positions of the beating nodes of the SdH oscillations at low B fields and enhance their splitting at high B fields. Similar beating patterns are observed in the spin and valley polarizations at low B fields. Interestingly, a 90% spin polarization and a 100% square-wave-shaped valley polarization are observed at high

B fields. The Hall-plateau sequence depends on E_z. These findings may be pertinent to future spintronic and valleytronic devices.

2.2 Introduction

Recently the MoS_2 monolayer has provided a new testbed for the study of fermion physics in reduced dimensions. Its strong intrinsic SOC and huge band gap [59], approximately $2\lambda = 150$ meV and $2\Delta = 1.66$ eV, respectively, render it pertinent to potential applications in spintronics and optoelectronics [103, 44, 48, 45]. Due to these features, MoS_2 may be more appropriate for device applications than graphene and the conventional two-dimensional electron gas (2DEG).

In addition to monolayer MoS_2, it has been recently realized that bilayer MoS_2 has potential applications in optoelectronics and spintronics. Also, a band-gap tuning is possible in a MoS_2 bilayer in the presence of a perpendicular electric field E_z [108, 109, 110]. Additional reported properties of bilayer MoS_2 include magnetoelectric effects and valley-controlled spin-quantum gates [111], tuning of the valley magnetic moment [112], and electrical control of the valley-Hall effect [113]. Moreover, a field-effect transistor has been realized experimentally in a few-layer MoS_2 [114]. In contrast, bilayer graphene has intrinsically a very weak SOC [115, 116] and, when not biased, a zero band gap [117, 118, 119]. There exist numerous theoretical and experimental [118, 120, 121, 122, 123] studies of magnetotransport properties in bilayer graphene. Although its band gap can be controlled by an electric field E_z [124, 125, 126, 127], high-quality samples of MoS_2 bilayers with a strong intrinsic SOC and a huge band gap are of particular importance. Contrary to bilayer graphene, the MoS_2 bilayer has greater potential for future spintronic and valleytronic applications. Recently, not only the QHE but also the SdH oscillations have been observed in high-quality monolayer and multilayer MoS_2 [57] but neither magnetotransport nor the effect of an electric field E_z have, to our knowledge, been theoretically studied for bilayer MoS_2. Such a study is the aim of the present work.

The chapter is organized as follows. In Sec. 2.3 we formulate the problem and discuss the band structure of bilayer MoS_2 with the help of the eigenvalues and eigenfunctions. We then present the numerical results of the Hall conductivity, spin and valley polarizations using the linear-response

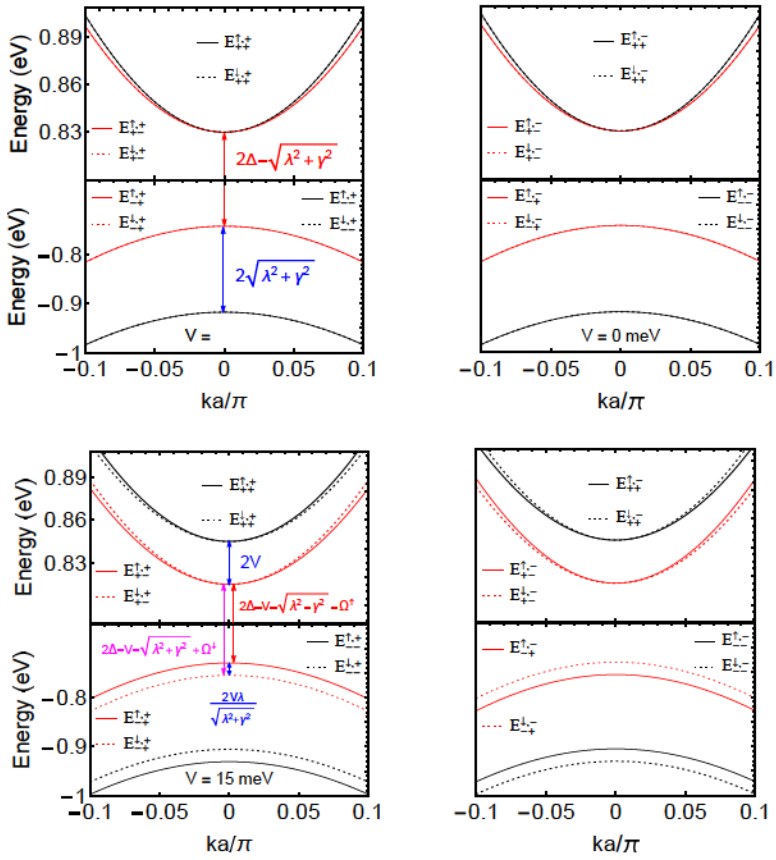

Figure 2.1: Band structure of bilayer MoS_2 for $\lambda = 0.074$ eV and $\gamma = 0.047$ eV. The upper panels are for zero electric field energy ($V = 0$) and the lower ones for $V = 15$ meV. The left (right) panels are for the K (K') valley and $\Omega^s = s\lambda V/[\lambda^2 + \gamma^2]^{1/2}$.

formulas of Ref. [128]. Interestingly, we find that the Hall-plateau sequence depends on the field E_z and becomes unconventional when E_z is present. Also, we compare the results with those on bilayer graphene. Concluding remarks follow in Sec. 2.6.

2.3 Formulation and electronic spectrum

The one-electron Hamiltonian of bilayer MoS_2 near the K and K' valleys [111, 112, 131, 132] reads

$$H^\tau = \begin{pmatrix} -\xi_1^{s\tau} & v_F p_-^\tau & \gamma & 0 \\ v_F p_+^\tau & \xi_2^{s\tau} & 0 & 0 \\ \gamma & 0 & -\xi_3^{s\tau} & v_F p_+^\tau \\ 0 & 0 & v_F p_-^\tau & \xi_4^{s\tau} \end{pmatrix}. \tag{1}$$

Here, $\tau = 1(-1)$ is for K (K') valley, $p_{\pm}^{\tau} = \tau p_x \pm i p_y$ with $\mathbf{p} = (p_x, p_y)$ the two-dimensional momentum operator, $\xi_1^{s\tau} = \kappa + \tau s\lambda + sM_z - \tau M_v$, $\xi_2^{s\tau} = \alpha - sM_z + \tau M_v$, $\xi_3^{s\tau} = \alpha - \tau s\lambda - sM_z + \tau M_v$, $\xi_4^{s\tau} = \kappa + sM_z - \tau M_v$ with $\kappa = \Delta + V$ and $\alpha = \Delta - V$ with Δ the monolayer band gap. Further, v_F =0.53$\times 10^6$ m/s [107] is the Fermi velocity, V the external electric field energy, λ the strength of the intrinsic SOC with spins up (down) represented by $s = +1(\uparrow)(s = -1(\downarrow))$, and γ the effective interlayer interaction energy. Moreover, $M_z = g'\mu_B B/2$ is the Zeeman exchange field induced by ferromagnetic order, g' the Landé g factor ($g' = g'_e + g'_s$), and μ_B the Bohr magneton [133]; $g'_e = 2$ is the free electron g factor and $g'_s = 0.21$ the out-of-plane factor due to the strong SOC in MoS_2. The term, $M_v = g'_v \mu_B B/2$ breaks the valley symmetry of the levels and $g'_v = 3.57$ [133]. The valley splitting has been measured in very recent experiments [134, 135, 136, 137] and is theoretically shown to be approximately 30 meV by first-principles calculations [138]. The eigenvalues $E_{\mu}^{s,\tau}(k)$ of Eq. (1), when the magnetic field is absent, are $E_{\mu}^{s,\tau}(k) = \hbar v_F \varepsilon_{\mu}^{s,\tau}(k)$.The subscript $\mu = (\mu_1, \mu_2)$ is used to denote the positive and negative energies of the upper layer, by $\mu_1 = \pm 1$, and of the lower layer by $\mu_2 = \pm 1$. The factor $\varepsilon_{\mu}^{s,\tau}(k) \equiv \varepsilon$ is the solution of the fourth-degree equation

$$\left[(\varepsilon - \alpha')(\varepsilon + \kappa' - \tau s\lambda') - k^2\right]\left[(\varepsilon - \kappa')(\varepsilon + \alpha' + \tau s\lambda') - k^2\right] - \gamma'^2(\varepsilon - \alpha')(\varepsilon - \kappa') = 0, \tag{2}$$

where $k \equiv k_y$ is the wave vector, $\varepsilon = E/\hbar v_F$ with $E \equiv E_{\mu}^{s,\tau}(k)$, $\lambda' = \lambda/\hbar v_F$, $\kappa' = \kappa/\hbar v_F$, $\gamma' = \gamma/\hbar v_F$, and $\alpha' = \alpha/\hbar v_F$. In the combined limit $\lambda' \to 0$, $\kappa' \to 0$, $\alpha' \to 0$, we obtain the energy dispersion for bilayer graphene [139].

In the upper panels of Fig. 2.1 we plot the energy dispersion of bilayer MoS_2 for field $E_z = 0$ ($V = 0$ meV) at both valleys. We remark the following: (i) The splitting due to the SOC is zero in the conduction and valence bands even in the presence of SOC [108, 109, 110, 111, 112, 132, 131]. (ii) The splitting due to interlayer hopping is zero in the conduction band but finite in the valence band [108, 109, 110, 111, 112, 132, 131]. Further, the splitting in the valence band is a combined effect of inter-layer coupling and SOC given by $2[\lambda^2 + \gamma^2]^{1/2}$ at $k = 0$. This relation indicates that the valence band is still split for $\lambda = 0$ [131]. (iii) The gap between conduction and valence band edges is given by $2\Delta - [\lambda^2 + \gamma^2]^{1/2}$ for $k = 0$ [131]. Notice that the effects of SOC and interlayer

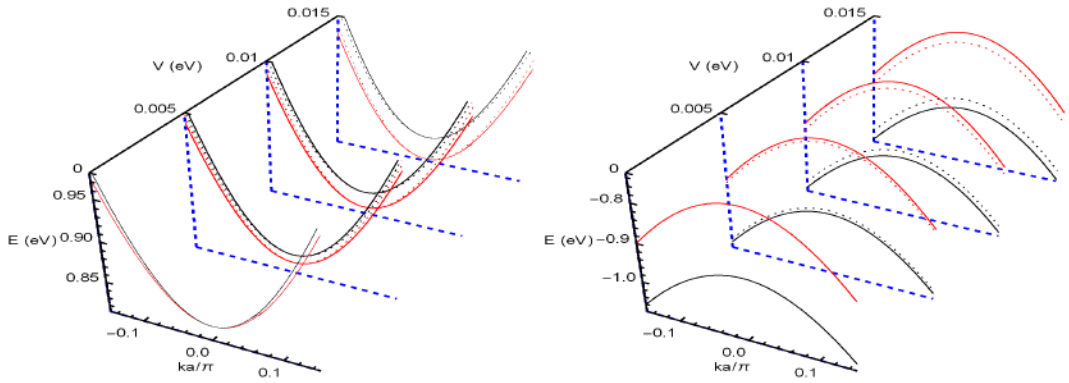

Figure 2.2: Band structure of bilayer MoS_2 for different electric field E_z. The left (right) panel is for the conduction (valence) band. The curve marking and parameters are as Fig. 2.1.

coupling are negligible in the conduction band, near $k = 0$, while at large values of k the SOC effect dominates.

For a finite field E_z ($V = 15$ meV) we plot the energy spectrum in the lower panels of Fig. 2.1. We remark the following: (i) The SOC splitting is modified by the field E_z. We also note that the spin splitting in the conduction band due to the SOC is negligible for the parameters and scale used. On the other hand, the valence band completely dictates the lifting of the spin degeneracy. (ii) An interlayer splitting is obtained in both the conduction and valence bands. Analytically we obtain the gaps $2V\lambda/[\lambda^2+\gamma^2]^{1/2}$, for $V \ll \lambda$, and $2V$ at the valence and conduction band edges, respectively. (iii) The band gap is also reduced by the field $E_z \propto V$. It is equal to $2\Delta - V - [\lambda^2+\gamma^2]^{1/2} - \tau s\lambda V/[\lambda^2+\gamma^2]^{1/2}$ for $V \ll \lambda$. The spin and layer splittings increase with the field E_z [109, 110, 143] or energy V, which can be seen in Fig. 2.2. So far we assumed that the band edges are at the K point of the Brillouin zone but this may not be the case neither for the valence band nor for the conduction band. In fact, there are arguments that our assumption holds [44, 111, 112, 140, 141] but DFT calculations and a recent ARPES measurement [142] indicate that the valence band edge is shifted to the Γ point.

2.3.1 Landau levels

In the presence of a magnetic field B perpendicular to the layers we replace $\mathbf{p}$ by $-i\hbar\nabla + \mathbf{A}$ in Eq. (1) and take the vector potential $\mathbf{A}$ in the Landau gauge $\mathbf{A} = (0, Bx, 0)$. After diagonalizing

Eq. (1) the LL spectrum is obtained as

$$E^{s,\tau}_{n,\mu} = \hbar\omega_c\, \varepsilon^{s,\tau}_{n,\mu}, \tag{3}$$

where $\omega_c = v_F\sqrt{2eB/\hbar}$ is the cyclotron frequency. For $n \geq 1$ the factor $\varepsilon^{s,\tau}_{n,\mu} \equiv \varepsilon$ is obtained by diagonalizing Eq. (1) numerically. The eigenfunctions are

$$\psi^{s,+}_{n,\mu} = \frac{1}{\sqrt{L_y}} \begin{pmatrix} \varrho^{s,+}_{n,\mu}\phi_n \\ \Theta^{s,+}_{n,\mu}\,\phi_{n-1} \\ \Lambda^{s,+}_{n,\mu}\,\phi_n \\ \Upsilon^{s,+}_{n,\mu}\,\phi_{n+1} \end{pmatrix} e^{ik_y y}, \qquad \psi^{s,-}_{n,\mu} = \frac{1}{\sqrt{L_y}} \begin{pmatrix} \Lambda^{s,-}_{n,\mu}\,\phi_n \\ \Upsilon^{s,-}_{n,\mu}\,\phi_{n+1} \\ \varrho^{s,-}_{n,\mu}\,\phi_n \\ \Theta^{s,-}_{n,\mu}\,\phi_{n-1} \end{pmatrix} e^{ik_y y}. \tag{4}$$

The coefficients are given by $\Theta^{s,\tau}_{n,\mu} = \sqrt{n}\,\varrho^{s,\tau}_{n,\mu}/[\varepsilon^{s,\tau}_{n,\mu} - d^{s\tau}_2]$, $\Lambda^{s,\tau}_{n,\mu} = k^{s,\tau}_{n,\mu}\varrho^{s,\tau}_{n,\mu}$, and $\Upsilon^{s,\tau}_{n,\mu} = \sqrt{n+1}\,k^{s,\tau}_{n,\mu}\,\varrho^{s,\tau}_{n,\mu}/[\varepsilon^{s,\tau}_{n,\mu} - d^{s\tau}_4]$, with $\varrho^{s,\tau}_{n,\mu}$ the normalization constants

$$\varrho^{s,\tau}_{n,\mu} = \left\{(k^{s,\tau}_{n,\mu})^2\left[1 + (n+1)/(\varepsilon^{s,\tau}_{n,\mu} - d^{s\tau}_4)^2\right)\right] + 1 + n/(\varepsilon^{s,\tau}_{n,\mu} - d^{s\tau}_2)^2\right\}^{-1/2} \tag{5}$$

and $k^{s,\tau}_{n,\mu} = [(\varepsilon^{s,\tau}_{n,\mu} + d^{s\tau}_1)(\varepsilon^{s,\tau}_{n,\mu} - d^{s\tau}_2) - n]/t(\varepsilon^{s,\tau}_{n,\mu} - d^{s\tau}_2)$, $t = \gamma/\hbar\omega_c$, $d^{s\tau}_1 = \kappa^\tau + s\lambda + \tau(sM_z - \tau M_v)/\hbar\omega_c$, $d^{s\tau}_2 = \alpha^\tau - \tau(sM_z - \tau M_v)/\hbar\omega_c$, $d^{s\tau}_3 = \alpha^\tau - s\lambda - \tau(sM_z - \tau M_v)/\hbar\omega_c$, and $d^{s\tau}_4 = \kappa^\tau + \tau(sM_z - \tau M_v)/\hbar\omega_c$ with $\kappa^\tau = \Delta + \tau V$ and $\alpha^\tau = \Delta - \tau V$ are dimensionless parameters. Therefore, the wave function of bilayer MoS_2 is a mixture of Landau wave functions with indices $n-1$, n, and $n+1$.

2.4 Hall conductivity

To evaluate the Hall conductivity, we use the expression given in chapter 3. Fig. 2.3 shows the Hall conductivity as a function of the field B for $V = 0$ meV. We found that the height of the steps is not constant: there are two different heights: $2\,e^2/h$ and $4\,e^2/h$ see Fig. 2.3, black curve, in the absence of the spin and valley Zeeman terms. However, additional new heights $2\,e^2/h$, $3\,e^2/h$ and $4\,e^2/h$ emerge in the sequence ladder in their presence as the red curve shows. Further, the plateaux in bilayer MoS_2 have different origin than those in bilayer graphene: the former are due to the strong

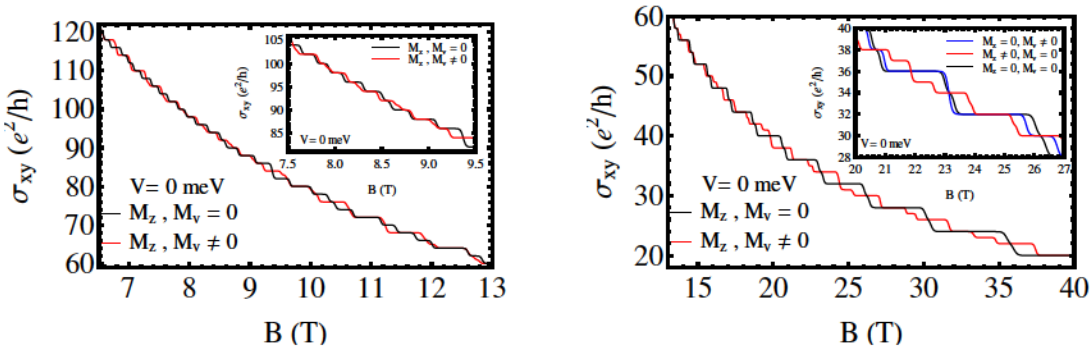

Figure 2.3: Hall conductivity as a function of the magnetic field B for $T = 1$ K and $V = 0$ meV. The two panels differ only in the range of B. For further clarity, the range 7.5 T-9.5 T is shown in the inset to the left panel and the range 20 T-27 T in that to the right panel.

SOC whereas the later result from strong interlayer coupling [118, 119]. A noteworthy feature of bilayer MoS_2 is that the influence of SOC and interlayer coupling is enhanced with increasing LL index and leads to new Hall plateaux as is evident from both panels of Fig. 2.3. In contrast to monolayer MoS_2 [55], the plateaux in bilayer MoS_2 occur at higher magnetic fields.

2.5 Spin and valley polarization

The spin P_s and valley P_v polarizations are evaluated by using the conductivities expressions that are given in chapter 3. We plot the spin P_s (black solid curve) and P_v (red dotted curve) polarization versus magnetic field at $T = 1$ K, $V = 0$ meV and finite Zeeman fields in Fig. 2.4. As expected and can be seen, here too we have a beating pattern at low magnetic fields and well-resolved separation between both P_s and P_v at higher magnetic fields. The fact is that strong magnetic fields give rise to larger splittings of the LLs. In contrast to monolayer MoS_2 [55], we find 100% valley polarization above $B > 13$ T whereas we attain 90% spin polarization above $B > 20$ T. Notice also the square-wave character of P_v above $B > 13$ T. However, for $M_z = M_v = 0$, there is no P_s and P_v as shown by the blue curve.

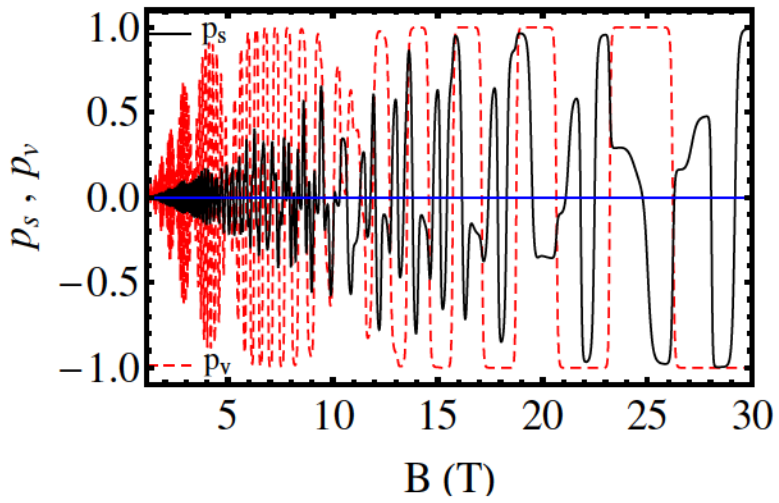

Figure 2.4: Spin P_s and valley P_v polarizations versus magnetic field B at $T = 1$ K. The parameters are the same as in Fig. 2.3 for $M_z \neq M_v \neq 0$.

2.6 Conclusions

We studied quantum magnetotransport in bilayer MoS_2 in the presence of perpendicular electric (E_z) and magnetic (B) fields. At $B = 0$ we showed that there is no spin splitting for zero field E_z in both the conduction and valence bands whereas there is one for finite field E_z. Further, for $E_z \neq 0$ we demonstrated that the conduction band is still spin degenerate while the spin degeneracy in the valence band is fully lifted (see Fig. 2.1). We showed though that the layer splitting and band gap can be controlled by the field E_z. The spin degeneracy of the levels, for $E_z = 0$, in the conduction band, is lifted for $B \neq 0$ and is also enhanced linearly with B. Furthermore, a finite field E_z leads to a significant enhancement of the spin splitting energy in the adjacent LLs of the conduction band. Moreover, we showed that the combined action of spin and valley Zeeman fields and inter-layer splitting allow for intra-LL transitions and lead to new quantum Hall plateaux. The field E_z modifies the layer splitting. As a result, steps of various heights, in multiples of e^2/h (Fig. 2.3), occur in the Hall conductivity.

Beating patterns, at low B fields, and splittings, at strong B fields, also occur in the spin and valley polarizations. It is worth emphasizing that a 100%, square-wave-shaped valley polarization is obtained for $B > 13$ T and 90% spin polarization for $B > 20$ T. The spin and valley Zeeman

fields lead to a giant splitting for strong B fields and to a lifting of the fourfold spin and valley degeneracies. The position of the plateaux as well as the peaks and beating pattern are sensitive to the field E_z and to the spin and valley Zeeman fields. The results, which we hope will be tested by experiments, indicate that bilayer MoS_2 is a promising alternative to bilayer graphene in the quest for gapped Dirac materials. We expect further applications of bilayer MoS_2 in the field of valleytronics and spintronics.

2.7 Acknowledgments

M. Z. and K. S. acknowledge the support of Higher Education Commission of Pakistan through project No. $20-1484/R\&D/09$. K. S. also acknowledges the support of the Abdus Salam International Center for Theoretical Physics (ICTP) in Trieste, Italy, through the Associate Scheme where part of this work was completed. This work was supported by the the University of Hafr Al Batin (MT). The work of P. V. was supported by the Canadian NSERC Grant No. OGP0121756.

Chapter 3

Magneto-optical properties of bilayer transition metal dichalcogenides

3.1 Abstract

In transition metal dichalcogenides (TMDCs) the spin-orbit interaction affects differently the conduction and valence band energies as functions of the wave vector k and the band gap is usually large except in few TMDCs that are metallic without band gaps. Consequently, when a perpendicular magnetic field B is applied the conduction and valence band Landau levels are also different and this leads to a splitting of the interband optical absorption lines in both the absence and presence of an external electric field E_z. When B and E_z are present the peaks in the imaginary part of the Hall conductivity give two distinct contributions of opposite sign to the interband spectrum. The real part of the right- and left-handed interband conductivity, however, retains its two-peak structure but the peaks are shifted in energy and amplitude with respect to each other in contrast with graphene. The response of the intraband conductivity is significantly modified when the Fermi energy E_F and the field B are varied. Its optical spectral weight is found to increase with E_F in contrast with the decrease observed in graphene. Further, the position and amplitude of the intraband response depend on the field B. The absorption peaks vary linearly with B for all fields similar to bilayer graphene for low fields but in contrast with the high-field $\sqrt{B}$ dependence in it.

3.2 Introduction

Two-dimensional materials have attracted a lot of attention due to their applications in spintronics [147], valleytronics [61] and optoelectronics [44, 48]. In this regard the group VI transition-metal dichalcogenides (TMDCs) have the form MX_2 (M=Mo,W; X=S,Se) are of particular interest due to their valley degree of freedom, large direct band gap [44, 45, 46] and strong intrinsic spin-orbit interaction (SOI) [43, 47]. Recently, nanoelectronic devices, such as amplifiers, photodetectors, thin film transistors, and logical circuits [49, 50, 48, 51], based on their excellent electronic properties have been experimentally realized. In addition, several properties of TMDC monolayers have been investigated theoretically and experimentally [52, 53, 54, 55, 56, 57, 58] e.g., magneto-optical spectra and magnetotransport.

Layered TMDCs, such as bilayer systems, exhibit a broad range of physical properties and have been extensively studied for applications in catalysis, tribology, electronics, photovoltaics, and electrochemistry [148, 184, 185, 186]. Also, few layer TMDCs have potential applications in nanoelectronics and nanophotonics. A field-effect transistor has been realized experimentally in a few-layer MoS_2 [114]. Similarly, magnetoelectric effects and valley-controlled spin quantum gates [111], tuning of the valley magnetic moment [112], electrical control of the valley-Hall effect [113], and spin-layer locking effect [131] has been explored in bilayer TMDCs. Most recently, magnetotransport studies of bilayer MoS_2 have been carried out [152]. Additionally, a band gap tuning is possible and more easily achievable in bilayer TMDCs than in monolayer TMDCs in the presence of a perpendicular electric field E_z [110, 109, 153]. However, less attention has been paid to the optical properties of bilayer TMDCs in the simultaneous presence of electric and magnetic fields.

In this work we study in detail the effect of magnetic and electric fields on the magneto-optical conductivity of bilayer TMDCs with particular emphasis on the asymmetry between the conduction band (CB) and valence band (VB). Moreover, we assess the effect of the electric field on the band structure with and without magnetic field, and on the magneto-optical conductivities. Also, we compare our results with those for monolayer and bilayer graphene.

We focus on bilayer WSe_2 due to recent experimental progress [112, 113, 154, 205, 206, 209]

but our findings are equally pertinent to other bilayer TMDCs, e.g. $MoSe_2$ and WS_2. The WSe_2 bilayer has much stronger SOI in the conduction ($2\lambda_c = 30$ meV) and valence ($2\lambda_v = 450$ meV) bands compared to bilayer MoS_2 ($2\lambda_c = 0$ meV). The band-edge energy difference $E_{\Gamma K}$ between the Γ and K points in bilayer WSe_2 is much smaller than in bilayer MoS_2 [210, 159]. Therefore, the CB and VB edges in bilayer WSe_2 lie at the K point. Accordingly, bilayer WSe_2 has advantages over the MoS_2 when studying its optical properties due to the direct band gap at the $\pm K$ points.

In Sec. 3.3 we specify the Hamiltonian and obtain the energy eigenvalues and eigenfunctions with and without magnetic field. In Sec. 3.4 we present a general expression for the conductivity $\sigma(\omega)$ and provide numerical results. Conclusions and a summary follow in Sec. 3.5.

3.3 Energy spectrum

In AB stacked bilayer TMDCs the top layer is rotated with respect to the bottom layer by 180 degrees such that the S atoms in it sit on top of the M atoms of the bottom layer. As a result, the effective Hamiltonian for bilayer TMDCs can be constructed from that of the single layer by simply adding the interlayer coupling term γ [59]. Then the one-electron Hamiltonian of bilayer WSe_2 near the K and K' valleys reads [111, 112, 131, 132]

$$H^\tau = \begin{pmatrix} -\xi_1^{s\tau} & v_F\pi_-^\tau & \gamma & 0 \\ v_F\pi_+^\tau & \xi_2^{s\tau} & 0 & 0 \\ \gamma & 0 & -\xi_3^{s\tau} & v_F\pi_+^\tau \\ 0 & 0 & v_F\pi_-^\tau & \xi_4^{s\tau} \end{pmatrix}. \tag{6}$$

Here $\tau = 1(-1)$ is for the K (K') valley, $\pi_\pm^\tau = \tau\pi_x \pm i\pi_y$, $\xi_1^{s\tau} = \kappa + \tau s\lambda_v + sM_z - \tau M_v$, $\xi_2^{s\tau} = \alpha - \tau s\lambda_c - sM_z + \tau M_v$, $\xi_3^{s\tau} = \alpha - \tau s\lambda_v - sM_z + \tau M_v$, $\xi_4^{s\tau} = \kappa + \tau s\lambda_c + sM_z - \tau M_v$ and $\kappa = \Delta + V$ and $\alpha = \Delta - V$ with Δ the monolayer band gap. Further, v_F =5×10^5 m/s is the Fermi velocity, V is the potential difference between the two layers due to a perpendicular electric field E_z, and λ the strength of the SOI with spins up (down) represented by $s = +1(\uparrow)(s = -1(\downarrow))$. Moreover, $M_z = g'\mu_B B/2$ is the Zeeman exchange field induced by ferromagnetic order, g' the Landé g factor ($g' = g'_e + g'_s$), and μ_B the Bohr magneton [136, 135]; $g'_e = 2$ is the free electron

g factor and $g_s' = 0.21$ the out-of-plane factor due to the strong SOI. The term $M_v = g_v' \mu_B B/2$ breaks the valley symmetry of the levels, $g_v' = 4$ [136, 135]. The eigenvalues $E_\mu^{s,\tau}(k)$ of Eq. (6), when the magnetic field is absent, are

$$E_\mu^{s,\tau}(k) = \hbar v_F \varepsilon_\mu^{s,\tau}(k). \tag{7}$$

The subscript $\mu = (\mu_1, \mu_2)$ is used for labeling the energy bands: $\mu_1 = +1(-1)$ is for the electron (hole) branches and $\mu_2 = +1(-1)$ is for the upper (lower) layer. Using the label μ_2 is allowed provided the interlayer coupling is weak, see Refs. [111, 131]. The factor $\varepsilon_\mu^{s,\tau}(k) \equiv \varepsilon$ in Eq. (7) is the solution of the quartic equation

$$\left[(\varepsilon + \xi_5^{s\tau})(\varepsilon - \xi_6^{s\tau}) - k^2\right]\left[(\varepsilon + \xi_7^{s\tau})(\varepsilon - \xi_8^{s\tau}) - k^2\right] - \gamma'^2 (\varepsilon - \xi_6^{s\tau})(\varepsilon - \xi_8^{s\tau}) = 0,$$

where $k \equiv k_y$ is the wave vector, $\varepsilon = E/\hbar v_F$, $\xi_5^{s\tau} = \xi_1^{s\tau}/\hbar v_F$, $\xi_6^{s\tau} = \xi_2^{s\tau}/\hbar v_F$, $\xi_7^{s\tau} = \xi_3^{s\tau}/\hbar v_F$, $\xi_8^{s\tau} = \xi_4^{s\tau}/\hbar v_F$, and $\gamma' = \gamma/\hbar v_F$. In the limit $\xi_i^{s\tau} \to 0$, $i = 5, .., 8$, we obtain the energy dispersion for bilayer graphene [139].

In the upper panel of Fig. 3.1 we plot the energy dispersion of bilayer WSe_2 for field $E_z = 0$ at both valleys. We remark the following: (i) The splitting between the levels due to SOI is finite in the CB given by $2\lambda_c$ at $k = 0$ in contrast to bilayer MoS_2 [111, 112, 131, 152]. Its means that four-fold degeneracy of CB in WSe_2 is partially lifted. So, the bands are two-two fold degenerate whereas it is four fold degenerate in bilayer MoS_2 at $k = 0$. But, the splitting due to interlayer hopping is negligible in the CB.(ii) The value of interlayer hopping between the two layers is finite in the VB [111, 112, 131, 152]. So, splitting of levels in the VB is a combined effect of interlayer hopping and SOI given by $2[\lambda_v^2 + \gamma^2]^{1/2}$ at $k = 0$. This relation indicates that the VB is still split for $\lambda_v = 0$ or $\gamma = 0$. Further, levels in VB are also two-two fold degenerate as seen upper panel of Fig. (1). (iii) The gap between conduction and valence band edges is given by $2\Delta - \lambda_c - [\lambda_v^2 + \gamma^2]^{1/2}$ for $k = 0$.

For $E_z \neq 0$ we plot the energy spectrum in the lower panels of Fig. 3.1. We note the following: (i) The field E_z modifies the SOI splitting. We note that two-fold spin degeneracy of all the bands in the CB and VB at each valley is completely lifted in contrast to bilayer MoS_2. However, bands have two-fold valley degeneracy i. e. energies of spin up and spin down bands at K and K' valleys

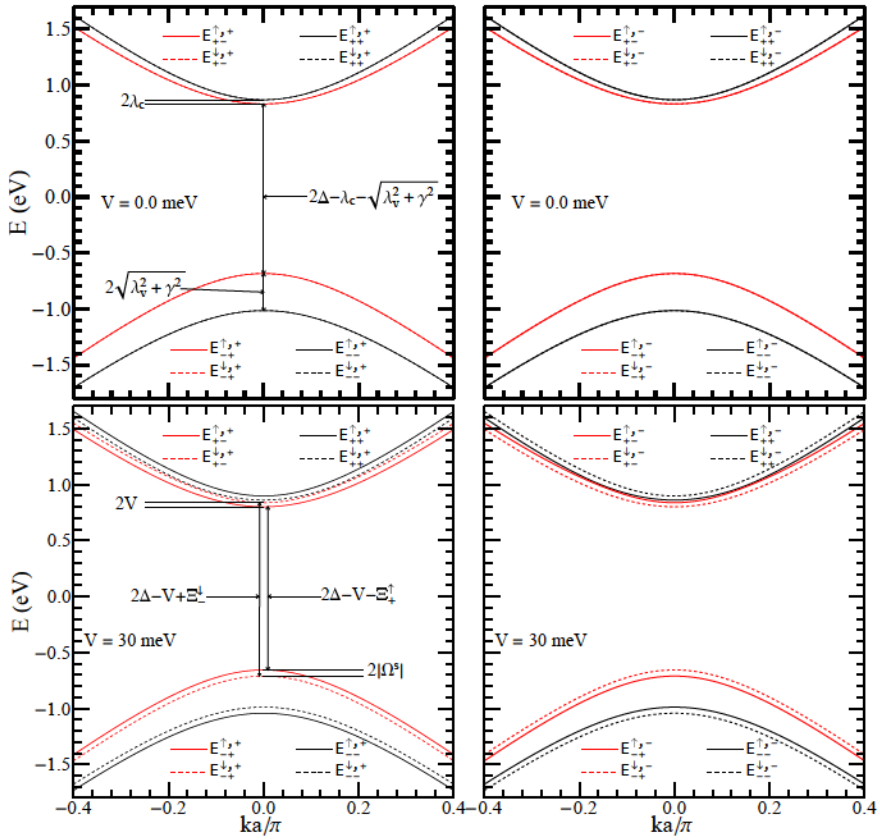

Figure 3.1: Band structure of bilayer WSe_2 for $2\lambda_c = 37$ meV, $2\lambda_v = 303$ meV, and $2\gamma = 134$ meV. The upper panels are for $V = 0$ meV, the lower ones for $V = 30$ meV. The left (right) panels are for the K (K') valley and $\Xi^s_\pm = \lambda_c \pm \sqrt{\lambda_v^2 + \gamma^2} + \Omega^s$ with $\Omega^s = s\lambda_v V/[\lambda_v^2 + \gamma^2]^{1/2}$.

are same and vise versa. (ii) An interlayer splitting is obtained in both the CB and VB. Analytically we obtain the gaps $2V\lambda_v/[\lambda_v^2 + \gamma^2]^{1/2}$ for $V \ll \lambda_v$ and $2V$ at the valence and conduction bands edges, respectively. (iii) The band gap is also reduced by the field $E_z \propto V$. It is equal to $2\Delta - V - s\lambda_c - [\lambda_v^2 + \gamma^2]^{1/2} - \tau s\lambda_v V/[\lambda_v^2 + \gamma^2]^{1/2}$ for $V \ll \lambda_v$.

3.3.1 Landau levels

In the presence of a magnetic field B perpendicular to the layers we replace π by $-i\hbar\nabla + \mathbf{A}$ in Eq. (6) and take the vector potential $\mathbf{A}$ in the Landau gauge $\mathbf{A} = (0, Bx, 0)$. After diagonalizing Eq. (6) the Landau level (LL) spectrum is obtained as

$$E^{s,\tau}_{n,\mu} = \hbar\omega_c\, \varepsilon^{s,\tau}_{n,\mu}, \tag{8}$$

with $\omega_c = v_F\sqrt{2eB/\hbar}$ the cyclotron frequency. For $n \geq 1$ the factor $\varepsilon^{s,\tau}_{n,\mu} \equiv \varepsilon$ is the solution of the quartic equation

$$\left[\left(\varepsilon + d_1^{s\tau}\right)\left(\varepsilon - d_2^{s\tau}\right) - n\right]\left[\left(\varepsilon + d_3^{s\tau}\right)\left(\varepsilon - d_4^{s\tau}\right) - (n+1)\right] - t^2\left(\varepsilon - d_2^{s\tau}\right)\left(\varepsilon - d_4^{s\tau}\right) = 0, \quad (9)$$

where $t = \gamma/\hbar\omega_c$, $d_1^{s\tau} = \kappa^\tau + s\lambda_v + \tau(sM_z - \tau M_v)/\hbar\omega_c$, $d_2^{s\tau} = \alpha^\tau - s\lambda_c - \tau(sM_z - \tau M_v)/\hbar\omega_c$, $d_3^{s\tau} = \alpha^\tau - s\lambda_v - \tau(sM_z - \tau M_v)/\hbar\omega_c$, and $d_4^{s\tau} = \kappa^\tau + s\lambda_c + \tau(sM_z - \tau M_v)/\hbar\omega_c$ with $\kappa^\tau = \Delta + \tau V$ and $\alpha^\tau = \Delta - \tau V$. In the limit $\xi_i^{s\tau} \to 0$, $i = 5, .., 8$, Eq. (8) gives a LL dispersion similar to that of bilayer graphene [119, 118]. The eigenfunctions are

$$\psi^{s,+}_{n,\mu} = \frac{1}{\sqrt{L_y}} \begin{pmatrix} \varrho^{s,+}_{n,\mu}\phi_n \\ \Theta^{s,+}_{n,\mu}\,\phi_{n-1} \\ \Lambda^{s,+}_{n,\mu}\,\phi_n \\ \Upsilon^{s,+}_{n,\mu}\,\phi_{n+1} \end{pmatrix} e^{ik_y y}, \qquad \psi^{s,-}_{n,\mu} = \frac{1}{\sqrt{L_y}} \begin{pmatrix} \Lambda^{s,-}_{n,\mu}\,\phi_n \\ \Upsilon^{s,-}_{n,\mu}\,\phi_{n+1} \\ \varrho^{s,-}_{n,\mu}\,\phi_n \\ \Theta^{s,-}_{n,\mu}\,\phi_{n-1} \end{pmatrix} e^{ik_y y}. \quad (10)$$

Here $\phi_n \equiv \phi_n(\upsilon) = (2^n n! l_B\sqrt{\pi})^{-1/2} e^{-\upsilon^2/2} H_n(\upsilon)$ is the harmonic oscillator wave function with $\upsilon = (x - l_B^2 k_y)/l_B$ and $H_n(\upsilon)$ the Hermite polynomial of order n. Notice that $\phi_n \equiv 0$ for $n < 0$. The coefficients are given by $\Theta^{s,\tau}_{n,\mu} = \sqrt{n}\,\varrho^{s,\tau}_{n,\mu}/[\varepsilon^{s,\tau}_{n,\mu} - d_2^{s\tau}]$, $\Lambda^{s,\tau}_{n,\mu} = k^{s,\tau}_{n,\mu}\varrho^{s,\tau}_{n,\mu}$, and $\Upsilon^{s,\tau}_{n,\mu} = \sqrt{n+1}\,k^{s,\tau}_{n,\mu}\,\varrho^{s,\tau}_{n,\mu}/[\varepsilon^{s,\tau}_{n,\mu} - d_4^{s\tau}]$, with $\varrho^{s,\tau}_{n,\mu}$ the normalization constants

$$\varrho^{s,\tau}_{n,\mu} = \left\{(k^{s,\tau}_{n,\mu})^2\left[1 + \frac{(n+1)}{\left(\varepsilon^{s,\tau}_{n,\mu} - d_4^{s\tau}\right)^2}\right] + 1 + \frac{n}{\left(\varepsilon^{s,\tau}_{n,\mu} - d_2^{s\tau}\right)^2}\right\}^{-1/2} \quad (11)$$

and $k^{s,\tau}_{n,\mu} = [(\varepsilon^{s,\tau}_{n,\mu} + d_1^{s\tau})(\varepsilon^{s,\tau}_{n,\mu} - d_2^{s\tau}) - n]/t(\varepsilon^{s,\tau}_{n,\mu} - d_2^{s\tau})$. As Eq. (10) shows, the full wave function is a mixture of the Landau wave functions with indices $n-1$, n, and $n+1$.

For $n = 0$ there are two special LLs. One has the energies $\varepsilon^{s,+}_{0,+-} = d_4^{s+}$ and $\varepsilon^{s,-}_{0,+-} = d_2^{s-}$ for

the K and K' valleys, respectively. The corresponding wave functions are

$$\psi^{s,+}_{0,+-} = \frac{1}{\sqrt{L_y}} \begin{pmatrix} 0 \\ 0 \\ 0 \\ \phi_0 \end{pmatrix} e^{ik_y y}, \quad \psi^{s,-}_{0,+-} = \frac{1}{\sqrt{L_y}} \begin{pmatrix} 0 \\ \phi_0 \\ 0 \\ 0 \end{pmatrix} e^{ik_y y}. \tag{12}$$

This LL has exactly the same properties as the $n = 0$ conventional, non-relativistic LL. For $\Delta = \lambda_c = \lambda_v = V = 0$, this level has exactly zero energy as the $n = 0$ LL for bilayer graphene [119, 118]. Also, from Eq. (9) we obtain three other levels for $n = 0$. We obtain the wave functions for two of these levels from Eq. (10) by simply setting $n = 0$ in it. Further, we specify the quantum number (μ) labels for these two levels as $\mu = (+,+)$ and $\mu = (-,+)$. However, for the third LL we specify n and μ as shown in the eigenfunctions

$$\psi^{s,+}_{0,--} = \frac{1}{\sqrt{L_y}} \begin{pmatrix} \varrho^{s,+}_{0,--}\phi_0 \\ 0 \\ \Lambda^{s,+}_{0,--}\phi_0 \\ \varrho^{s,+}_{0,--}t\phi_1 \end{pmatrix} e^{ik_y y}, \qquad \psi^{s,-}_{0,--} = \frac{1}{\sqrt{L_y}} \begin{pmatrix} \Lambda^{s,-}_{0,--}\phi_0 \\ \varrho^{s,-}_{0,--}t\phi_1 \\ \varrho^{s,-}_{0,--}\phi_0 \\ 0 \end{pmatrix} e^{ik_y y}, \tag{13}$$

where $\Lambda^{s,\tau}_{0,--} = \varrho^{s,\tau}_{0,--}t(\varepsilon^{s,\tau}_{0,--} - d^{s,\tau}_4)$. The normalization constants are

$$\varrho^{s,\tau}_{0,--} = k^{s,\tau}_{0,--}\left\{(k^{s,\tau}_{0,--})^2 + t^2[1 + (\varepsilon^{s,\tau}_{0,--} - d^{s,\tau}_{4,--})]\right\}^{-1/2} \tag{14}$$

and $k^{s,\tau}_{0,--} = (\varepsilon^{s,\tau}_{0,--} + d^{s,\tau}_{3,--})(\varepsilon^{s,\tau}_{0,--} - d^{s,\tau}_{4,--}) - 1$. The wave function corresponding to this LL is a mixture of the $n = 0$ and $n = 1$ conventional (nonrelativistic) Landau functions ϕ_0 and ϕ_1. For $\Delta = \lambda_c = \lambda_v = V = 0$ Eq. (13) gives the eigenfunctions for bilayer graphene [119, 118].

In Fig. 3.2 (left panels) we plot the spin and valley dependent LL spectrum, but independent of k_y, given by Eq. (8) versus the magnetic field B for $V = 0$ and finite spin M_z and valley M_v Zeeman fields. The marking of all curves is explained in the upper panel. We find the following: (i) The energy spectrum grows linearly with B due to the huge band gap. (ii) For $M_z = M_v = 0$, all LLs ($n \geq 1$) are two-fold degenerate corresponding to the two valleys including the $n = 0$ LL with

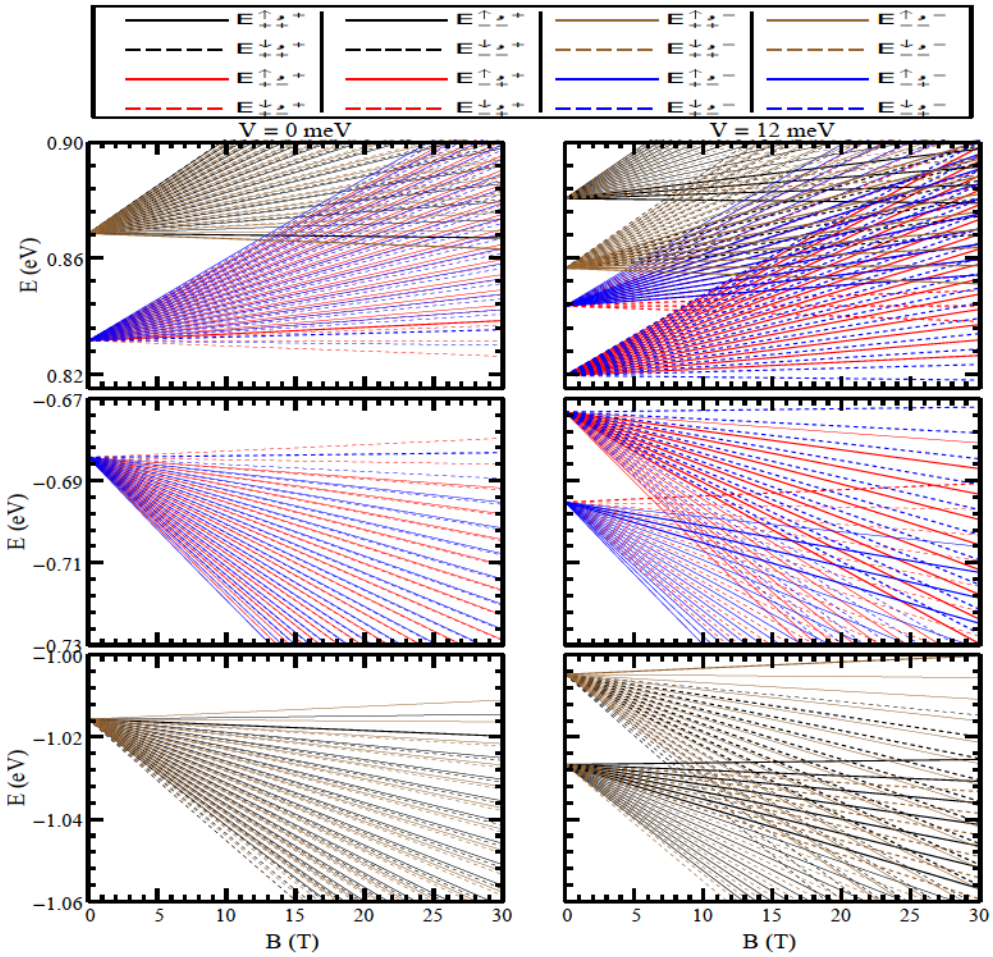

Figure 3.2: Energy spectrum of bilayer WSe_2 versus magnetic field B for $M_z \neq, M_v \neq 0$. The left panel is for the $E_z = 0$ and right one for $E_z \neq 0$, respectively. The upper panel explains the colour and style assignments of the curves. The upper row of panels is for the LLs in the conduction band and the last two rows of panels for the LLs in the valence band.

energies $\varepsilon^{s,\tau}_{0,++}$, $\varepsilon^{\downarrow,+}_{0,-+}$, $\varepsilon^{\uparrow,-}_{0,-+}$, and $\varepsilon^{\downarrow,\tau}_{0,--}$ in both the conduction and valence bands. The LL with energy $\varepsilon^{s,\tau}_{0,+-} = \Delta + s\lambda_c$ for $n = 0$ is doubly degenerate in the conduction band, i.e. $\varepsilon^{\uparrow,+}_{0,+-} \equiv \varepsilon^{\uparrow,-}_{0,+-}$ and $\varepsilon^{\downarrow,+}_{0,+-} \equiv \varepsilon^{\downarrow,-}_{0,+-}$. Further, in the valence band the $n = 0$ LL is two-fold valley degenerate, i.e. $\varepsilon^{\uparrow,+}_{0,-+} \equiv \varepsilon^{\downarrow,-}_{0,-+}$ and $\varepsilon^{\uparrow,+}_{0,--} \equiv \varepsilon^{\uparrow,-}_{0,--}$. In this situation, interlayer splitting among the levels of WSe_2 or MoS_2 bilayer is zero [152]. On the other hand, the intra-layer spin splitting in bilayer WSe_2 is significantly large given by $2\lambda_c$, which can be clearly seen in the limit of vanishing B as compared to bilayer MoS_2 [152]. (iii) For $M_z \neq 0, M_v \neq 0$, shown in the left panel of Fig. 3.2, the spin and valley degeneracies of all LLs ($n \geq 0$) are lifted i.e., the energies of the spin-up (-down) LLs at the K valley are different than the spin-down (-up) ones at the K' valley in contrast to the $B = 0$

case. (iv) The valley Zeeman term M_v lifts the spin degeneracy as well as the valley degeneracy in both the conduction and valence bands. This effect on the LLs, due to the M_v term, is absent in bilayer MoS_2 [152]. Notice that the inter-layer splitting among the levels of bilayer WSe_2 vanishes in contrast to bilayer MoS_2 [152].

We show the LL spectrum in Fig. 3.2 (right panels) for finite field E_z ($V = 12$ meV) including the M_z and M_v terms. We deduce the following: (i) The field E_z modifies the interlayer splitting, e.g., it makes it 24 meV and 23 meV in the conduction and valence bands, respectively. (ii) The spin and valley degeneracies of all levels ($n \geq 0$) are completely lifted, i.e., the energies of the spin-up ($\uparrow$) states at the K valley and a spin-down ($\downarrow$) ones at the K' valley are totally different in contrast to the $B = 0$ case. Moreover, we can adjust the LL separation by varying the external electric and magnetic fields. This becomes important when we tune the onset frequency of the magneto-optical conductivity.

3.3.2 Density of states

The density of states $D(E)$ is given by

$$D(E) = \frac{1}{S_0} \sum_{n,\tau,s,\mu,k_y} \delta(E - E^{s,\tau}_{n,\mu}), \tag{15}$$

where $S_0 = L_x L_y$ is the area of the system. The sum over k_y can be calculated by using $k_0 = L_x/2l_B^2$ and the prescription $\sum_{k_y} \to (L_y/2\pi) g_s g_v \int_{-k_0}^{k_0} dk_y = (S_0/D_0) g_s g_v$, with $D_0 = 2\pi l_B^2$; $g_s(g_v)$ denotes the spin (valley) degeneracy. In this work we take $g_s = g_v = 1$ because the spin and valley degeneracies are lifted. E_F at constant electron concentration n_e we obtain E_F from the relation

$$n_e = \int_{-\infty}^{\infty} D(E) f(E) dE = \frac{g_{s/v}}{D_0} \sum_{n,\tau,s,\mu} f(E^{s,\tau}_{n,\mu}), \tag{16}$$

where $f(E^{s,\tau}_{n,\mu}) = 1/\left[1 + \exp[\beta(E^{s,\tau}_{n,\mu} - E_F)]\right]$ is the Fermi-Dirac function and $\beta = 1/k_B T$.

The black solid curve in the upper panels of Fig. 3.3 shows E_F, obtained from Eq. (16) numerically, versus B for $E_z = 0$. The field B lifts the spin and valley degeneracies of all LLs ($n \geq 0$), i.e. the spin-up and spin-down electrons in the K valley have different energies than the corresponding

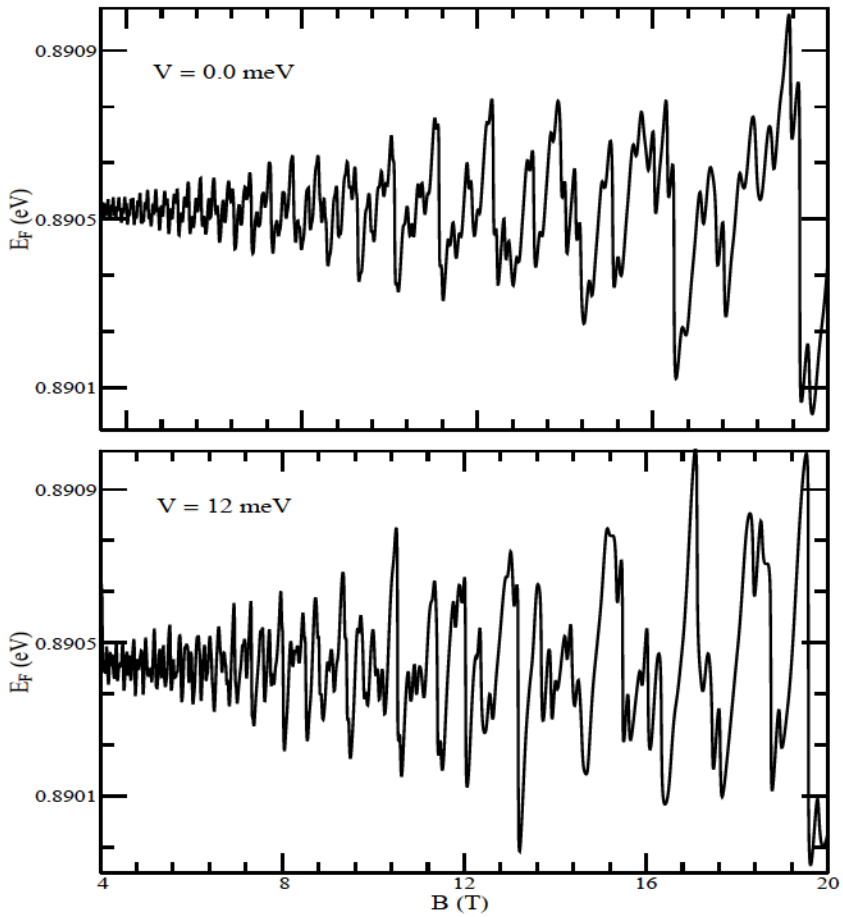

Figure 3.3: Fermi energy E_F versus B for an electron density $n_e = 4.3 \times 10^{13}$ cm^{-2}. The upper panels are for $V = 0$ meV and the lower ones for $V = 12$ meV.

ones in the K' valley. This leads to additional intra-LL small jumps in Fig. 3.3 (upper panels) that are enhanced, as shown in the lower panels of Fig. 3.3, when a finite electric field E_z is applied.

We evaluate $D(E)$ per unit area assuming a Gaussian broadening of the δ function in Eq. (15). At zero temperature we have $D(E) = (g_s g_v / D_0 \Gamma \sqrt{2\pi}) \sum_\zeta \exp[-(E - E_\zeta)^2 / 2\Gamma^2]$, where Γ is the width of the distribution and $|\zeta\rangle \equiv |n, \mu, s, \tau, k_y\rangle$. In Fig. 3.4 we plot the dimensionless $D(E)$ versus the field B in the conduction band for two different values of E_z and Γ. The Shubnikov-de Haas (SdH) oscillations are clearly shown. The level broadening effect becomes significant for weak B fields due to the small LL separation. On the other hand, this effect may become very weak in strong fields B for which the LL separation is strong and $\Gamma \propto \sqrt{B}$.

Looking closely at Fig. 3.4 we observe a beating of the SdH oscillations at low fields B and a pronounced splitting at higher fields. The beating of the oscillations is observed for $B \leq 10$

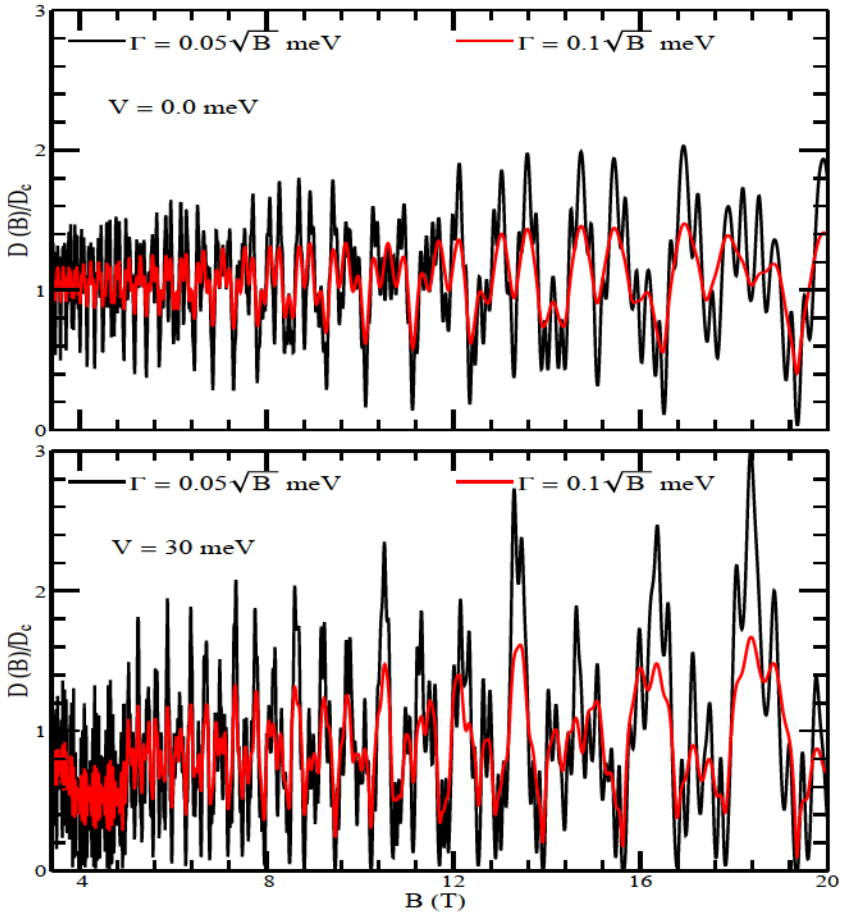

Figure 3.4: Dimensionless density of states, at the Fermi level, as a function of field B for LL width $\Gamma = 0.05\sqrt{B}$ meV (black curve) and $\Gamma = 0.1\sqrt{B}$ meV (red curve). The upper panels are for $V = 0$ and the lower ones for $V = 30$ meV.

T, with $E_z = 0$, and for $B \leq 5$ T with $E_z \neq 0$. Away from these ranges the beating pattern is replaced by a split in the SdH oscillations. This behaviour is explained by the closeness of the oscillation frequencies of the SOI-split LLs. The field B enhances the splitting in the conduction band by mixing the spin-up and spin-down states of neighbouring LLs into two unequally spaced energy branches. This is also the case of a 2DEG [146]. This beating pattern occurs when the level broadening is of the order of $\hbar\omega_c$; it is replaced by a split in the oscillations when the SOI becomes weak for large fields B. We further notice that the beating pattern shifts to lower magnetic fields for finite electric field energy V.

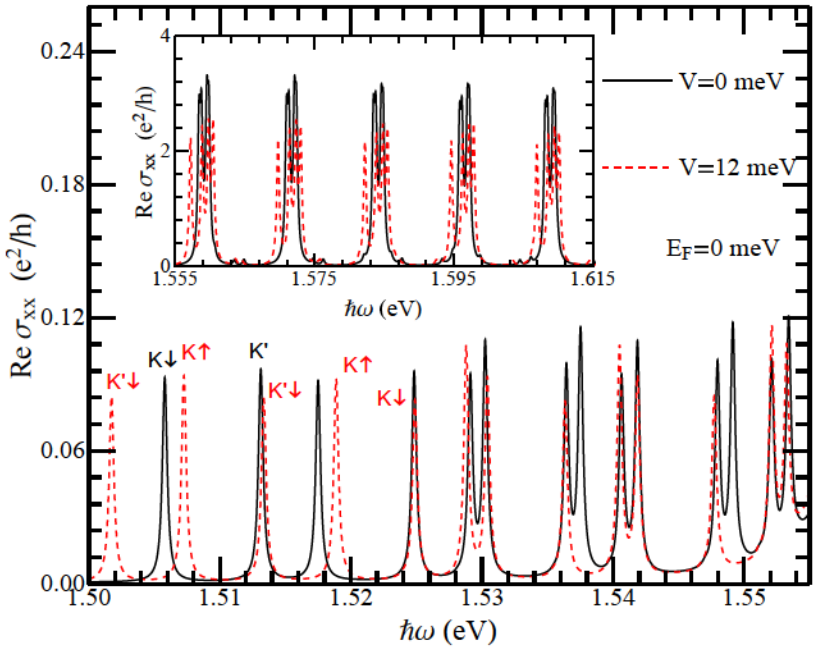

Figure 3.5: Real part of the longitudinal optical conductivity $\sigma_{xx}^{nd}(\omega)$ versus the photon energy $\hbar\omega$ for a field $B = 30$ T. The solid black and dotted red curves are for $V = 0$ and $V = 12$ meV, respectively. The inset shows Re$\sigma_{xx}^{nd}(\omega)$ for higher $\hbar\omega$. The spin assignment of the curves follows from Eq. (22).

3.4 Conductivities

We consider a many-body system described by the Hamiltonian $H = H_0 + H_I - \mathbf{R}\cdot\mathbf{F}(t)$, where H_0 is the unperturbed part, H_I is a binary-type interaction (e.g., between electrons and impurities or phonons), and $-\mathbf{R}\cdot\mathbf{F}(t)$ is the interaction of the system with the external field F(t) [128]. For conductivity problems we have $\mathbf{F}(t) = e\mathbf{E}(t)$, where $\mathbf{E}(t)$ is the electric field, e the electron charge, $\mathbf{R} = \sum_{\mathbf{r_i}}$, and $\mathbf{r_i}$ the position operator of electron i. In the representation in which H_0 is diagonal the many-body density operator $\rho = \rho^d + \rho^{nd}$ has a diagonal part ρ^d and a nondiagonal part ρ^{nd}. For weak electric fields and weak scattering potentials, for which the first Born approximation applies, the conductivity tensor has a diagonal part $\sigma_{\mu\nu}^d$ and a nondiagonal part $\sigma_{\mu\nu}^{nd}$, $\sigma_{\mu\nu} = \sigma_{\mu\nu}^d + \sigma_{\mu\nu}^{nd}, \mu, \nu = x, y$.

In general we have two kinds of currents, diffusive and hopping, with $\sigma_{\mu\nu}^d = \sigma_{\mu\nu}^{dif} + \sigma_{\mu\nu}^{col}$, but usually only one of them is present. When a magnetic field is present we have only a hopping current since the diffusive part $\sigma_{\mu\nu}^{dif}$ vanishes identically due to the vanishing velocity matrix elements as is

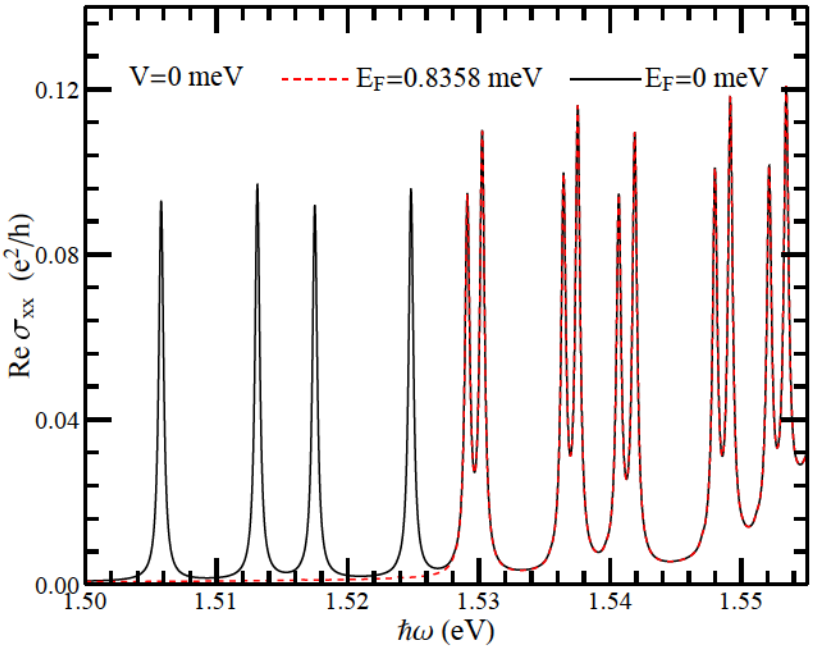

Figure 3.6: As in Fig. 3.5 but for two different values of E_F as indicated.

evident, for elastic scattering, by its form [128]

$$\sigma^{d}_{\mu\nu}(\omega) = \frac{\beta e^2}{S_0} \sum_{\zeta} f_\zeta (1 - f_\zeta) \frac{v_{\nu\zeta} v_{\mu\zeta} \tau_\zeta}{1 + i\omega\tau_\zeta}, \tag{17}$$

where τ_ζ is the momentum relaxation time, ω the frequency, and $v_{\mu\zeta}$ the diagonal matrix elements of the velocity operator. Further, $f_\zeta = [1 + \exp\beta(E_\zeta - E_F)]^{-1}$ is the Fermi-Dirac distribution function, $\beta = 1/k_B T$, T the temperature, and S_0 the area of the sample. In our case $v_{\mu\zeta} = 0$ and the conductivity given by Eq. (17) vanishes.

The ac hopping conductivity $\sigma^{col}_{\mu\nu}(\omega)$ is given by Eq. (2.64) of Ref. [44]. In strong fields B it is much smaller than the contribution $\sigma^{nd}_{\mu\nu}$, given below, and is neglected. Regarding this contribution $\sigma^{nd}_{\mu\nu}$ one can use the identity $f_\zeta(1 - f_{\zeta'})[1 - \exp\beta(E_\zeta - E_{\zeta'})] = f_\zeta - f_{\zeta'}$ and cast the original form in the more familiar one [128]

$$\sigma^{nd}_{\mu\nu}(\omega) = \frac{i\hbar e^2}{S_0} \sum_{\zeta \neq \zeta'} \frac{(f_\zeta - f_{\zeta'}) v_{\nu\zeta\zeta'} v_{\mu\zeta\zeta'}}{(E_\zeta - E_{\zeta'})(E_\zeta - E_{\zeta'} + \hbar\omega - i\Gamma)}, \tag{18}$$

where the sum runs over all quantum numbers $|\zeta\rangle \equiv |n, \mu, s, \tau, k_y\rangle$ and $|\zeta'\rangle \equiv |n', \mu', s', \tau', k'_y\rangle$

with $\zeta \neq \zeta'$. The infinitesimal quantity ϵ in the original form [128] has been replaced by $\Gamma_\zeta \approx \Gamma$ to account for the broadening of the energy levels. The familiar selection rules $n' = n \pm 1$ are obtained through an evaluation of velocity matrix elements, see Eqs. (20)- (21) below. In the zero-temperature limit the Fermi function can be replaced by a step function. Further, we assume positive values of E_F, so that all transitions to negative levels are Pauli blocked. In Eq. (18) $v_{\nu\zeta\zeta'}$ and $v_{\mu\zeta\zeta'}$ are the off-diagonal matrix elements of the velocity operator. They are evaluated using the operator expressions $v_x = \partial H/\partial p_x$ and $v_y = \partial H/\partial p_y$, and are given in terms of the Pauli matrices σ_v as

$$v_x = \tau v_F \begin{pmatrix} \sigma_x & 0 \\ 0 & \sigma_x \end{pmatrix}, \quad v_y = v_F \begin{pmatrix} \sigma_y & 0 \\ 0 & -\sigma_y \end{pmatrix}, \tag{19}$$

With $\varepsilon_{n,d_2} \equiv \varepsilon^{s,\tau}_{n,\mu} - d_2^{s\tau}$, $\varepsilon_{n,d_4} \equiv \varepsilon^{s,\tau}_{n,\mu} - d_4^{s\tau}$ and $Q = v_F \varrho^{s,\tau}_{n,\mu} \varrho^{s',\tau'}_{n',\mu'} \delta_{s,s'}$, and $R = k^{s,\tau}_{n,\mu}\, k^{s',\tau'}_{n',\mu'}$ the results are

$$\langle\zeta|\, v_x \,|\zeta'\rangle = \tau Q \Big[\sqrt{n+1}\,\Big(\frac{1}{\varepsilon'_{n,d_2}} + \frac{R}{\varepsilon_{n,d_4}}\Big)\delta_{n,n'-1} + \sqrt{n}\,\Big(\frac{1}{\varepsilon_{n,d_2}} + \frac{R}{\varepsilon'_{n,d_4}}\Big)\delta_{n,n'+1}\Big], \tag{20}$$

$$\langle\zeta'|\, v_y \,|\zeta\rangle = \tau i Q \Big[\sqrt{n+1}\,\Big(\frac{1}{\varepsilon'_{n,d_2}} + \frac{R}{\varepsilon_{n,d_4}}\Big)\delta_{n,n'-1} - \sqrt{n}\,\Big(\frac{1}{\varepsilon_{n,d_2}} + \frac{R}{\varepsilon'_{n,d_4}}\Big)\delta_{n,n'+1}\Big], \tag{21}$$

where $\mu = \{\mu_1, \mu_2\}$. Using Eqs. (20), (21), and (18) we obtain the real and imaginary parts of the conductivities $\sigma^{nd}_{xx}(\omega)$ and $\sigma^{nd}_{xy}(\omega)$ which for convenience and later purposes we write, setting $\Delta_{n,n+1} = \varepsilon^{s,\tau}_{n,\mu} - \varepsilon^{s,\tau}_{n+1,\mu}$, as

$$\begin{pmatrix} \mathrm{Re}\sigma^{nd}_{xx} \\ \\ \mathrm{Im}\sigma^{nd}_{xy} \end{pmatrix} = \mp\frac{e^2}{2h} \sum_{s,\tau,n,\mu,\mu'} \eta^{s,\tau}_{n,\mu,\mu'} \bar{\Gamma} \Big[\frac{1}{\big(\Delta_{n,n+1} + \bar{\omega}\big)^2 + \bar{\Gamma}^2} \pm \frac{1}{\big(\Delta_{n,n+1} - \bar{\omega}\big)^2 + \bar{\Gamma}^2}\Big], \tag{22}$$

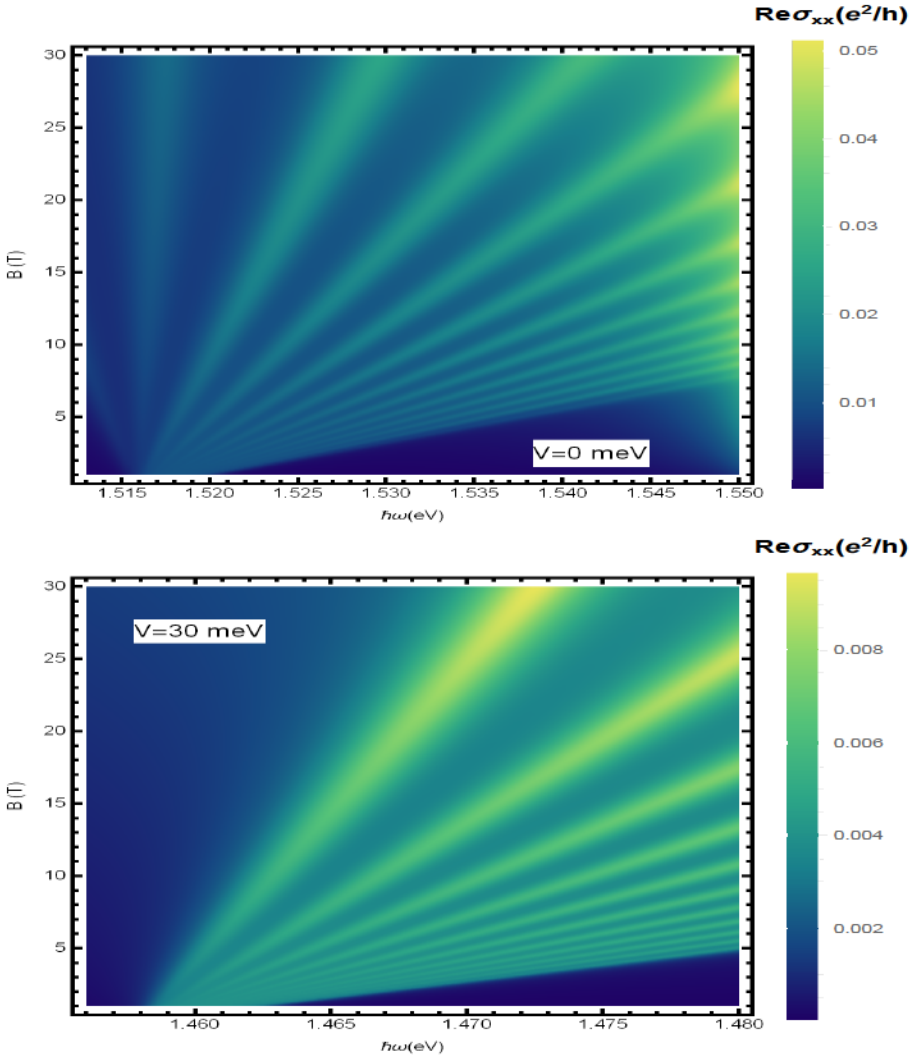

Figure 3.7: (B,ω) Contour plot of the real part of the longitudinal conductivity for $E_z = 0$ (upper panel) and $E_z \neq 0$ (lower panel). The level width Γ is set to $0.4\sqrt{B}$ meV.

$$\begin{pmatrix} \mathrm{Im}\sigma_{xx}^{nd} \\ \\ \mathrm{Re}\sigma_{xy}^{nd} \end{pmatrix} = -\frac{e^2}{2h} \sum_{s,\tau,n,\mu,\mu'} \eta_{n,\mu,\mu'}^{s,\tau} \left[\frac{\Delta_{n,n+1} + \bar{\omega}}{\left(\Delta_{n,n+1} + \bar{\omega}\right)^2 + \bar{\Gamma}^2} \mp \frac{\Delta_{n,n+1} - \bar{\omega}}{\left(\Delta_{n,n+1} - \bar{\omega}\right)^2 + \bar{\Gamma}^2} \right], \tag{23}$$

with

$$\eta_{n,\mu,\mu'}^{s,\tau} = (n+1)\left(\varrho_{n,\mu}^{s,\tau}\varrho_{n+1,\mu'}^{s,\tau}\right)^2 \left[\frac{k_{n,\mu}^{s,\tau}\, k_{n+1,\mu'}^{s,\tau}}{\varepsilon_{n,d_4}} + \frac{1}{\varepsilon_{n+1,d_2}} \right]^2 \frac{f(E_{n,\mu}^{s,\tau}) - f(E_{n+1,\mu'}^{s,\tau})}{\varepsilon_{n,\mu}^{s,\tau} - \varepsilon_{n+1,\mu'}^{s,\tau}}. \tag{24}$$

Here $\bar{\omega} \equiv \omega/\omega_c$ and $\bar{\Gamma} \equiv \Gamma/\hbar\omega_c$. The Fermi Dirac function at $T = 0$ becomes the Heaviside

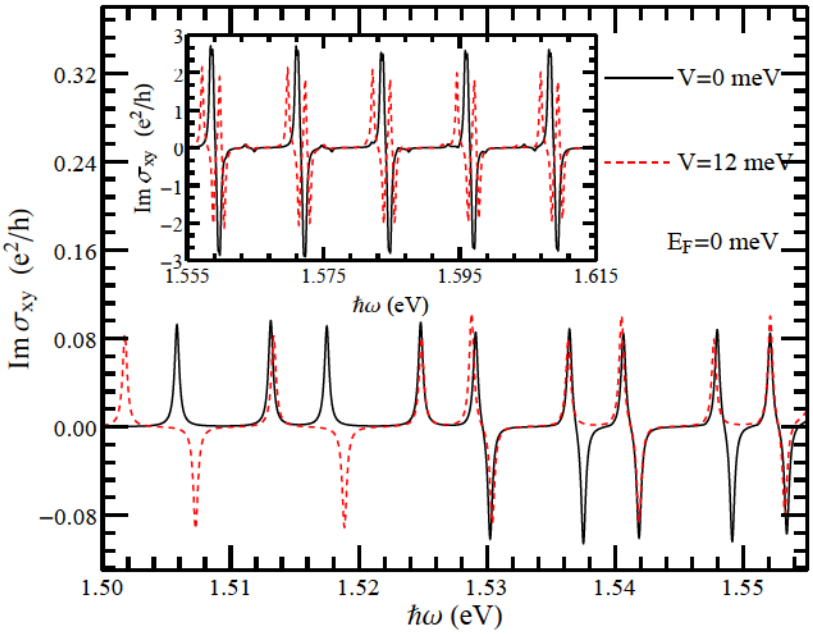

Figure 3.8: As in Fig. 3.5 but for Imσ_{xy}.

step function $\Theta(x)$ and enforces the Pauli exclusion principle for optical transitions, i.e., transitions occur only between the occupied n state and the unoccupied n' one. The $n = 0$ contributions to the absorptive conductivity Eq. (22) are evaluated separately. The results are given by Eq. (108) in Appendix A.

Notice that in the limit $\omega \to 0, \Gamma \to 0$ we have

$$\text{Re}\ \sigma_{xx}^{nd} = \text{Im}\ \sigma_{xx}^{nd} = \text{Im}\ \sigma_{xy}^{nd} = 0, \tag{25}$$

$$\text{Re}\ \sigma_{xy}^{nd} = -\frac{e^2}{h} \sum_{s,\tau,n,\mu,\mu'} \frac{\eta_{n,\mu,\mu'}^{s,\tau}}{\Delta_{n,n+1}}. \tag{26}$$

The electron energies are different than those of the holes due to Δ, the different values of the SOI and interlayer hopping (see Fig. 3.1). The terms intra-band and inter-band transitions refer to the bands in the absence of the magnetic field ($B = 0$). In bilayer WSe_2 they belong to totally different regimes because of $\hbar\omega_c << \Delta$: the intra-band transitions fall in the microwave-to-THz

regime and the inter-band ones in the visible frequency range because of the large value of the gap Δ. Unlike bilayer graphene-like 2D systems, the asymmetry between the CB and VB in the bilayer WSe_2 spectrum, due to the huge band gap and strong SOI, has important implications for the peaks seen in $\mathrm{Re}\sigma^{nd}_{xx}(\omega)$ and $\mathrm{Im}\sigma^{nd}_{xy}(\omega)$ as functions of the photon energy ($\hbar\omega$).

The absorptive part of the longitudinal conductivity is shown in Fig. 3.5 for a temperature $T = 0$ K and a level broadening $\Gamma = 0.04\sqrt{B}$ meV. A larger magnetic field ($B = 30$ T) has been used for well-resolved LL separation. The black solid and red dashed curves are for $E_z = 0$ and $E_z \neq 0$, respectively. Here, we took $E_F = 0$ eV in the gap. The optical selection rules allow n to change by only 1, see Eqs. (20) - (21). In addition, one needs to go from occupied (n) to unoccupied (n') states through the absorption of photons with transitions allowed only between same-spin states. For $E_z = 0$ and $E_z \neq 0$, the series of peaks occur at $\hbar\omega = -E^{s,\tau}_{n+1,-,\mu_2} + E^{s,\tau}_{n,+,\mu_2}$ and $\hbar\omega = -E^{s,\tau}_{n,-,\mu_2} + E^{s,\tau}_{n+1,+,\mu_2}$ for integer n. This series of peaks corresponds to the allowed inter-band transitions in the LL structure. As we can see from Fig. 3.5, the peaks are split due to the lifting of the spin and valley degeneracies in the presence of B and absence of E_z in contrast to the $B = 0$ case. The spin-up transitions $-n \to (n+1)$ in K (K') and spin-down ones $n \to -(n+1)$ in K (K') are suppressed as seen by the small peaks in Fig. 3.5. On the other hand, the large peaks correspond to the spin-down transitions $-n \to (n+1)$ in K (K') and the spin-up ones $n \to -(n+1)$ in K (K').

When the electric field is applied, the splitting of the peaks increases and the peaks move to lower energies as well as to higher energies. Further, the spin and valley responses switch their labels. The shifting of peaks to lower energies signals the reduction of the band gap between CB and VB as can be seen in Figs. 3.1 and 3.2. Moreover, the shifting of the peaks to higher energies signals an increase of the gap between the $E^{s,\tau}_{n,++}(E^{s,\tau}_{n,--})$ and $E^{s,\tau}_{n,+-}(E^{s,\tau}_{n,-+})$ bands (see Figs. 3.1 and 3.2). As the electric field is turned on, the intensity of the peaks is reduced due to a redistribution of the spectral weight between the peaks as shown by the red dotted curve in Fig. 3.5. In contrast to monolayer WSe_2 [53], σ_{xx} doesn't show any beating pattern at higher photon energies (not shown here) due to the well separated spin-up and spin-down states which do not mix at these frequencies. Another noteworthy point is that peak features in bilayer WSe_2 are completely different than in bilayer graphene [160] due to the lack of perfect symmetry between the positive and negative

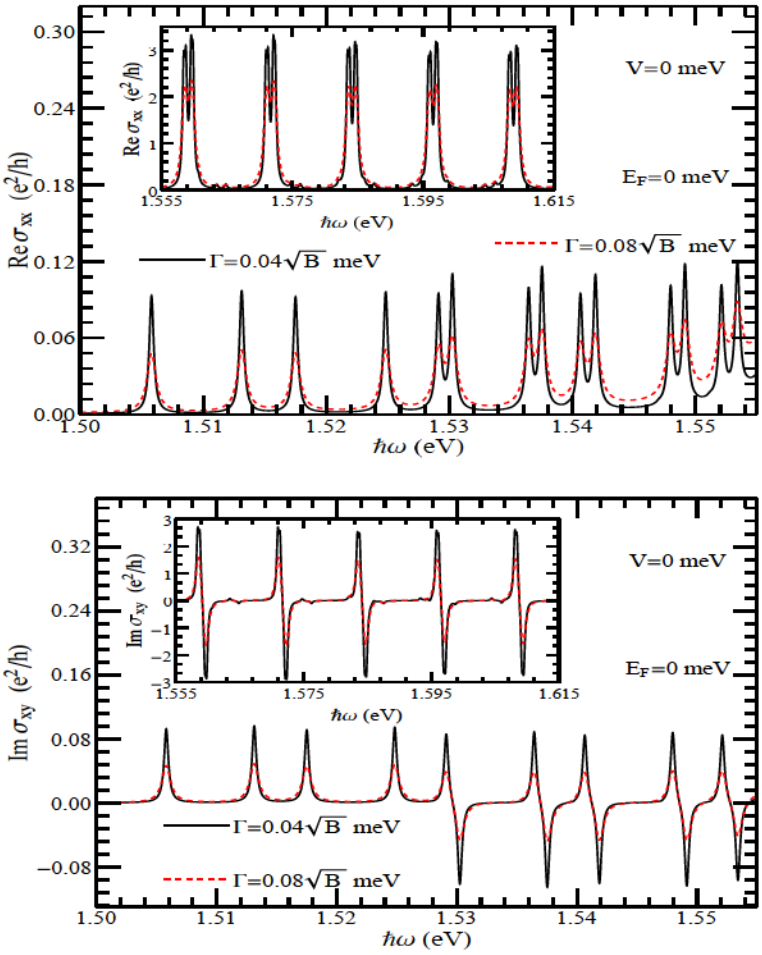

Figure 3.9: The real part of σ_{xx} (upper panel) and the maginary part of σ_{xy} (lower panel) vs $\hbar\omega$ for $V = 0$, $E_F = 0$ meV, $B = 30$ T, and two values of the level width Γ.

branches (see Fig. 3.1).

A magnetic and electric control of the valley polarization can be clearly seen as the corresponding peaks in two different valleys appear at different frequencies. In addition to the valley-controlled transport, the peaks in each valley split as a result of all LLs becoming spin split. The spin and valley splittings can be understood with the help of Eq. (22) and the corresponding energies. One noteworthy feature, that becomes clear by comparing the black and red curves of Fig. 3.5, is that the peaks are well separated for $E_z \neq 0$ in both spin and valley spaces. In massless Dirac systems [161], the spin and valley peaks occur at the same frequency and hence a series of four peaks is replaced by one peak in contrast to bilayer WSe_2 shown in Fig. 3.5. It is obvious from Fig. 3.5 that real absorptive part of σ_{xx} of the bilayer WSe has a much richer structure than its monolayer

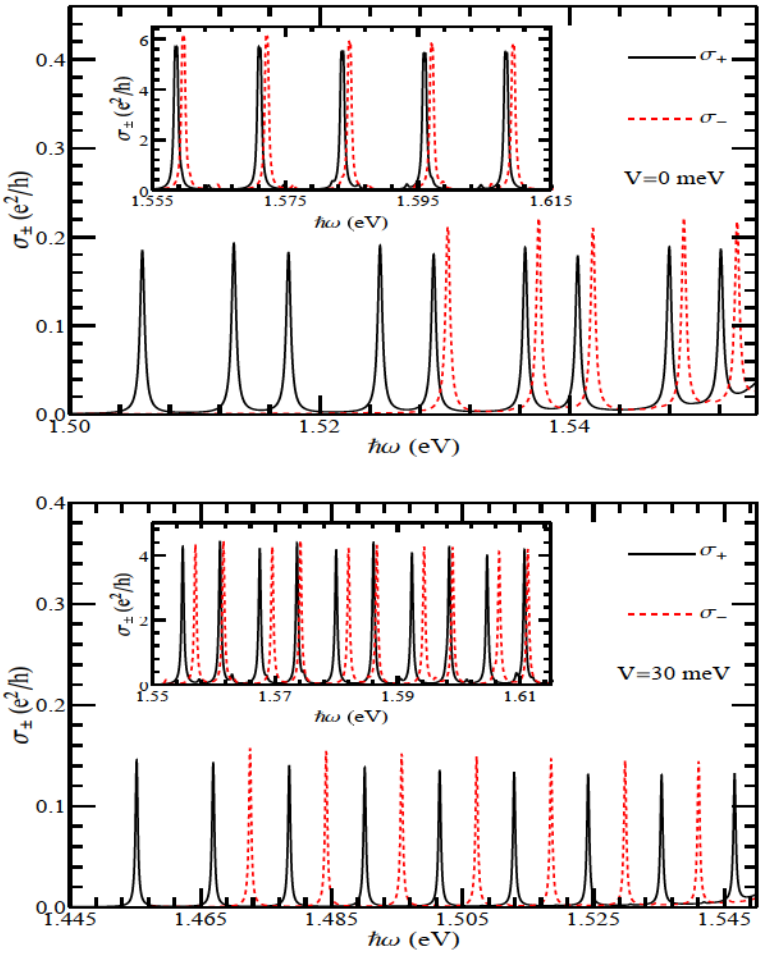

Figure 3.10: Real part of the right polarized optical conductivity $\sigma_+(\omega)$ and of the left polarized one $\sigma_-(\omega)$ vs $\hbar\omega$ for $E_F = 0$ meV and $B = 30$ T. The solid black curve and red dotted one are for $V = 0$ meV and $V = 30$ meV, respectively.

counterpart [53].

The effect of varying E_F is shown in Fig. 3.6 for $E_z = 0$. The value $E_F = 0.8358$ eV is situated between the $n = 0$ and $n = 1$ LLs, the first four peaks occurring at $\hbar\omega < 1.53$ eV are completely removed due to Pauli blocking while all others ($\hbar\omega > 1.53$ eV) occur at the same energies as in Fig. 3.5. This behaviour is opposite to that of other 2D materials [161, 162, 163, 164] like graphene, silicene, $\alpha - T_3$ and topological insulators, in which the spectral weight of the inter-band peaks is continuously redistributed into the intra-band ones. This shows how the conductivity changes as E_F moves through the LLs. Further, for $E_z \neq 0$ the lower peaks also disappear as E_F moves to higher LLs.

For simplicity, we show a (B, ω) contour plot of Reσ_{xx} only for the K valley in Fig. 3.7 versus B for two values of V: $V = 0$ meV (upper panel) and $V = 30$ meV (lower panel). In bilayer WSe_2, as might be expected from Eq. (8), all observed transition energies behave linearly with the magnetic field ($\propto \hbar^2\omega_c^2$). In contrast, in bilayer graphene [160] this occurs only for weak B fields, but it switches over to a $\sqrt{B}$ dependence as the corresponding energy goes out of the parabolic band region. Also, the slope of the transition energies depends on the LL index n. In weak fields, the peaks are smeared out more easily in bilayer WSe_2 than in its monolayer counterpart [53]. As expected, for $V \neq 0$, the peaks move to lower values of $\hbar\omega$ due to the reduction of the gap between the CB and VB (cf. lower panel of Fig. 3.7).

Figure 3.8 gives results for the Im σ_{xy} as a function of energy $\hbar\omega$ in eV. The symmetry between positive and negative branches is no longer observed due to the Δ and SOI terms in Eq. (6), and the peaks corresponding to the transitions $-n \to (n+1)$ and $n \to -(n+1)$ have slightly different energies. Also, we can see the splitting of the conductivity peaks due to these transitions. The strength of the splitting directly reflects the energy difference between the CB and VB branches for the same n. The consequences of this difference are even more striking for the Hall conductivity than it is for the longitudinal one. So, we can see this mismatch as emergence of positive and negative oscillations in conductivity. This behaviour can also be understood by the negative sign between the two terms of Eq. (22). For the massless Dirac case, the negative and positive peaks would have the same energy and hence cancel out perfectly. Furthermore, there are no downward peaks in the range $\hbar\omega < 1.53$ eV for $E_z = 0$ but there are when the field E_z is present.

In Fig. 3.9 we show the dependence of Reσ_{xx} and Imσ_{xy} on the values of Γ. The solid black curve is for broadening $\Gamma = 0.04\sqrt{B}$ meV and the red dotted one for $\Gamma = 0.08\sqrt{B}$ meV. The separation of the split peaks becomes narrow with increasing broadening Γ. By further increasing Γ, the splitting of the peaks disappears because the broadening covers the spacing between the spin-split LLs. To retain these peaks one has to apply a magnetic field for which the spin splitting exceeds the LL broadening $\Gamma \propto \sqrt{B}$. In other words, a large Γ smears out the peaks.

The peak structure just described above for Re $\sigma_{xx}^{nd}(\omega)$ and Im $\sigma_{xy}^{nd}(\omega)$ importantly affects the behaviour of the conductivity for right $(+)$ and left $(-)$ polarized light. For real experiments that probe the circular polarization of resonant light, as in the case of the Kerr and Faraday effects, one

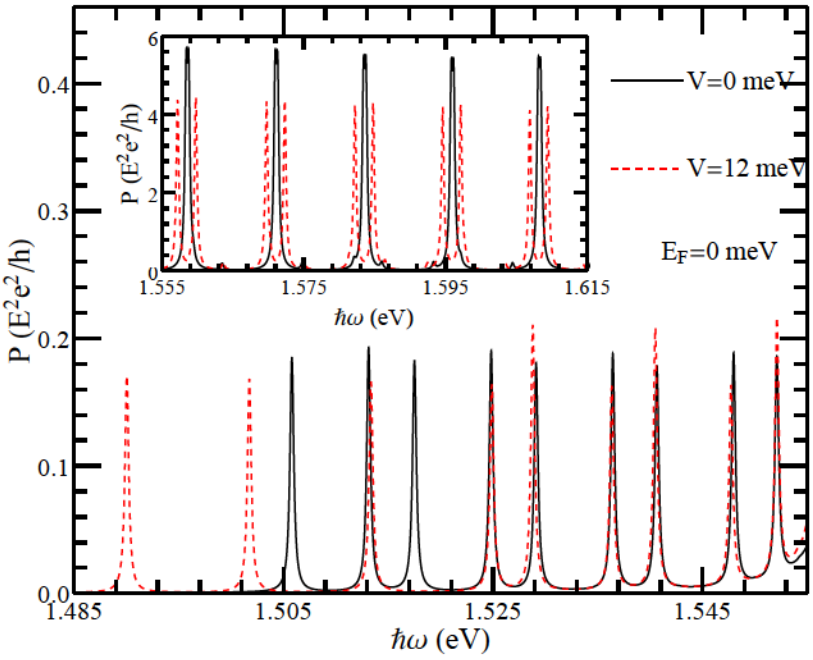

Figure 3.11: Power spectrum vs $\hbar\omega$ for $V = 0$ (black solid curve), $V = 12$ meV (dotted red curve), and field $B = 30$ T.

evaluates the quantity $\sigma_{\pm}(\omega)$ given by

$$\sigma_{\pm}(\omega) = \mathrm{Re}\sigma^{nd}_{xx}(\omega) \pm \mathrm{Im}\sigma^{nd}_{xy}(\omega), \tag{27}$$

with the $+(-)$ sign corresponding to the right (left) polarization. In Fig. 3.10 we show $\sigma_{-}(\omega)$ (dotted red curve) and $\sigma_{+}(\omega)$ (solid black curve) as functions of the frequency, for $E_F = 0.0$ eV in the gap, with $E_z = 0$ (upper panel) and $E_z \neq 0$ (lower panel), using the parameters of Fig. 3.5. As seen, there is a direct correspondence between these results and those of Figs. 3.5 and 3.8. The heights of the peaks for $E_z = 0$ and $E_z \neq 0$ in $\sigma_{-}(\omega)$ are slightly higher than those in $\sigma_{+}(\omega)$. Also, note that there is a double split-peak structure rather than a four split-peak structure as in $\sigma_{xx}(\omega)$. The peaks of $\sigma_{-}(\omega)$ and $\sigma_{+}(\omega)$ are displaced in energy with respect to each other. Similar to the behaviour of $\mathrm{Re}\sigma^{nd}_{xx}(\omega)$ and $\mathrm{Im}\sigma^{nd}_{xy}(\omega)$, the spin and valley splittings increase with E_z.

The difference between $\sigma_{-}(\omega)$ and $\sigma_{+}(\omega)$ is also reflected in the power absorption spectrum given by

$$P(\omega) = (E/2)\big[\sigma_{xx}(\omega) + \sigma_{yy}(\omega) - i\sigma_{yx}(\omega) + i\sigma_{xy}(\omega)\big]. \tag{28}$$

We recall that $\sigma_{\mu\nu} = \sigma^{d}_{\mu\nu} + \sigma^{nd}_{\mu\nu} = \sigma^{nd}_{\mu\nu}$ since the component $\sigma^{d}_{\mu\mu}$, $\mu = x, y$, vanishes. The component $\sigma^{nd}_{yy}(\omega)$ is given by $\sigma^{nd}_{xx}(\omega)$ and $\mathrm{Im}\sigma^{nd}_{xy}(\omega) = \mathrm{Im}\sigma^{nd}_{yx}(\omega)$. The spectrum $P(\omega)$ is shown in Fig. 3.11 as a function of the photon frequency for $E_z = 0$ and $E_z \neq 0$. Given that Im $\sigma^{nd}_{xy}(\omega)$ is the negative of Re $\sigma^{nd}_{xx}(\omega)$, see Eq. (22), the peaks in it are essentially the same as those in the longitudinal optical conductivity but positive and negative. Similar to $\mathrm{Re}\sigma^{nd}_{xx}(\omega)$ and $\mathrm{Im}\sigma^{nd}_{xy}(\omega)$, spin and valley splittings can be clearly seen in Fig. 3.11 and for $E_z \neq 0$ the separation between them increases.

The semiclassical limit of the magneto-optical conductivity occurs when the magnetic field is very weak and the spacing becomes inconsequential. This occurs for a large Fermi energy, $E_F \gg \varepsilon^{s,\tau}_{0,+-}$. For $E_F > 0$, only intra-band transitions are obtained between the nth and $(n+1)$th LLs in the CB. For $n \gg 0$, consider $E_F \approx E_{n,+,\mu_2}$ lies between the nth and $(n+1)$th LLs. In this limit, the energy spacing is linear in B in contrast to the $\sqrt{B}$ behaviour in Weyl semimetals [165]. The pertinent energy difference is $E_{n,+,\mu_2} - E_{n+1,+,\mu_2} = -\hbar\omega_c$.

We show the results of $\mathrm{Re}\sigma^{nd}_{xx}(\omega)$ for the intra-band case in Fig. 3.12. We see from the upper panel that there is a spectral weight redistribution to a strong intra-band response when E_F increased. Furthermore, the optical spectral weight under these curves increases with E_F in contrast to topological insulators [161]. Further, a double peak response is present in the strong intra-band response as the dashed red curve in the upper panel shows. This results from the spin splitting of the LLs that renders the spin levels at a given valley unequal in energy. Also, the separation between the double peaks (red dashed curve) increases with E_F. Similar to the monolayer WSe_2 [53], these peaks lie in the range of microwave-to-THz frequencies and their height is larger than that of the inter-band transitions shown in Figs. 3.5 - 3.11. Further, when we increase the magnetic field B, as seen in the lower panel of Fig. 3.12, the intra-band peaks move to higher energies and their height is reduced in contrast to massless Dirac materials [161, 162]. For large E_F the effect of E_z becomes inconsequential. These results are consistent with graphene-like 2D systems in which the relevant spectral weight increases with E_F, while the optical features in these 2D systems lie only in the THz regime [161, 162, 163, 164, 165].

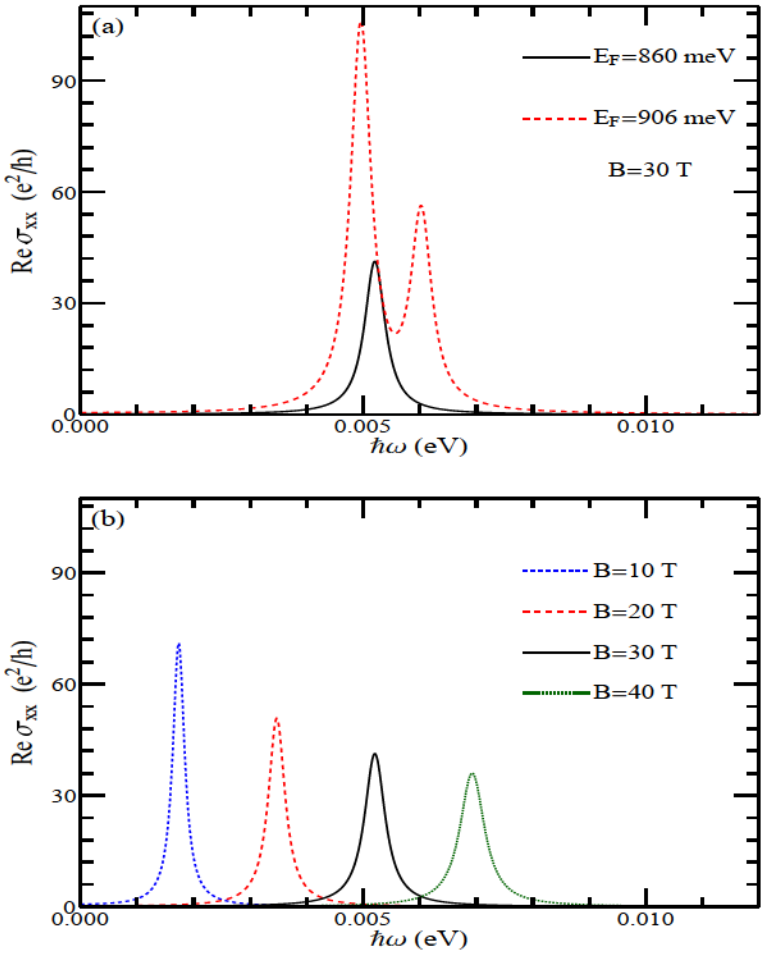

Figure 3.12: (a) Intra-band limit of the real part of the longitudinal conductivity versus photon energy $\hbar\omega$ for $B = 30$ T and two values of E_F. (b) As in (a) for four values of B and E_F close to 860 meV for $B \neq 30$ T. The energy $\hbar\omega$ is measured from the bottom of the conduction band.

3.5 Summary and conclusions

We have shown how the gap Δ and the SOI strength modify the electronic energy dispersion in bilayer WSe_2 , unlike bilayer graphene [119, 118], in the absence and presence of magnetic and electric fields. For $B = E_z = 0$ and $B \neq E_z \neq 0$, the energies of the levels in the conduction and valence bands no longer mirror each other, cf. Figs. 3.1 - 3.2. Further, we have studied the spin- and valley-controlled magnetotransport in the presence and absence of E_z. We point out that inter-band optical transitions from level n in the valence band to level $n + 1$ in the conduction band no longer have the same energy as those from level $n + 1$ to level n; this splits the corresponding absorption line in the real part of the longitudinal conductivity. Also, the optical spectral weight of these lines

is different (see the large and small peaks of Fig. 3.4) from that in graphene. The energy of the splitting is related to the mismatch in energy levels between the conduction and valence bands, see Fig. 3.2. A similar splitting was found for the imaginary part of the Hall conductivity.

Due to the large Δ, λ_c and λ_v terms, the conductivity peaks in WSe_2 depend linearly on B, contrary to bilayer graphene [160], and reflect the equidistant LLs in each band. In addition, the onset energies of the spin- and valley-dependent transitions reflect the energy difference between the LLs and are controlled by the magnetic and electric fields. The other determining factors are the band gap and the SOI strength. Accordingly, we may expect that a careful tuning of electric and magnetic fields will determine the value of band gap and SOI strength. However, for the absorption of circularly polarized light, two-peak structures are recovered but in this case there is a shift in the energy position and amplitude of the lines between right and left polarizations in contrast to what is found when the band gap and SOI terms in the electron dispersion curves are zero for graphene.

The semiclassical limit is affected by the magnetic field. This significantly shifts not only the intra-band peak to higher $\hbar\omega$ values, but also reduces the peak amplitude in contrast with graphene. The lineshape associated with the intra-band magneto-conductivity is significantly changed when the Fermi energy is varied. The optical spectral weight under these curves is found to increase in contrast to topological insulators and similar massless Dirac systems [161]. These novel findings may be pertinent to the development of spintronic and valleytronic optical devices based on bilayer TMDCs.

3.6 Acknowledgments

M. Z. and P. V. acknowledge the support of the Concordia University Grant No. OGP0121756 and a Concordia University Graduate Fellowship. The work of M. T. was supported by Colorado State University.

Chapter 4

Influence of interface induced valley-Zeeman and spin-orbit couplings on transport in heterostructures of graphene on WSe_2

4.1 Abstract

We investigate the electronic dispersion and transport properties of graphene/WSe_2 heterostructures in the presence of a proximity induced spin-orbit coupling (SOC) using a low-energy Hamiltonian, with different types of symmetry breaking terms, obtained from a four-band, first and second nearest-neighbour tight-binding (TB) one. The competition between different perturbation terms leads to inverted SOC bands. Further, we study the effect of symmetry breaking terms on ac and dc transport by evaluating the corresponding conductivities within linear response theory. The scattering-independent part of the valley-Hall conductivity, as a function of the Fermi energy E_F, is mostly negative in the ranges $-\lambda_R \leqslant E_F$ and $E_F \geqslant \lambda_R$ when the strength λ_R of the Rashba SOC increases except for a very narrow region around $E_F = 0$ in which it peaks sharply upward. The

scattering-dependent diffusive conductivity increases linearly with electron density, is directly proportional to λ_R in the low- and high-density regimes, but weakens for $\lambda_R = 0$. We investigate the optical response in the presence of a SOC-tunable band gap for variable E_F. An interesting feature of this SOC tuning is that it can be used to switch on and off the Drude-type intraband response. Furthermore, the ac conductivity exhibits interband responses due to the Rashba SOC. We also show that the valley-Hall conductivity changes sign when E_F is comparable to λ_R and vanishes at higher values of E_F. It also exhibits a strong dependence on temperature and a considerable structure as a function of the frequency.

4.2 Introduction

Two-dimensional (2D) materials have become a hot topic in solid state physics, especially since the discovery of graphene, both theoretically and experimentally because of their prominent mechanical, optical, electrical and magnetic properties [265]. Recently graphene has attracted a lot of attention in the field of spintronics due to its large electronic mobility, low spin-orbit coupling (SOC), negligible hyperfine interaction and gate tunability [266]. For a clear example, it has been proven that graphene exhibits a very long spin relaxation length even at room temperature [268, 269]. Due to the weak SOC though, it is not a suitable candidate for the observation of important spin-dependent phenomena including the spin-Hall effect [271] and anomalous Hall effect [272].

To render graphene useful in spintronics, several experimental groups used different techniques to tailor the SOC strength in it through coupling with foreign atoms or materials [273, 274, 276, 175, 176, 177, 178], such as graphene hydrogenation [179, 278] or fluorination [181] as well as heavy adatom decoration [182, 183]. However, these approaches not only reduce the transport quality, but also make it difficult to reproduce [179, 278] and detect [181, 182, 183] the induced SOC. To overcome these difficulties, graphene is recently grown on different novel 2D materials, which are ideal candidates to induce SOC via proximity effects [184, 185, 186, 187, 188, 189, 190]. Hexagonal boron nitride (BN) has a weak SOC, and therefore, is not a suitable substrate for the proximity effect [191]. The family of 2D transition metal dichalcogenides (TMDCs) are

the next best candidates, which have large direct band gaps and giant intrinsic SOC [44, 192]. In this respect, graphene on TMDCs has been investigated for transport [267, 194, 195] as well as intriguing technological applications, including field-effect tunnelling transistors (FETTs), radio-frequency oscillators, and efficient phototransistors [196, 82, 197, 198, 76, 80]. Also, the proximity-induced SOC in graphene/TMDCs heterostructures has recently been shown to depend [199, 200] on the twist angle between the lattice of graphene and that of the TMDC.

In addition, it has been found in room-temperature experimental studies of the spin-Hall effect that few-layer WS_2 induces a large SOC in graphene, about 17 meV [201] as compared to the very weak one in pristine graphene [202]. Also, it has been unambiguously demonstrated experimentally that a room-temperature spin-Hall effect in graphene is induced by MoS_2 proximity [203]. Moreover, when graphene is placed on a multilayer WS_2 substrate, an additional valley-Zeeman SOC, due to the broken sublattice symmetry, along with the Rashba SOC have been predicted theoretically and observed experimentally [190, 204, 205, 206]. This SOC induces a spin splitting of degenerate bands, with out-of-plane spin polarization at the K and K' points, and an opposite spin splitting in different valleys. Analogous to the Zeeman splitting, the SOC is termed valley-Zeeman because the effective Zeeman fields are valley-dependent. It is the dominant SOC in TMDCs and is also predicted to be induced in graphene on TMDCs [190, 204, 205, 206]. To our knowledge though, apart from some spin-transport studies [207] and two experimental magneto-transport studies [208], neither ac and dc scattering-dependent charge transport nor the simultaneous effect of valley-Zeeman and Rashba SOCs have been theoretically studied in graphene on TMDCs.

In this work we study in detail the effect of the valley-Zeeman and Rashba-type SOCs on ac and dc transport in graphene/WSe_2 heterostructures. There results a Mexican hat dispersion [209] contrary to other family memebers of TMDCs , e.g., MoS_2, WS_2 etc. [210]. Such a dispersion leads to more features in the optical conductivity when the Fermi level moves between the minimum and maximum of the Mexican hat. Also, we compare our results with those for pristine graphene.

In Sec. 4.3 we specify the Hamiltonian and obtain the eigenvalues and eigenfunctions in the presence of symmetry breaking terms. In Sec. 4.4 we present general expressions for the conductivities and provide numerical results. Conclusions and a summary follow in Sec. 4.5.

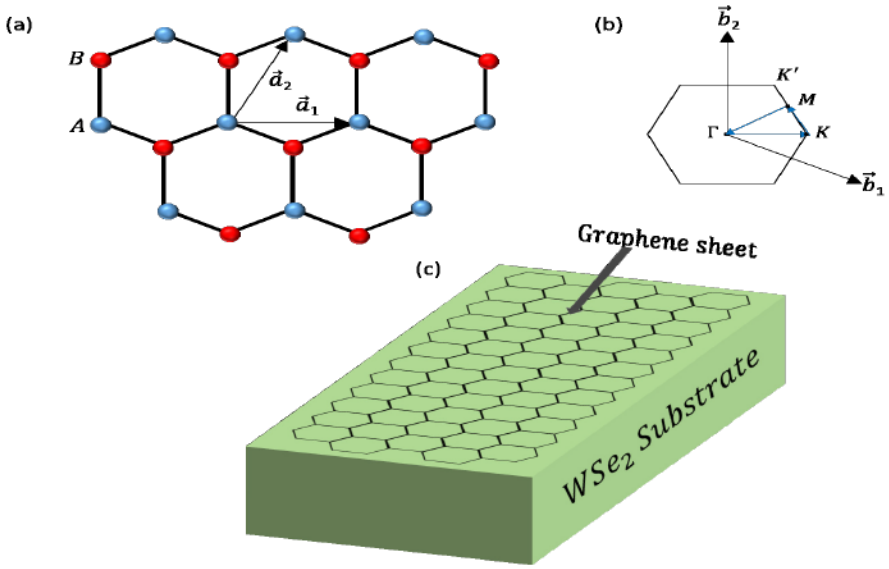

Figure 4.1: (a) Real-space graphene with $\vec{a}_1$ and $\vec{a}_2$ the primitive lattice vectors. (b) Graphene's first Brillouin zone and high symmetry points Γ, K, and M in reciprocal space. Its primitive lattice vectors are $\vec{b}_1$ and $\vec{b}_2$. (c) Schematic representation of graphene on a WSe_2 substrate.

4.3 Formulation

Graphene is a 2D, one-atom thick planar sheet of bonded carbon atoms densely packed in a honeycomb structure as shown in Fig. 4.1 (a). The lattice structure can be viewed as a triangular lattice with two sites A (red filled spheres) and B (blue filled spheres) per unit cell. The arrows indicate the primitive lattice vectors $\vec{a}_1 = a(1,0)$ and $\vec{a}_2 = a(1/2, \sqrt{3}/2)$, with a the triangular lattice constant of the structure, and span the graphene lattice. Further, $\vec{a}_1$ and $\vec{a}_2$ generate the reciprocal lattice vectors of the Brillouin zone, cf. Fig. 4.1 (b), given by $\vec{b}_1 = 4\pi/\sqrt{3}a(\sqrt{3}/2, -1/2)$ and $\vec{b}_2 = 4\pi/\sqrt{3}a(0,1)$. From the explicit expressions of $\vec{b}_1$ and $\vec{b}_2$ we find the two inequivalent Dirac points (valleys) given by $\vec{K} = (4\pi/3a)(1,0)$ and $\vec{K}' = (4\pi/3a)(1/2, \sqrt{3}/2)$.

The monolayer graphene system is described by the four-band, second nearest-neighbour tight-binding (TB) Hamiltonian [188, 209, 211]

$$H = -\sum_{\langle i,j\rangle,\alpha} t c^{\dagger}_{i\alpha} c_{j\alpha} + \sum_{i\alpha} \Delta \eta_{c_i} c^{\dagger}_{i\alpha} c_{i\alpha} + \sum_{\langle\langle i,j\rangle\rangle} \Delta_{ij} c^{\dagger}_{i\alpha} c_{j\alpha'} + \frac{2i}{3} \sum_{\langle i,j\rangle} \sum_{\alpha\alpha'} c^{\dagger}_{i\alpha} c_{j\alpha'} [\lambda_R (\boldsymbol{s} \times \hat{\mathbf{d}}_{ij})_z]_{\alpha\alpha'}. \tag{29}$$

Here $\Delta_{ij} = i\lambda_{c_i}\nu_{ij}s_z/3\sqrt{3}$, $c^{\dagger}_{i\alpha}$ creates an electron with spin polarization α at site i that belongs to

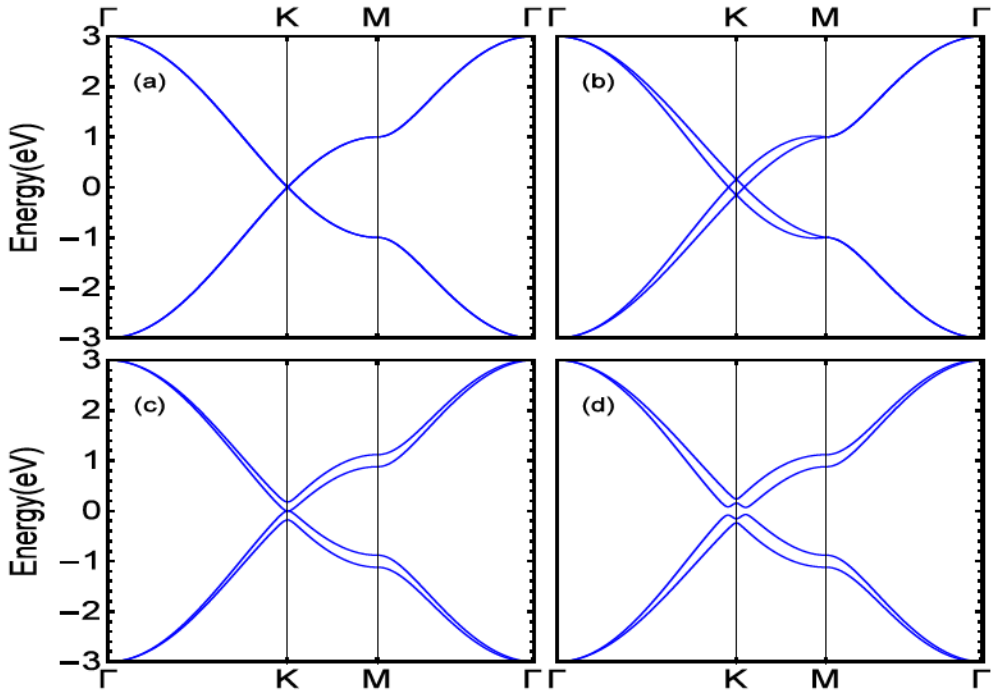

Figure 4.2: Energy dispersion in a graphene/WSe_2 heterostructure using the TB model (29) along the path $-M \rightarrow -K \rightarrow \Gamma \rightarrow K \rightarrow M$ for (a) $\lambda_{c_i}, \lambda_R = 0$, (b) $\lambda_{c_i} \neq 0, \lambda_R = 0$, (c) $\lambda_{c_i} = 0, \lambda_R \neq 0$, and (d) $\lambda_{c_i}, \lambda_R \neq 0$.

sublattice A or B, and $\langle i,j \rangle$ ($\langle\langle i,j \rangle\rangle$) runs over the nearest (second nearest) neighbouring sites. The second term is a staggered on-site potential, which takes into account the effective energy difference experienced by atoms at the lattice sites A ($\eta_{c_i} = +1$) and B ($\eta_{c_i} = -1$), respectively. The third and fourth terms represent the proximity-induced enhancement of the SOC due to a weak hybridization with the heavy atoms in WSe_2. The third term is the valley-Zeeman SOC where $\nu_{ij} = +1$, if the second nearest hopping is anticlockwise with respect to the positive z axis, and $\nu_{ij} = -1$ if it is clockwise. The last term is the Rashba SOC parametrized by λ_R. It arises because the inversion symmetry is broken when the graphene sheet is placed on top of WSe_2 as shown in Fig.5.2 (c). Also, $\hat{\mathbf{d}}_{ij} = \mathbf{d}_{ij}/|\mathbf{d}_{ij}|$, where $\boldsymbol{s} = (s_x, s_y, s_z)$ is the Pauli spin matrix and $\mathbf{d}_{ij}$ the vector connecting the sites i and j in the same sublattice.

In Fig. 4.2 we plot the numerically evaluated energy dispersion of Eq. (29) to better understand the characteristics of the induced intrinsic SOCs. Near the K point, for $\lambda_{c_i} = \lambda_R = 0$, the band

structure has linear band crossings near $k = 0$ as can be seen from Fig. 4.2 (a). For $\lambda_{c_i} \neq 0$ and $\lambda_R = 0$ the spectrum is gapless and the spin degeneracy is broken away from $k = 0$, see Fig. 4.2 (b). Further, if only λ_R is present, the spectrum is also gapless, cf. Fig. 4.2 (c). However, a gap is created when both λ_{c_i} and λ_R are finite, cf. Fig. 4.2 (d).

We analyze the physics of electrons near the Fermi energy using a low-energy effective Hamiltonian derived from Eq. (29) and a Dirac theory around the K and K' valleys [188, 204, 206]. It reads

$$H_\eta^s = v_F(\eta\sigma_x p_x + \sigma_y p_y) + \Delta\sigma_z + \lambda\sigma_0 s\eta + \lambda_R(\eta s_y\sigma_x - s_x\sigma_y). \tag{30}$$

Here $\eta = \pm 1$ denotes the valleys K and K', Δ is the mass term that breaks the inversion symmetry, $\lambda = \lambda_{c_i}$ is the valley-Zeeman SOC strength, λ_R the Rashba type SOC strength, (σ_x, σ_y, σ_z) the Pauli matrix that corresponds to the pseudospin (i.e., $A - B$ sublattice), σ_0 is the unit matrix in the sublattice space, and v_F (8.2×10^5 m/s) denotes the Fermi velocity of Dirac fermions. For simplicity, we neglect the intrinsic SOC λ_i and consider only the $\lambda_R > \lambda_i$ case. Also, we expect that small but finite values of λ_i do not qualitatively affect our results as long as $\lambda >> \lambda_i$. Further, we will also neglect the Δ term in our numerical treatment because $\lambda >> \Delta$.

Upon diagonalizing Eq. (30) we obtain the dispersion

$$E_\xi(k) = l\big[\Delta^2 + \lambda^2 + \hbar^2 v_F^2 k^2 + 2\lambda_R^2 + 2s\sqrt{\Upsilon}\,\big]^{1/2}, \tag{31}$$

where $\Upsilon = \lambda_R^2\left(\lambda_R^2 - 2\lambda\Delta\right) + \hbar^2 v_F^2 k^2\left(\lambda_R^2 + \lambda^2\right) + \lambda^2\Delta^2$ and $\xi = \{l, s\}$. Further, $l = +1(-1)$ denotes the conduction (valence) band and $s = +1(-1)$ represents the spin-up (spin-down) branches. Notice that Eq. (31) has a valley degeneracy despite the valley-Zeeman term. The normalized eigenfunctions for both valleys are

$$\psi_\xi^+(k) = \frac{N_\xi^+}{\sqrt{S_0}}\begin{pmatrix} 1 \\ A_\xi^\eta e^{i\phi} \\ -iB_\xi^\eta e^{i\phi} \\ -iC_\xi^\eta e^{2i\phi} \end{pmatrix} e^{i\mathbf{k}\cdot\mathbf{r}}, \qquad \psi_\xi^-(k) = \frac{N_\xi^-}{\sqrt{S_0}}\begin{pmatrix} -A_\xi^\eta e^{i\phi} \\ 1 \\ iC_\xi^\eta e^{2i\phi} \\ -iB_\xi^\eta e^{i\phi} \end{pmatrix} e^{i\mathbf{k}\cdot\mathbf{r}}, \tag{32}$$

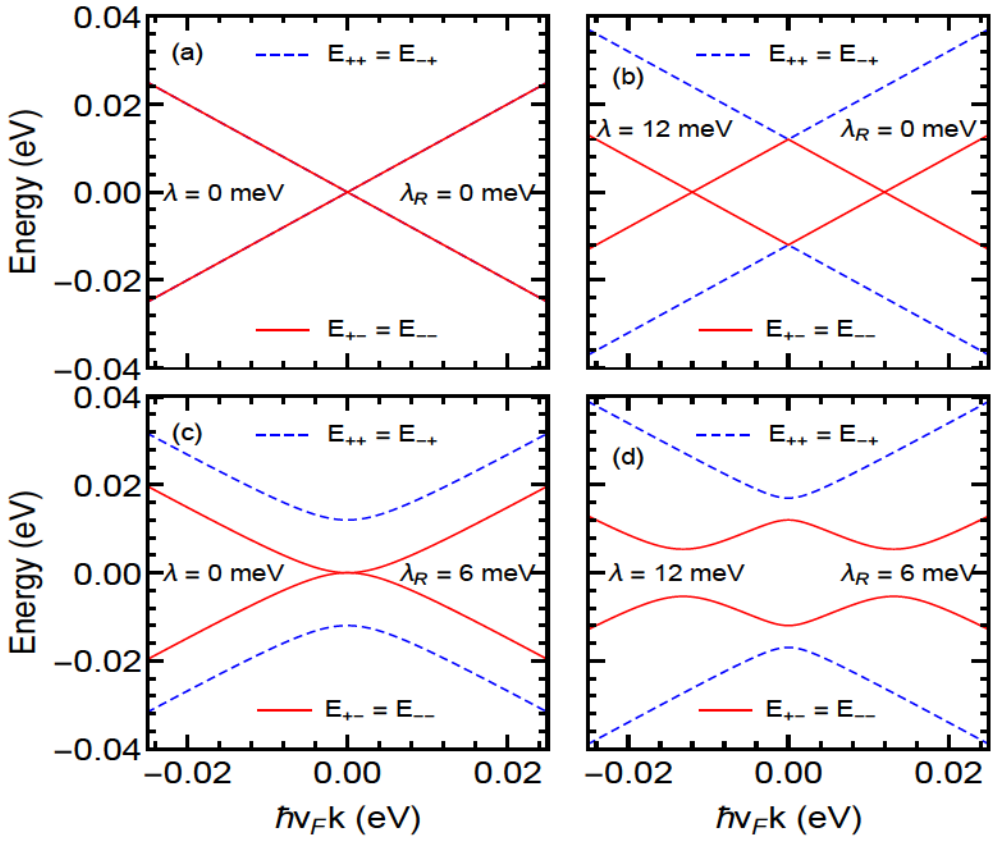

Figure 4.3: Low-energy dispersion in a graphene/WSe_2 heterostructure for $\Delta = 0$ and different combinations of λ and λ_R.

respectively, with

$$N_\xi^\eta = l\left[1 + (A_\xi^\eta)^2 + (B_\xi^\eta)^2 + (C_\xi^\eta)^2\right]^{-1/2}, \tag{33}$$

$S_0 = L_x L_y$ the area of the sample, and $\phi = \tan^{-1}(k_y/k_x)$. Further, $A_\xi^\eta = (E_\xi^\eta - \eta\Delta - \eta\lambda)/\hbar v_F k$, $B_\xi^\eta = 2\lambda_R\left[(E_\xi^\eta)^2 - (\Delta + \lambda)^2\right]/\hbar v_F k\left[(E_\xi^\eta + \eta\lambda)^2 - \Delta^2 - \hbar^2 v_F^2 k^2\right]$, and $C_\xi^\eta = 2\lambda_R(E_\xi^\eta - \eta\Delta - \eta\lambda)/\left[(E_\xi^\eta + \eta\lambda)^2 - \Delta^2 - \hbar^2 v_F^2 k^2\right]$.

We plot Eq. (31) in Fig. 4.3 for different combinations of the λ and λ_R terms whose realistic values fall in the ranges $5 - 6$ meV and $10 - 15$ meV, respectively, as determined experimentally in Ref. [212]. Here, the larger values of SOCs are used just to see well-resolved bands splitting. For $\lambda = \lambda_R = 0$, the band structure has linear bands crossing near $k = 0$ for both valleys as can be seen from panel (a). For $\lambda \neq 0$ and $\lambda_R = 0$, the energy dispersion is spin non-degenerate and valley

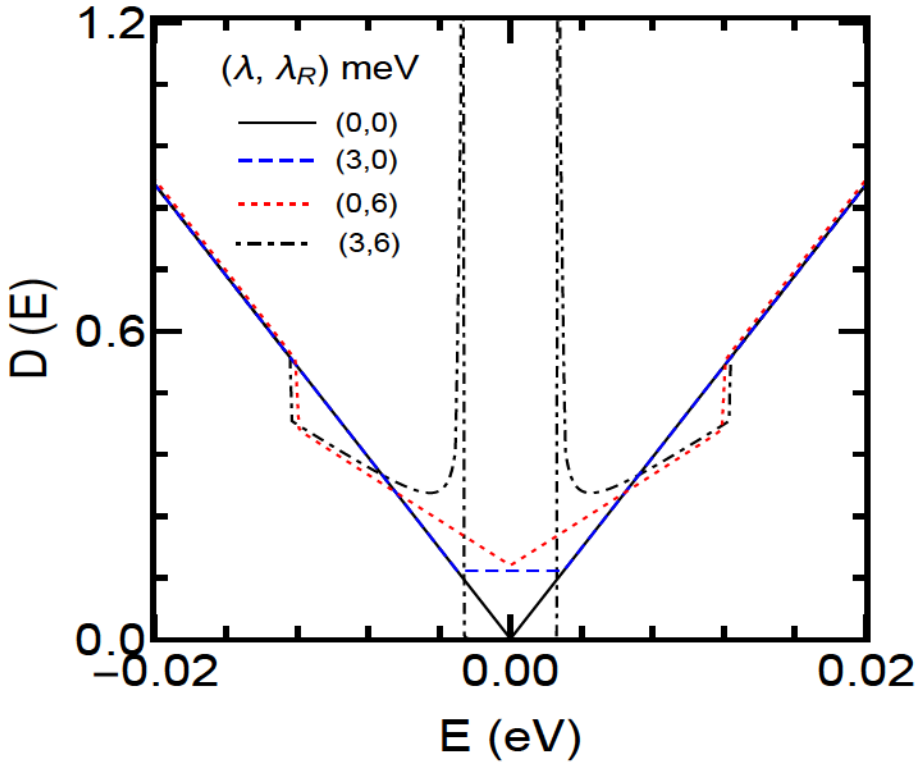

Figure 4.4: Density of states for $(\lambda, \lambda_R) = (0, 0)$, $(\lambda, \lambda_R) = (3, 0)$ meV, $(\lambda, \lambda_R) = (0, 6)$ meV and $(\lambda, \lambda_R) = (3, 6)$ meV. All cases are for $\Delta = 0$.

degenerate with a gapless behaviour as shown in panel (b). Further, the energy dispersion shows the gapless behaviour for $\lambda = 0$ and $\lambda_R \neq 0$ whereas it is spin-split as seen from panel (c). However, for λ and λ_R finite, the Rashba coupling not only creates a gap between the conduction and valence band, by mixing the spin-up and spin-down states, but also produces an avoided crossing, see Fig. 4.1 (d). The analytical form of the momentum k_1, at which an avoided crossing occurs, and of the gap $E_g = \Delta_1$ are

$$k_1 = \frac{1}{\hbar v_F}\Big[\frac{(\lambda^2 + \lambda\Delta)(\lambda^2 + 2\lambda_R^2 - \lambda\Delta)}{\lambda^2 + \lambda_R^2}\Big]^{1/2}, \tag{34}$$

$$\Delta_1 = 2\lambda_R\Big[\frac{\lambda^2 + \Delta(2\lambda + \Delta)}{\lambda^2 + \lambda_R^2}\Big]^{1/2}. \tag{35}$$

The density of states (DOS) per unit area corresponding to Eq. (31) is given by $D(E) =$

$\sum_\zeta \delta(E - E_\zeta)$ with $|\zeta\rangle = |\xi, \eta, k\rangle$. For $\lambda_R = 0$ it takes the simple form

$$D(E) = \frac{1}{2\pi\hbar^2 v_F^2} \sum_\xi \left| \frac{E}{l} - s\lambda \right| \Theta(\frac{E}{l} - s\lambda - \Delta), \tag{36}$$

and for $\Delta = \lambda = 0$ the form

$$D(E) = \frac{1}{2\pi\hbar^2 v_F^2} \sum_\xi \left| \frac{E}{l} - s\lambda_R \right| \Theta(\frac{E}{l} - (s+1)\lambda_R). \tag{37}$$

The DOS is shown in Fig. 4.4 for several values of λ and λ_R. The black curve is for monolayer graphene, with $\lambda = \lambda_R = 0$, and is included for comparison. The E_{+-} and E_{++} dispersions give rise to a square root singularity at $E = \lambda\lambda_R/\sqrt{\lambda^2 + \lambda_R^2}$ and a step at $E = \sqrt{\lambda^2 + 4\lambda_R^2}$, respectively, as shown by the black dot-dashed curve of Fig. 4.4. The origin of the singularity is the Mexican-hat energy dispersion, cf. Fig. 4.3. In addition, the step emerges from the bottom of the E_{++} band and is a van Hove singularity associated with the dispersion flattening at this point. The square root singularity is calculated near the Mexican-hat minimum $E = \lambda\lambda_R/\sqrt{\lambda^2 + \lambda_R^2}$ at which $D(E)$ reads

$$D(E) = \frac{k_1}{4\pi\hbar} \sqrt{\frac{2m^*}{E - \Delta_1}}, \tag{38}$$

with $m^* = \lambda_R(\lambda^2 + \lambda_R^2)^{3/2}/2v_F^2\lambda(\lambda^2 + 2\lambda_R^2)$ the effective mass and $E_{+,-} = \Delta_1 + (\hbar^2/2m^*)(k - k_1)^2$ the energy. This singularity is similar to that of the one-dimensional density of states. In the limit $\lambda_R = 0$ and $\lambda \neq 0$, the DOS has a finite value $\lambda/2\pi\hbar^2 v_F^2$ at $E = 0$ (see blue dashed curve). For $E \geqslant \lambda$, it increases linearly with E. Also, for $\lambda = 0$ and $\lambda_R \neq 0$, it is finite at $E = 0$ but has a step at $E = 2\lambda_R$, see the red dotted curve.

4.4 Conductivities

We consider a many-body system described by the Hamiltonian $H = H_0 + H_I - \mathbf{R} \cdot \mathbf{F}(t)$, where H_0 is the unperturbed part, H_I is a binary-type interaction (e.g., between electrons and impurities or phonons), and $-\mathbf{R} \cdot \mathbf{F}(t)$ is the interaction of the system with the external field F(t) [128]. For conductivity problems we have $\mathbf{F}(t) = e\mathbf{E}(t)$, where $\mathbf{E}(t)$ is the electric field, e the electron charge,

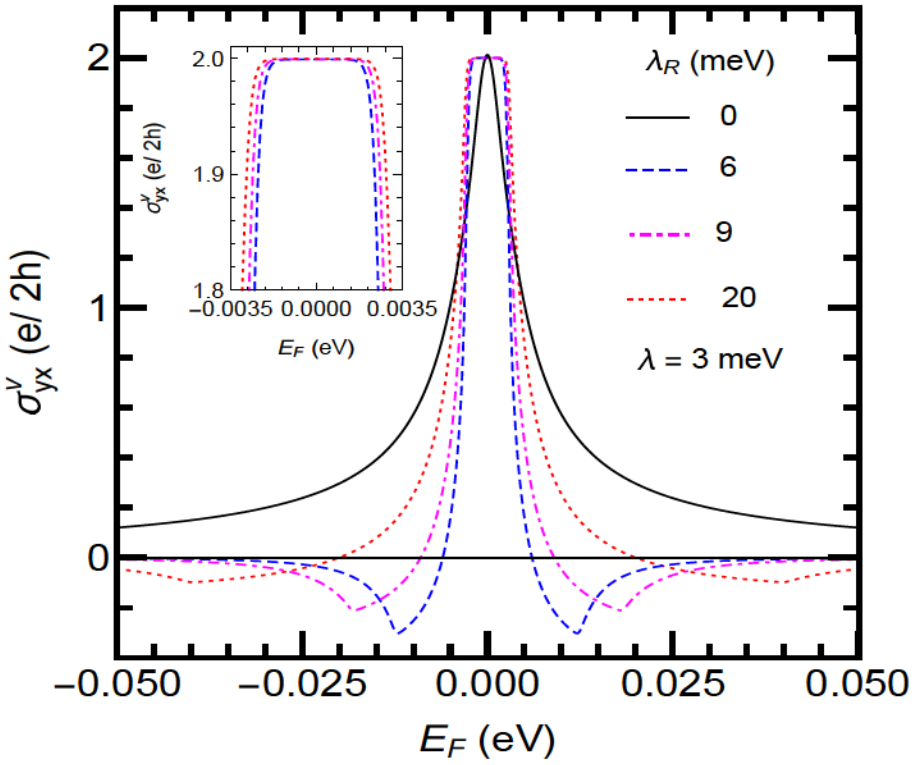

Figure 4.5: Valley-Hall conductivity versus Fermi energy at $T = 0.5$ K. For further clarity, the range -0.35 meV $\leq E_F \leq$ 0.35 meV is shown in the inset without the $\lambda_R = 0$ curve.

$\mathbf{R} = \sum_i \mathbf{r}_i$, and $\mathbf{r}_i$ the position operator of electron i. In the representation in which H_0 is diagonal the many-body density operator $\rho = \rho^d + \rho^{nd}$ has a diagonal part ρ^d and a nondiagonal part ρ^{nd}. For weak electric fields and weak scattering potentials, for which the first Born approximation applies, the conductivity tensor has a diagonal part $\sigma^d_{\mu\nu}$ and a nondiagonal part $\sigma^{nd}_{\mu\nu}$; the total conductivity is $\sigma^T_{\mu\nu} = \sigma^d_{\mu\nu} + \sigma^{nd}_{\mu\nu}, \mu, \nu = x, y$.

In general we have two kinds of currents, diffusive and hopping, with $\sigma^d_{\mu\nu} = \sigma^{dif}_{\mu\nu} + \sigma^{col}_{\mu\nu}$, but usually only one of them is present. If no magnetic field is present, the hopping term $\sigma^{col}_{\mu\nu}$ vanishes identically and only the term $\sigma^{dif}_{\mu\nu}$ survives. For elastic scattering it is given by [128]

$$\sigma^d_{\mu\nu}(\omega) = \frac{\beta e^2}{S_0} \sum_\zeta f_\zeta (1 - f_\zeta) \frac{v_{\nu\zeta}\, v_{\mu\zeta}\, \tau_\zeta}{1 + i\omega\tau_\zeta}, \tag{39}$$

with τ_ζ the momentum relaxation time, ω the frequency, and $v_{\mu\zeta}$ the diagonal matrix elements of the velocity operator. Further, $f_\zeta = \left[1 + \exp[\beta(E_\zeta - E_F)]\right]^{-1}$ is the Fermi-Dirac distribution function,

Table 4.1: Band gap energies involved in optical transitions, cf. Fig. 4.7, for $\lambda = 8$ meV, $\lambda_R = 6$ meV, and two values of E_F. Also, $M = \sqrt{(\lambda^2+\lambda_R^2)E_F^2 - \lambda^2\lambda_R^2}$ and $L = \sqrt{\lambda_R^4 + (\lambda^2+\lambda_R^2)(E_F^2+\lambda^2 \pm 2M)}$.

Transition energies	Formula	$E_F = 6.6$ meV	$E_F = 9.6$ meV
Δ_1	$2\lambda\lambda_R/\sqrt{\lambda^2+\lambda_R^2}$	9.6	9.6
Δ_2	$2\sqrt{(4\lambda^4+4\lambda_R^4+9\lambda^2\lambda_R^2)/(\lambda^2+\lambda_R^2)}$	41.2	41.2
Δ_{01}	2λ	16	16
Δ_{02}	$2\sqrt{\lambda^2+4\lambda_R^2}$	28.8	28.8
Δ_a	$2\sqrt{2\lambda^2+2\lambda_R^2+E_F^2-2M-2L}$	32.2	
Δ_b	$2\sqrt{2\lambda^2+2\lambda_R^2+E_F^2+2M+2L}$	50	57.4

$\beta = 1/k_BT$ and T the temperature.

Regarding the contribution $\sigma_{\mu\nu}^{nd}$ one can use the identity $f_\zeta(1-f_{\zeta'})\left[1-\exp[\beta(E_\zeta - E_{\zeta'})]\right] = f_\zeta - f_{\zeta'}$ and cast the original form in the more familiar one [128]

$$\sigma_{\mu\nu}^{nd}(\omega) = \frac{i\hbar e^2}{S_0}\sum_{\zeta\neq\zeta'}\frac{(f_\zeta - f_{\zeta'})\, v_{\nu\zeta\zeta'}\, v_{\mu\zeta\zeta'}}{(E_\zeta - E_{\zeta'})(E_\zeta - E_{\zeta'} + \hbar\omega - i\Gamma)}, \tag{40}$$

where the sum runs over all quantum numbers ζ and ζ' with $\zeta \neq \zeta'$. The infinitesimal quantity ϵ in the original form has been replaced by Γ_ζ to account for the broadening of the energy levels. In Eq. (40) $v_{\nu\zeta\zeta'}$ and $v_{\mu\zeta\zeta'}$ are the off-diagonal matrix elements of the velocity operator. The relevant velocity operators are given by $v_x = \partial H/\hbar\partial k_x$ and $v_y = \partial H/\hbar\partial k_y$. With $\zeta = \{l, s.k, \eta\} = \{\xi, k, \eta\}$ for brevity, they read

$$\langle\zeta|\, v_x\, |\zeta'\rangle = v_F N_\xi^\eta N_{\xi'}^\eta (D_{\xi,\xi'}^\eta e^{i\phi} + F_{\xi,\xi'}^\eta e^{-i\phi})\delta_{k,k'}, \tag{41}$$

$$\langle\zeta'|\, v_y\, |\zeta\rangle = iv_F N_\xi^\eta N_{\xi'}^\eta (D_{\xi,\xi'}^\eta e^{-i\phi} - F_{\xi,\xi'}^\eta e^{i\phi})\delta_{k,k'}, \tag{42}$$

where $D_{\xi,\xi'}^\eta = A_{\xi'}^\eta + B_\xi^\eta C_{\xi'}^\eta$ and $F_{\xi,\xi'}^\eta = A_\xi^\eta + B_{\xi'}^\eta C_\xi^\eta$.

We now calculate the conductivity $\sigma_{yx}^{nd}(i\omega)$ given by Eq. (40). Further, the velocity matrix elements (41) and (42) are diagonal in k, therefore k will be suppressed in order to simplify the

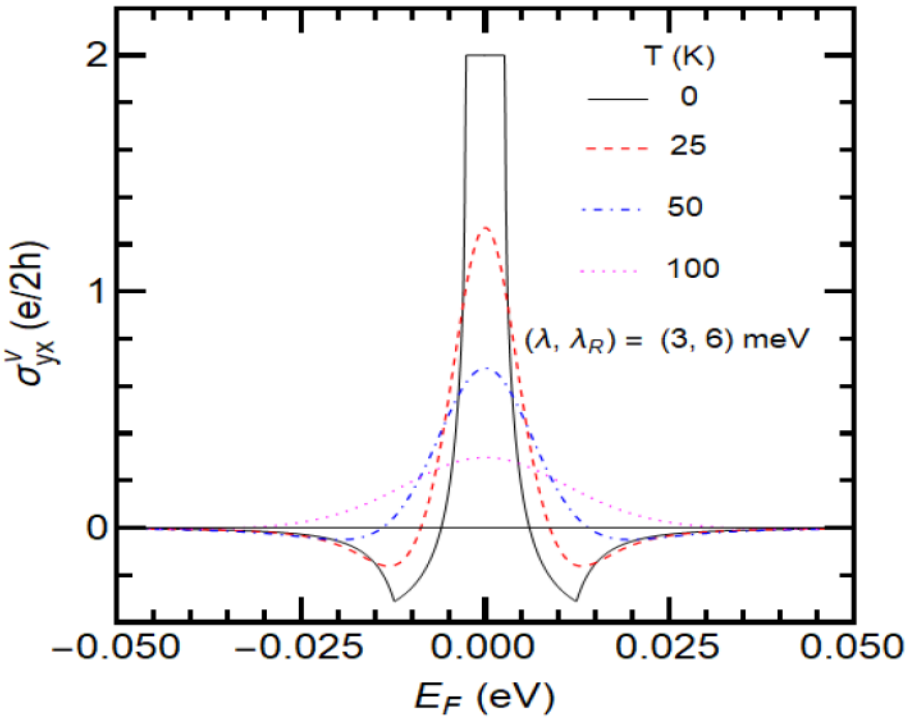

Figure 4.6: Same as in Fig. 4.5 but for different values of T.

notation. The summation in Eq. (40) runs over all quantum numbers ξ,ξ', η, η', and k. The parameter $\Gamma^{\xi\xi'}_{\eta\eta'}$, that takes into account the level broadening, is assumed to be independent of the band and valley indices, i.e., $\Gamma^{\xi\xi'}_{\eta\eta'} = \Gamma$. Using Eqs. (41) and (42) we can express Eq. (40) as

$$\begin{aligned}\sigma^{nd}_{yx}(i\omega) &= \frac{e^2\hbar^2 v_F^2}{h}\sum_{\xi\xi'}\int dkk\,\frac{(N^\eta_\xi N^\eta_{\xi'})^2(f^\eta_{\xi k}-f^\eta_{\xi' k})}{\Delta^\eta_{\xi\xi'}\left[(\Delta^\eta_{\xi\xi'}+\hbar\omega)^2+\Gamma^2\right]}\left[\Delta^\eta_{\xi\xi'}+\hbar\omega-i\Gamma)\right] \\ &\quad\times\left[D^\eta_{\xi,\xi'})^2-(F^\eta_{\xi,\xi'})^2\right] \qquad (43)\end{aligned}$$

where $\Delta^\eta_{\xi\xi'} = E^\eta_{\xi k} - E^\eta_{\xi' k}$. Further, in the limit $\Gamma = \omega = 0$, Eq. (43) reduces to

$$\sigma^{nd}_{yx} = \frac{e^2\hbar^2 v_F^2}{h}\sum_{\xi\xi'}\int dkk\,\frac{(N^\eta_\xi N^\eta_{\xi'})^2(f^\eta_{\xi k}-f^\eta_{\xi' k})}{(\Delta^\eta_{\xi\xi'})^2}\left[(D^\eta_{\xi,\xi'})^2-(F^\eta_{\xi,\xi'})^2\right] \qquad (44)$$

In the valley-Hall effect electrons from regions near the inequivalent K and K' valleys flow to opposite transverse edges of the system, in the presence of SOCs when a longitudinal electric field is applied [129, 130]. Further, one can probe the valley-Hall effect by measuring the Berry curvature

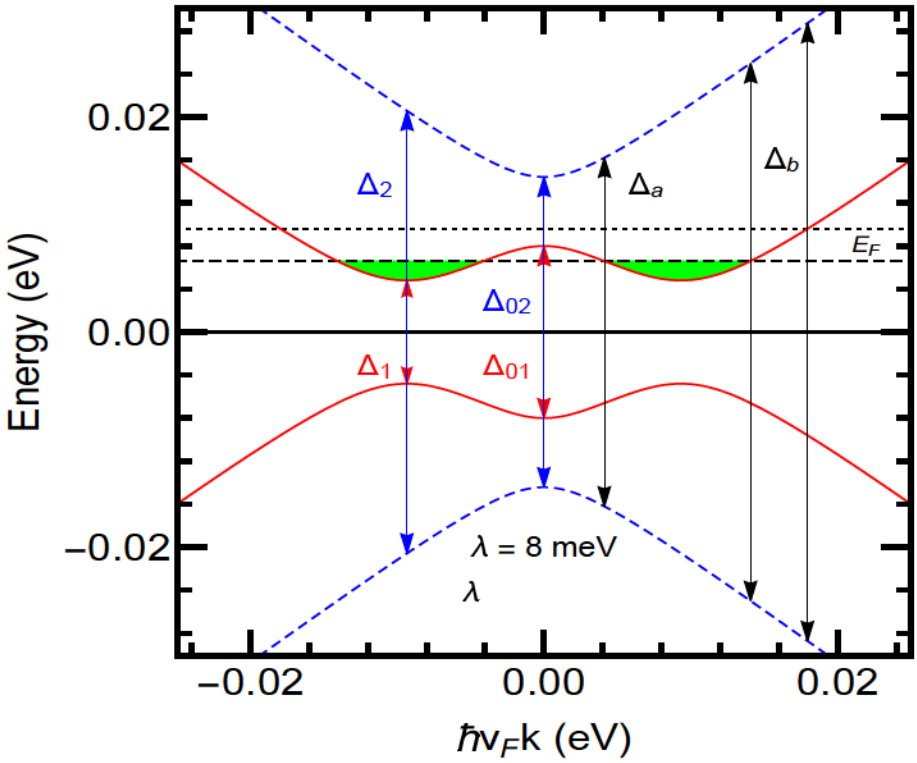

Figure 4.7: Band structure near the Fermi energy E_F in the presence of SOC terms for $\lambda = 8$ meV and $\lambda_R = 6$ meV. The black dashed and dotted lines show $E_F = 6.6$ meV and $E_F = 9.6$ meV. The various gap energies, indicated by Δ_1, Δ_2, etc. are displayed in table 4.1. Notice that for $E_F = 9.6$ meV the energy Δ_a does not contribute to any transitions.

associated with the Bloch electrons [59]. The valley-Hall conductivity corresponding to Eq. (43) is defined by

$$\sigma^v_{yx} = \sum_{ss'} \sigma^{nd}_{yx}(\eta = +, s, s') - \sigma^{nd}_{yx}(\eta = -, s, s'). \tag{45}$$

The spin-Hall conductivity σ^s_{yx}, corresponding to Eq. (43), is finite only when both the Kane-Mele and valley- Zeeman SOCs are present. Hence, even in the presence of Rashba SOC, σ^s_{yx} vanishes [203]. Since a spin current is defined by $\mathbf{J_s} = (\hbar/\mathbf{2e})(\mathbf{J}_\uparrow - \mathbf{J}_\downarrow)$, we have to multiply σ^v_{yx} by $1/2e$ [271, 213]. Further, we find that charge Hall conductivity always vanishes

$$\sigma^c_{yx} = \sum_{\eta ss'} \sigma^{nd}_{yx}(\eta, s, s') = 0 \tag{46}$$

The component $\sigma^{nd}_{xx}(i\omega)$ is also obtained from Eq. (40):

$$\sigma^{nd}_{xx}(i\omega) = \frac{ie^2\hbar^2v_F^2}{h}\sum_{\eta\xi\xi'}\int dkk\,\frac{(N^\eta_\xi N^\eta_{\xi'})^2(f^\eta_{\xi k}-f^\eta_{\xi' k})}{\Delta^\eta_{\xi\xi'}\left[(\Delta^\eta_{\xi\xi'}+\hbar\omega)^2+\Gamma^2\right]}\left[\Delta^\eta_{\xi\xi'}+\hbar\omega-i\Gamma)\right] \times\left[D^\eta_{\xi,\xi'})^2+(F^\eta_{\xi,\xi'})^2\right]. \quad (47)$$

For $\lambda=0$ and $\lambda_R\neq 0$, Eq. (43) vanishes because the factor $(D^\eta_{\xi,\xi'})^2-(F^\eta_{\xi,\xi'})^2$ becomes zero, whereas Eq. (47) survives. Moreover, in the limit $\lambda=\lambda_R=0$, Eq. (47) reduces to the optical conductivity of pristine graphene, which is independent of $\hbar\omega$ and given by $e^2/2h$ [214].

We now consider the diagonal component σ^d_{xx} given by Eq. (39). Using Eq. (41), with $\xi=\xi'$, we obtain

$$\sigma^d_{xx}(i\omega) = \frac{e^2v_F^2\beta}{\pi}\sum_{\eta\xi}\int dkk\,(N^\eta_\xi)^4 f^\eta_{\xi k}(1-f^\eta_{\xi k})\frac{(A^\eta_\xi+B^\eta_\xi C^\eta_\xi)^2\,\tau^\eta_{\xi k}}{1+i\omega\tau^\eta_{\xi k}} \quad (48)$$

At very low temperatures we can make the approximation $\beta f^\eta_{\xi k}(1-f^\eta_{\xi k})\approx\delta(E_\xi-E_F)$ and $\tau^\eta_{\xi k}=\tau^\eta_{\xi k_F}$ because all states untill the Fermi level are occupied.

In Fig. 4.5 we plot Eq. (43) in the dc limit ($\omega=0$) as a function of E_F for $\Gamma=0.2$ meV, $\lambda=3$ meV and for different values of λ_R. When E_F is in the gap, i.e., in the range $-\lambda\lambda_R/\sqrt{\lambda^2+\lambda_R^2}\leqslant E_F\leqslant\lambda\lambda_R/\sqrt{\lambda^2+\lambda_R^2}$, the valley-Hall conductivity is quantized in units of $2e/2h$ similar to the case of gapped graphene and topological insulators [130, 215]. The reason is that the factor $\sum_{\eta\xi\xi'}(N^\eta_\xi N^\eta_{\xi'})^2[(D^\eta_{\xi,\xi'})^2-(F^\eta_{\xi,\xi'})^2]/(\Delta^\eta_{\xi\xi'})^2$, called Berry curvature $\Omega(k)$, of Eq. (43) in the limit $\omega=0$ has a peak, which is well covered by occupied states for $E_F>\lambda\lambda_R/\sqrt{\lambda^2+\lambda_R^2}$. As a consequence, the valley-Hall conductivity approaches the quantized value. For $\lambda\lambda_R/\sqrt{\lambda^2+\lambda_R^2}\leqslant E_F\leqslant\lambda_R$, σ^v_{yx} decreases with E_F. Further, as can be seen, when E_F becomes comparable to λ_R, a sign change occurs in the conductivity which later vanishes at higher values of E_F, $E_F>>\sqrt{\lambda^2+4\lambda_R^2}$. The change in sign is due to the Rashba coupling between the spin-up and spin-down bands. Furthermore, this off-diagonal term in spin space permits transitions between two conduction spin subbands (see Eq. (31)), that could be interpreted as spin-flip transitions near the band touching. In addition, the coupling strength between opposite spin bands becomes weaker as λ_R increases. As a result, the negative part of the conductivity due to the spin-up band diminishes and σ^v_{yx} shows

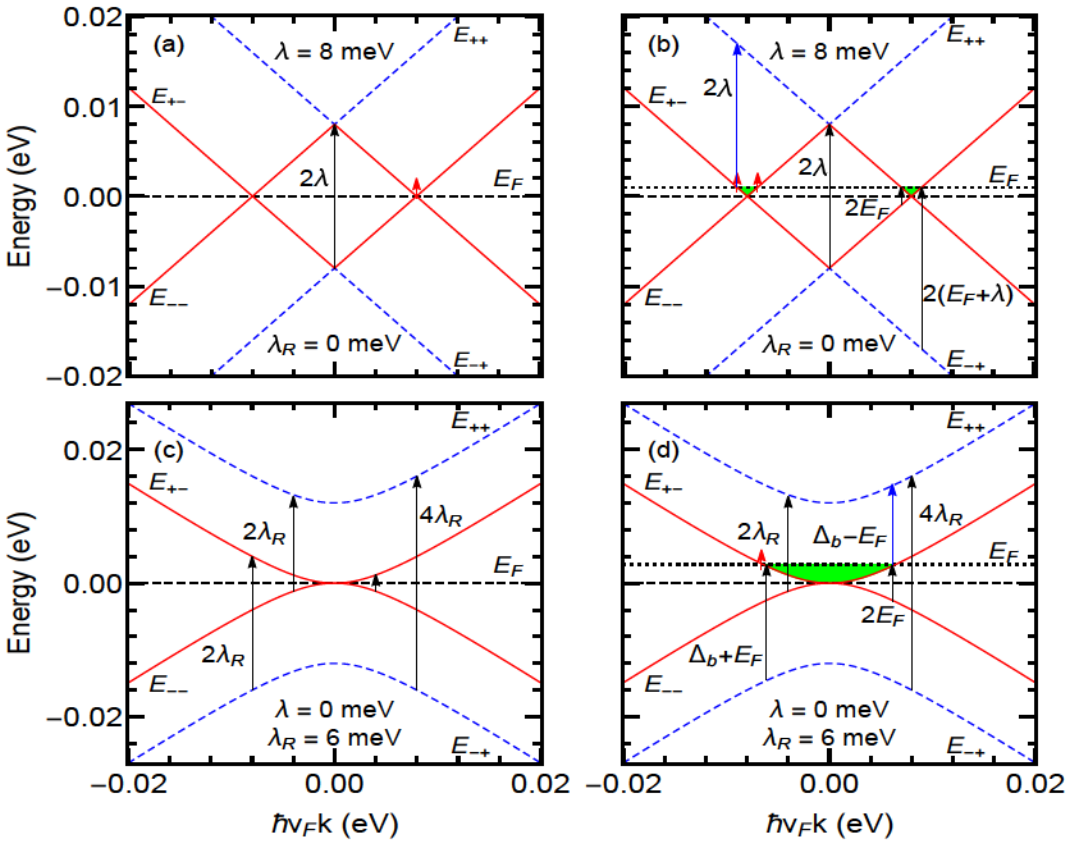

Figure 4.8: Band structure near the Fermi energy E_F in the presence of SOC terms for $\lambda = 8$ meV and $\lambda_R = 6$ meV. Black and red arrows represent possible interband transitions. Red arrows indicate the Drude type intraband transitions. (a) $\lambda \neq 0$, $\lambda_R, E_F = 0$. (b) $\lambda \neq 0$, $\lambda_R = 0$, $E_F = 1$ meV. (c) $\lambda_R \neq 0$, $\lambda, E_F = 0$. (d) $\lambda_R \neq 0$, $\lambda_R = 0$, $E_F = 2.8$ meV.

the usual behaviour of gapped graphene and topological insulators [130, 215]. Further, as can be seen in the inset, the band gap increases with λ_R. Also, the value of the conductivity at $E_F = 0$ is due to the finite one of Γ (= 0.2 meV); if we take $\Gamma = 0$, the conductivity diverges at $E_F = 0$ but its overall qualitative behavior remains as shown.

We now take into account the effect of temperature T on the valley-Hall conductivity contained in the Fermi function, which is independent of electron-phonon interaction in the first Born approximation [128]. The valley-Hall conductivity is evaluated numerically with the help of Eq. (43) and plotted in Fig. 4.6 for four values of T. We find a strong T dependence, particularly when the Fermi level is in the gap. The quantization of the valley-Hall conductivity is destroyed at high values of T. This occurs when the thermal broadening k_BT becomes comparable to the energy gap. Notice that the effect of temperature on σ^v_{yx} is similar to that on the spin-Hall conductivity in a graphene/MoS_2

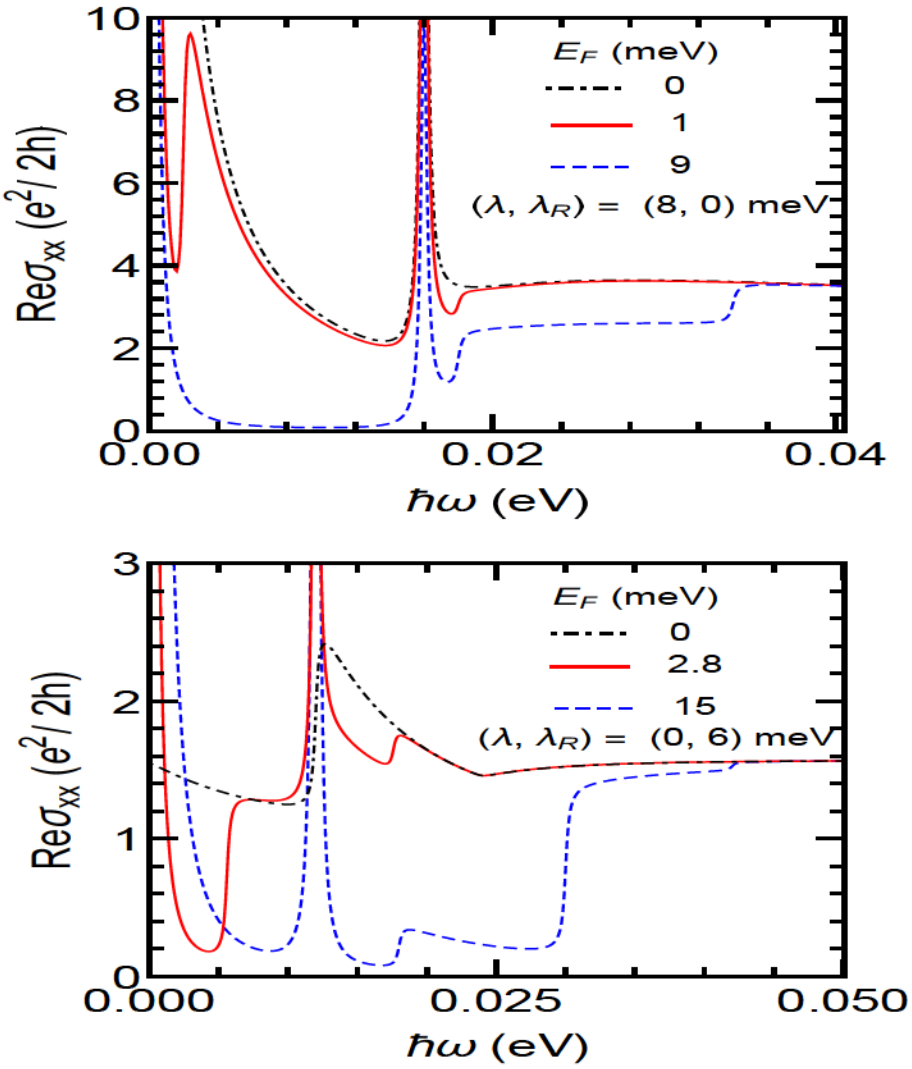

Figure 4.9: Real part of longitudinal conductivity versus photon energy at $T = 0.5$ K. The upper panel is for $\lambda_R = 0$ and the lower one is for $\lambda_R \neq 0$.

heterostructure by considering valley-Zeeman and Kane-Mele SOCs in the absence of the Rashba SOC.

Various transition energies, which play an important role in the optical conductivity, are shown in Fig. 4.7 for $\lambda, \lambda_R \neq 0$. Their analytical expressions are displayed in table 4.1. Notice that for $E_F = 6.6$ meV, the energies Δ_a and Δ_b, indicated with black arrows, become also important in optical transitions, since E_F crosses the curve E_{+-} at two values of the momentum. However, for $E_F = 9.6$ meV, only Δ_b contributes to optical transitions because E_F cuts E_{+-} curve only at one value of the momentum. In Fig. 4.8, we show possible allowed interband and intraband transitions

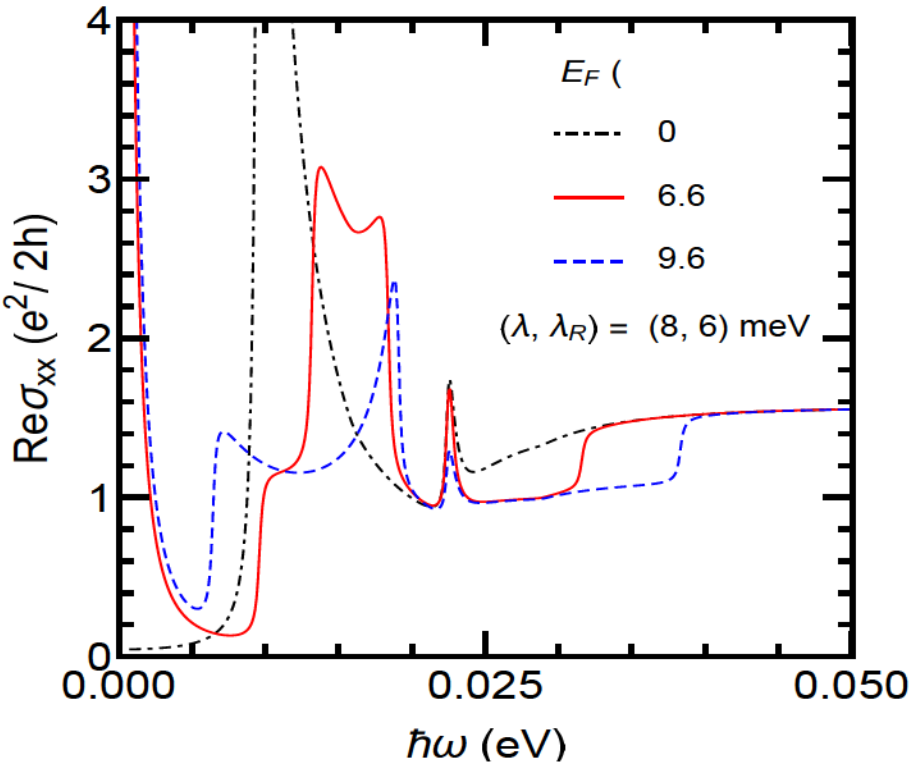

Figure 4.10: Same as in Fig. 4.9 but for $\lambda, \lambda_R \neq 0$.

by contrasting the case $\lambda \neq 0, \lambda_R = 0$ in the upper panels and the case $\lambda = 0, \lambda_R \neq 0$ in the lower panels. The blue arrows represent the interband transitions $E_{+-} \rightarrow E_{++}$ for $0 < E_F < \lambda$ and $0 < E_F < \lambda_R$ as can be seen in Fig. 4.8 (b) and (d). The black arrows represent the allowed interband transitions $E_{-+} \rightarrow E_{+-}(E_{++})$ and $E_{--} \rightarrow E_{+-}(E_{++})$ for $E_F = 0$ and $E_F \neq 0$, repectively, while the red arrows indicate intraband transitions that occur near E_F.

Now we present results for the real part of Eqs. (47) and (48) ($\mathrm{Re}\sigma_{xx} = \mathrm{Re}\sigma^{d}_{xx} + \mathrm{Re}\sigma^{nd}_{xx}$), evaluated numerically, versus $\hbar\omega$ using a Lorentzian form of Dirac delta function and taking $\Gamma = 0.2$ meV for $T \neq 0$. We start from the upper panel of Fig. 4.9 by considering the case $\lambda \neq 0$ and $\lambda_R = 0$. The transitions are vertical for photon's momentum $q \sim 0$ and connect the filled valence band to empty conduction band, see Fig. 4.8 (a). For the case of $E_F = 0$, intraband response appears due to the transition $E_{+-} \rightarrow E_{+-}$ and has a δ function form, centred around $\hbar\omega = 0$, which broadens the peak when any kind of scattering is taken into account. Further, intraband responses occur when the Fermi level is located away from the Dirac point. For $\hbar\omega = 2\lambda$ we obtain another Dirac delta peak due to the transition from $E_{--} \rightarrow E_{+-}$, which is also broadened through

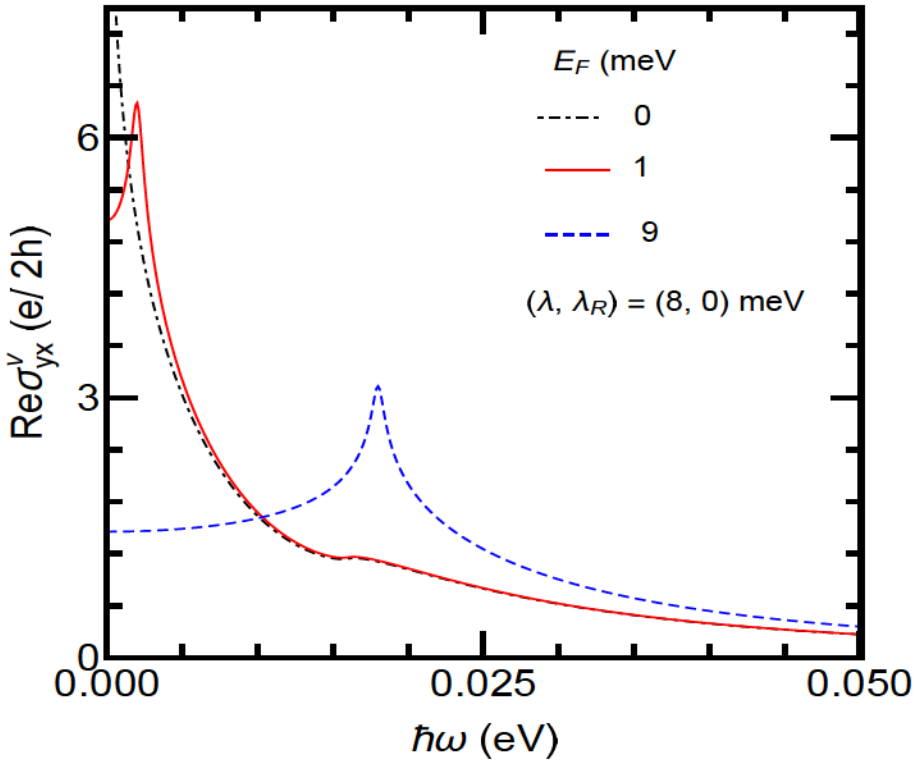

Figure 4.11: Valley-Hall conductivity versus photon energy for $\lambda_R = 0$ at $T = 0.5$ K.

$i\pi\delta(x) = \lim_{\Gamma\to 0}(1/x - i\Gamma)$, cf. Eq. (47). For $0 < E_F < \lambda$, the new absorption peaks appear at $\hbar\omega = 2E_F$ and $\hbar\omega = 2(E_F + \lambda)$ due to the possible transitions $E_{--} \to E_{+-}$ and $E_{-+} \to E_{+-}$. For $E_F > \lambda$, the absorption peaks disappear below $\hbar\omega < 2\lambda$ because the transition $E_{--} \to E_{+-}$ is no longer possible due to the filling of states below the Fermi level that are Pauli blocked. Further, the Drude peak persists at low $\hbar\omega$, but now two other pieces of interband transitions emerge with onsets at $\Delta_a + E_F$ and $\Delta_b + E_F$.

In the lower panel of Fig. 4.9 we show the results for real part of the longitudinal conductivity for $\lambda = 0$, $\lambda_R \neq 0$ for different values of E_F. For $E_F = 0$, we can see that there is a peak at $2\lambda_R$ which is the separation between E_{--} and E_{+-} bands. In addition, there is a kink at $4\lambda_R$ due to the transition $E_{-+} \to E_{++}$. As we increase the Fermi level, say, $0 < E_F < \lambda_R$ and $E_F > \lambda_R$, the peak becomes sharper and we see a onset of a Drude contribution at low $\hbar\omega$ due to intraband transitions $E_{+-} \to E_{+-}$ and $E_{++} \to E_{++}$ in contrast to $E_F = 0$ case (black dot-dashed curve). Further, for finite values of E_F, we see the steps at $2E_F$ similar to monolayer graphene ($\lambda = \lambda_R = 0$) as well as features at $\Delta_a + E_F$, $\Delta_b - E_F$, and $\Delta_b + E_F$ above which we attain the flat absorption like

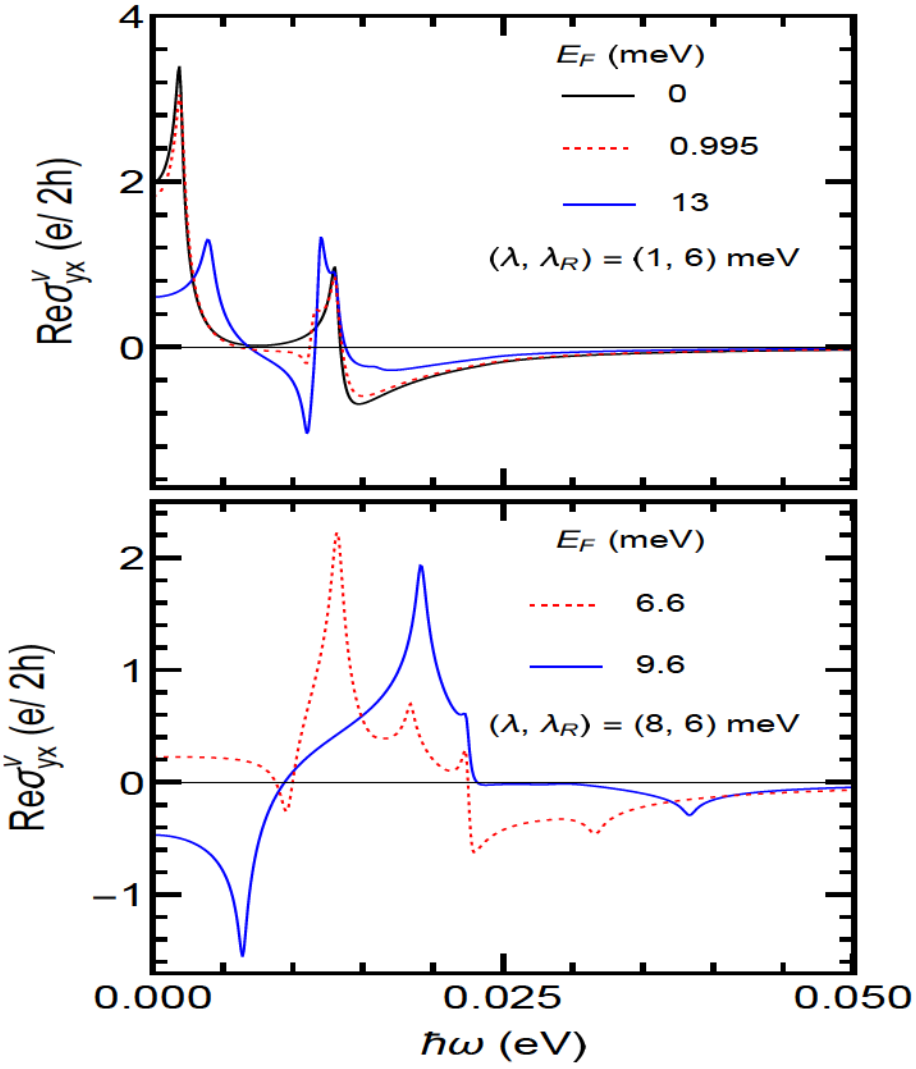

Figure 4.12: Same as in Fig. 4.11 but with the upper panel for $\lambda_R > \lambda$ and the lower one for $\lambda_R < \lambda$.

pristine graphene [214]. Note that our results are similar to bilayer graphene [216, 217]. But here, the Rashba SOC, which allows the interband transitions between opposite spin bands, gives rise to the absorption peaks, while these peaks in bilayer graphene are due to interlayer hopping between two graphene sheets.

The real part of the longitudinal conductivity as a function of the photon energy, for $\lambda, \lambda_R \neq 0$, is show in Fig. 4.10 for several values of E_F: (i) just below the maximum of the Mexican hat i.e. $\lambda\lambda_R/(\lambda^2 + \lambda_R^2)^{1/2} < E_F < \lambda$ (ii) just above the Mexican hat, i.e., for $\lambda < E_F < (\lambda^2 + 2\lambda_R^2)^{1/2}$. For $E_F = 0$ we find a large absorption peak at approximately $2\lambda_R$, which corresponds to transitions

between the two square-root singularities of the DOS, see Fig. 4.4, or transitions between the two minima of the Mexican hat structures of the E_{--} and E_{-+} bands. As E_F moves into the Mexican hat, this feature disappears because states below E_F are occupied and, therefore, Pauli blocked. Further, the major peaks are due to the transitions $E_{+-} \rightarrow E_{++}$, $E_{--} \rightarrow E_{-+}$, $E_{--} \rightarrow E_{++}$ and $E_{-+} \rightarrow E_{++}$, respectively. The gap energies which contribute to the onset of these transition peaks are indicated in Fig. 4.7 and given analytically in table 4.1. Also, the conductivity retains the flat absorption at sufficiently higher values of $\hbar\omega$ similar to pristine graphene [214].

Plots of the real part of σ^v_{yx} for $E_F = 0$ (black dotdashed curve) and $E_F \neq 0$ (red and blue dashed curves) in the absence of Rashba SOC ($\lambda_R = 0$) are shown in Fig. 4.11. In the dc limit, the expected value of the valley-Hall conductivity is obtained as can be seen in Fig. 4.5 (black curve). If the system is illuminated by photons of frequency ω, the amplitude of the absorption peaks is suppressed for $E_F = 0$, while an increase in it is observed for $E_F \neq 0$. For $\hbar\omega = 2|\lambda|$ a strong valley-Hall response is observed for $E_F \neq 0$. Therefore, it can be expected that a stronger valley-Hall response may be accessible when the photon energy is tuned to the valley-Zeeman SOC. For $\hbar\omega > 2|\lambda|$, σ^v_{yx} decreases rapidly and approaches zero at sufficiently higher values of $\hbar\omega$.

The real part of the valley-Hall conductivity is shown in Fig. 4.12 for several values of E_F. In the dc limit ($\omega = 0$), we obtain the quantized value of the valley-Hall conductivity (Re$\sigma^v_{yx} = e/h$) for $E_F = 0$ (black curve in the upper panel). If the system is subjected to photon of frequency ω, an increase in the magnitude of the valley-Hall response is observed. The absorption peaks occur at the same onset energies as indicated in Fig. 4.7. For example, the first peak appeared when $\hbar\omega = 2\Delta_1$ or transition between the minima of the E_{--} and E_{+-} bands. Further, the change in sign of the conductivity is due to the Rashba SOC, which is responsible for the coupling between spin-up and spin-down bands e.g., the transition from the maximum of Mexican hat of E_{--} band to the minimum of E_{++} band around $k = 0$. Furthermore, for finite values of E_F we obtain new features in the optical spectrum due to the emergence of new transitions such as $E_{+-} \rightarrow E_{++}$, e.g., some features are completely removed due to Pauli blocking. Also, the valley-Hall response is diminished at sufficiently high frequencies. However, in the case of $\lambda_R < \lambda$ (lower panel), the difference among the optical transition energies is significantly enhanced due to larger values of λ and new features emerge at the momenta at which E_F crosses the E_{+-} band (see Fig. 4.7).

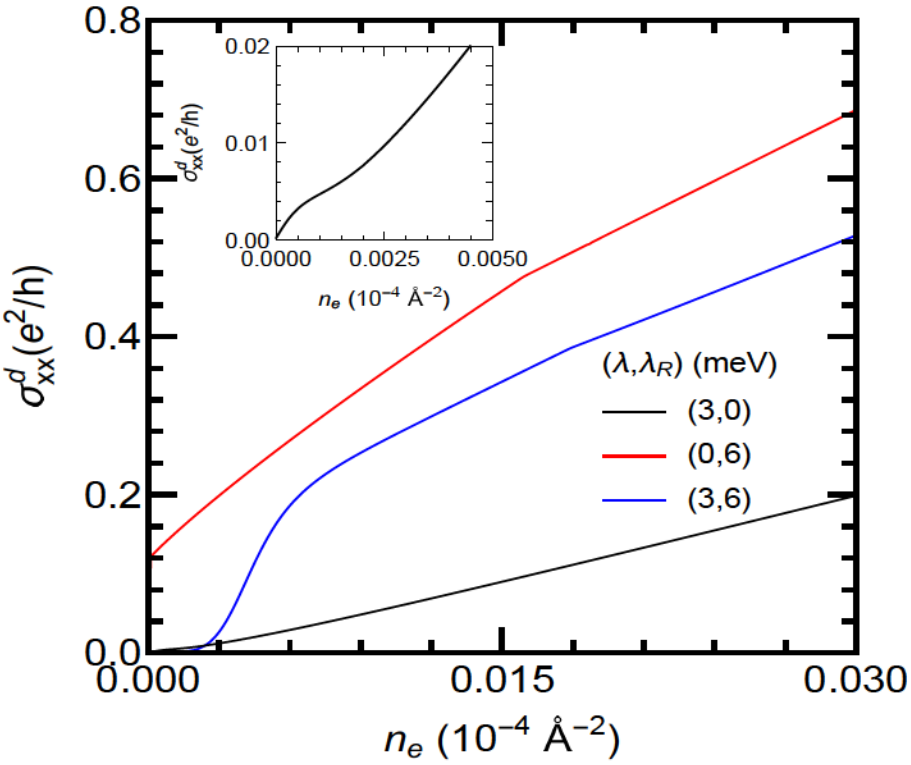

Figure 4.13: Longitudinal conductivity σ^d_{xx} in units of e^2/h versus electron concentration n_e for different values of λ and λ_R. For further clarity, the range $0-5$ meV is shown in inset.

Moreover, some of the optical transitions are no longer possible, e.g., $E_{--} \rightarrow E_{+-}$ when E_F is just above the Mexican hat because the states below it are occupied and, therefore, Pauli blocked (blue curve).

In Fig. 4.13 we plot σ^d_{xx}, from Eq. (48), by evaluating it numerically versus electron concentration (n_e) and using the expression of τ given in Appendix B but evaluated at the Fermi level, $k = k_F$. The conductivity increases with E_F and therefore with the carrier density n_e. The diffusive conductivity increases linearly with n_e but cusp-like features appear when E_{++} band begin to occupied at specific values of n_e in contrast to pristine graphene [218, 219]. This behaviour makes graphene/WS_2 a suitable candidate for charge switches contrary to pristine graphene. The screening effect becomes significantly weaker when only the λ term is present. Moreover, the conductivity shown in Fig. 4.14 increases in the low-density regime for $\lambda = 0$ and $\lambda_R \neq 0$ as compared to the $\lambda \neq 0$, $\lambda_R = 0$ and $\lambda, \lambda_R \neq 0$ case. In the limit $\lambda = \lambda_R = 0$ we obtain the result similar to pristine graphene [218, 219].

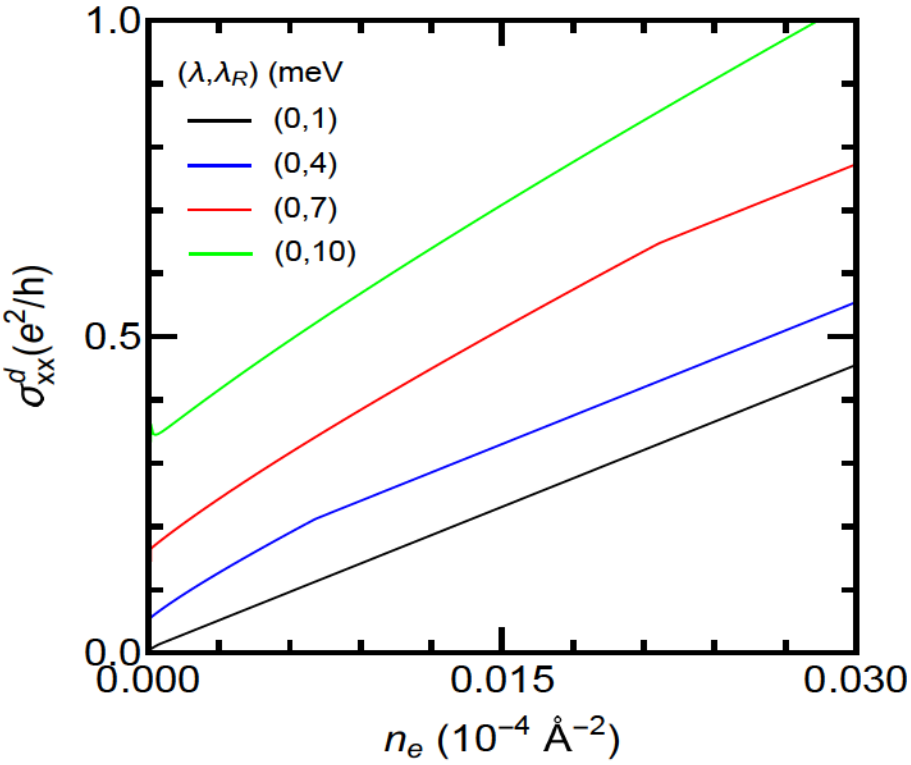

Figure 4.14: Same as in Fig. 4.13 but for different values of λ_R.

4.5 Summary and conclusion

We studied the energy dispersion of graphene/WSe_2 heterostructures by using a TB model in the presence of valley-Zeeman and Rashba SOCs. We found that the effective Hamiltonian (29) derived from the TB one (30) nicely captures the low-energy physics near the K and K' valleys. We demonstrated that the density of states has a finite value around $E = 0$ in both cases $\lambda \neq 0, \lambda_R = 0$ and $\lambda = 0, \lambda_R \neq 0$. In addition, it has a square root singularity when both λ and λ_R are present. This singularity is similar to that in biased bilayer graphene; however, here it is due to the Rashba SOC whereas in biased bilayer graphene it is due to interlayer hopping. We also found that the ac and dc valley-Hall conductivities change sign in the presence of the λ_R term, which leads to interband transitions. Also, the band gap is enhanced by increasing the strength λ_R. Further, for $\lambda_R >> \lambda$ the valley-Hall conductivity exhibits a behaviour similar to that in gapped graphene and topological insulators [130, 215]. The screening effect in the diffusive conductivity is dominant only when the Rashba SOC is present, whereas it is significantly suppressed for $\lambda \neq 0, \lambda_R = 0$.

Also, the conductivity increases with λ_R in the low- and high-density regimes, see Fig. 4.14.

The dc valley-Hall conductivity changes sign when E_F is comparable to λ_R and vanishes at higher values of E_F, cf. Fig. 4.5. It also exhibits a strong temperature dependence when the Fermi level in the gap, cf. Fig. 4.6.

The intraband response of the ac longitudinal conductivity for $\lambda_R = 0$ (see upper panel of Fig. 4.9) shifts towards lower photon energies when E_F increases compared to $\lambda_R \neq 0$ (see lower panel of Fig. 4.9 and Fig. 4.10). We also noted the switching on and off of the Drude response when the Fermi energy is varied (see Fig. 4.10), which may be of interest in technological applications. In addition, for $\lambda, \lambda_R \neq 0$ new onsets in the optical conductivity appear due to the shifting of the Fermi level through the Mexican hat structure (see Figs. 4.10 and 4.12), which may be a promising feature in optical experiments. Our findings may be pertinent to developing future spintronics and valleytronics devices such as field-effect tunnelling transistors, memory devices, phototransistors, etc.

4.6 Acknowledgments

M. Z. and P. V. acknowledge the support of the Concordia University Grant No. VB0038 and a Concordia University Graduate Fellowship. The work of M. T. was supported by Colorado State University.

Chapter 5

Valley-controlled transport in graphene/ WSe_2 heterostructures under an off-resonant polarized light

5.1 Abstract

We investigate the electronic dispersion and transport properties of graphene/WSe_2 heterostructures in the presence of a proximity-induced spin-orbit coupling λ_v, sublattice potential Δ, and an off-resonant circularly polarized light of frequency Ω and effective energy Δ_Ω. Using a low-energy Hamiltonian we find that the interplay between different perturbation terms leads to inverted spin-orbit coupled bands. At high Ω we study the band structure and dc transport using the Floquet theory and linear response formalism, respectively. We find that the inverted band structure transfers into the direct band one when the off-resonant light is present. The valley-Hall conductivity behaves as an even function of the Fermi energy in the presence and absence of this light. At $\Delta_\Omega = \lambda_v - \Delta$ a transition occurs from the valley-Hall phase to the anomalous Hall phase. In addition, the valley-Hall conductivity switches sign when the polarization of the off-resonant light changes. The valley polarization vanishes for $\Delta_\Omega = 0$ but it is finite for $\Delta_\Omega \neq 0$ and reflects the lifting of the valley degeneracy of the energy levels, for $\Delta_\Omega = 0$, when the off-resonant light is present. The

corresponding spin polarization, present for $\Delta_\Omega = 0$, increases for $\Delta_\Omega \neq 0$. Further, pure K or K' valley polarization is generated when Δ_Ω changes sign. Also, the charge Hall conductivity is finite for $\Delta_\Omega \neq 0$ and changes sign when the handedness of the light polarization changes.

5.2 Introduction

Since its discovery graphene has attracted immense attention both theoretically and experimentally due to its peculiar electronic and optical properties [265]. But, it has limited usage in the field of spintronics due to its very weak intrinsic spin orbit coupling (SOC). The intrinsic SOC in graphene is theoretically predicted to be weak, 12 μeV [202]. A value of 20 μeV is reported in a recent experiment for graphene on SiO_2 substrate [221]. A lot of efforts have been made to enhance the strength of SOC in graphene by employing external means, such as graphene hydrogenation [179, 278] or fluorination [181] as well as heavy adatom decoration [182, 183], and bringing it to proximity with other two-dimensional materials specifically transition metal dichalcogenides (TMDCs) [184, 185, 186]. In recent years the heterostructures of graphene and TMDCs have become more promising because the Dirac cone of graphene is well fit in the band gap of TMDCs, which leaves it intact. The giant native SOC of TMDCs is transferred to graphene via hybridization processes. Moreover, the combinations of graphene with TMDCs, such as MoS_2 or WSe_2, exhibit the proximity SOC on the meV scale [210, 212, 222, 201, 223, 224, 225, 226]

Presently SOC, induced by proximity effects, is no longer limited to theoretical studies, as it has been demonstrated by experimentally as well [227]. The breaking of spatial symmetry due to the substrate leads to an alteration of the Hamiltonian and spin degeneracy of graphene and opens a gap in its massless energy dispersion. In addition, it has been verified by experiments [190, 226, 228, 189] that another type of sublattice-resolved intrinsic SOC arises, the so-called valley-Zeeman or staggered SOC with opposite sign on the A and B sublattices. Further, enhancement of the Rashba SOC and creation of staggered potentials are also unavoidable [229].

Nowadays, the optical control of functional materials has been become a hot topic in the condensed matter physics. In addition, it creates a bridge between condensed matter physics [230] and ultrafast spectroscopy [231]. Many intriguing phenomena have been realized in optically

driven quantum solids such as light induced superconductivity [232, 233], photo-initiated insulator-metal transition [234, 235], microscopic interactions, such as the electron-phonon one, controlled by light [236, 237, 238], and theoretically predicted Floquet topological phases of matters [239, 240, 241, 242, 243]. These Floquet phases have stimulated much interest but direct evidence for electron-photon Floquet dressed states is scarce to date [244, 245] contrary to the field of artificial lattices [246, 247, 248, 249, 250, 251].

Recently, light-induced anomalous Hall effect has been observed experimentally in monolayer graphene by using an ultrafast transport technique [252] and predicted theoretically using a quantum Liouville equation with relaxation [253]. Also, graphene under the influence of light has been studied in various frameworks [239, 240, 241, 242, 254, 255, 256, 257, 258] The transport properties, especially valley-dependent dc transport, using the Floquet theory, have not been addressed sufficiently in contrast with a large amount of research on proximitized graphene. As far as transport in the presence of an off-resonant light is concerned, we are aware only of an electron transport study in MoS_2 [231], of another one on graphene and the Lieb lattice [259], and of a thermal transport study in topological insulators in the absence of any SOC [260]. Here we investigate theoretically the band structure in laser-driven graphene/WSe_2 heterostructures using the Floquet theory in the high-frequency regime. Also, we study dc transport in such heterostructres in the framework of linear response theory. We show that the interplay between the proximity SOCs and off-resonant light leads to a phase transition from the inverted band regime to the direct one. Our results are in good agreement with experimental results [252] in the limit of vanishing proximity SOCs.

In Sec. 5.3 we specify the Hamiltonian and obtain the eigenvalues and eigenfunctions of the proximity modified graphene as well as an analytical expression for the density of states (DOS). In Sec. 5.4 we derive analytical expressions for the conductivities and provide numerical results. Conclusions and a summary follow in Sec. 5.5.

5.3 Formulation

The real space tight-binding (TB) Hamiltonian of proximitized graphene is written as [229, 209, 271]

$$\begin{aligned} H &= -t\sum_{\langle i,j\rangle,\alpha} c^{\dagger}_{i\alpha}c_{j\alpha} + \Delta\sum_{i\alpha}\eta_{c_i}c^{\dagger}_{i\alpha}c_{i\alpha} + \frac{i}{3\sqrt{3}}\sum_{\langle\langle i,j\rangle\rangle,\alpha\alpha'}\lambda^{i}_{I}\nu_{ij}c^{\dagger}_{i\alpha}c_{j\alpha'}[s_z]_{\alpha\alpha'} \\ &\quad + \frac{2i\lambda_R}{3}\sum_{\langle i,j\rangle,\alpha\alpha'} c^{\dagger}_{i\alpha}c_{j\alpha'}[(\boldsymbol{s}\times\hat{\mathbf{d}}_{ij})_z]_{\alpha\alpha'}. \end{aligned} \tag{49}$$

Here $c^{\dagger}_{i\alpha}$ creates an electron with spin polarization α at site i that belongs to sublattice A or B, and $\langle i,j\rangle$ ($\langle\langle i,j\rangle\rangle$) runs over the nearest (second nearest) neighbouring sites. The second term is a staggered on-site potential, which takes into account the effective energy difference experienced by atoms at the lattice sites A ($\eta_{c_i}=+1$) and B ($\eta_{c_i}=-1$), respectively. The third and fourth terms represent the proximity-induced enhancement of the spin orbit coupling (SOC) due to a weak hybridization with the heavy atoms in transition metal dichalcogenides (TMDCs). The third term is the sublattice resolved intrinsic SOC (λ^{i}_{I} with $i=A,B$) where $\nu_{ij}=+1$, if the second nearest hopping is anticlockwise, and $\nu_{ij}=-1$ if it is clockwise with respect to the positive z axis. The last term is the Rashba SOC parametrized by λ_R. It arises because the inversion symmetry is broken when the graphene sheet is placed on top of TMDCs. Also, $\hat{\mathbf{d}}_{ij}=\mathbf{d}_{ij}/|\mathbf{d}_{ij}|$, $\boldsymbol{s}=(s_x,s_y,s_z)$ is the Pauli spin matrix, and $\mathbf{d}_{ij}$ the vector connecting the sites i and j in the same sublattice.

We analyze the physics of electrons near the Fermi energy using a low-energy effective Hamiltonian derived from Eq. (83) and a Dirac theory around K and K' points. It reads [188, 206, 204]

$$H_{s\eta} = v_F(\eta\sigma_x p_x + \sigma_y p_y) + \Delta\sigma_z + \lambda_R(\eta s_y\sigma_x - s_x\sigma_y) + \frac{1}{2}[\lambda^{A}_{I}(\sigma_z+\sigma_0) + \lambda^{B}_{I}(\sigma_z-\sigma_0)]\eta s. \tag{50}$$

Here $\eta=\pm1$ denotes the valleys K and K', $s=+1(-1)$ is for spin up (down), Δ is the mass term that breaks the inversion symmetry, λ_R the Rashba type SOC strength, (σ_x, σ_y, and σ_z) the Pauli matrix that corresponds to the pseudospin (i.e., $A-B$ sublattice); σ_0 is the unit matrix in the sublattice space and v_F (8.2×10^5 m/s) denotes the Fermi velocity of Dirac fermions. The last term arises due to the breaking of sublattice symmetry and can be categorized into two groups

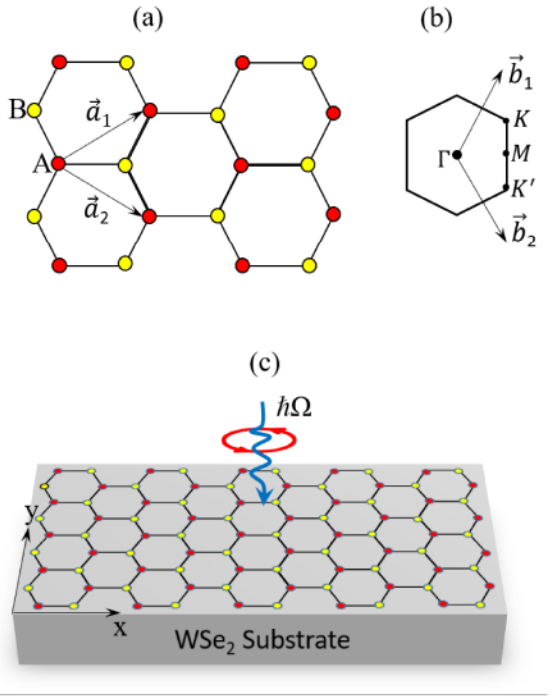

Figure 5.1: (a) Real-space graphene with $\vec{a}_1$ and $\vec{a}_2$ the primitive lattice vectors. (b) Graphene's first Brillouin zone and high symmetry points Γ, K, K', and M in reciprocal space. Its primitive lattice vectors are $\vec{b}_1$ and $\vec{b}_2$. (c) Schematics of graphene epitaxially grown on a WSe_2 substrate and irradiated by a left circularly polarized light.

according to its dependence on sublattice spin: (i) $\lambda_{so}\sigma_z\eta s$ when $\lambda_{so} = (\lambda_I^A + \lambda_I^B)/2$. This is called conventional Kane-Mele (KM) type SOC, which has a magnitude of the order of μeV in graphene/TMDCs heterostuctures [229, 204, 202]; (ii) $\lambda_v\sigma_0\eta s$ when $\lambda_v = (\lambda_I^A - \lambda_I^B)/2$. It is called valley-Zeeman or staggered SOC and has been experimentally confirmed in graphene on TMDCs [190, 226, 228, 189]; it occurs only for $\lambda_I^A = -\lambda_I^B$. Further, Refs. [202], [229], and [204] show that λ_{so} is negligibly small or zero. In view of that, we treat only the regime $\lambda_v >> \lambda_{so}$ and neglect λ_{so} altogether.

As shown in Fig. 5.1, monolayer graphene, irradiated by off-resonant circularly polarized light, is grown on WSe_2 that provides a staggered potential and induces SOC in graphene. We study the changes induced by circularly polarized light in graphene/WSe_2 in the presence of a perpendicular electric field E. We describe the monochromatic light through a time-dependent vector potential $\vec{A}(t) = (E_0/\Omega)(\cos\Omega t, p\sin\Omega t)$ with Ω its frequency, E_0 the amplitude of the field E, and $p = +1(-1)$ for left (right) circular polarization. The vector potential is periodic in time $A(t+T) =$

$A(t)$ with $T = 2\pi/\Omega$. Eq. (88) in the presence of circularly polarized light reads

$$H_{s\eta}(t) \;=\; H^0_{s\eta} + V(t), \tag{51}$$

with

$$\begin{aligned} H^0_{s\eta} &= v_F(\eta\sigma_x p_x + \sigma_y p_y) + \Delta\sigma_z + \lambda_v\sigma_0\eta s + \lambda_R(\eta s_y\sigma_x - s_x\sigma_y) \\ V(t) &= -(ev_F/\hbar)[\eta\sigma_x A_x(t) + \sigma_y A_y(t)]. \end{aligned} \tag{52}$$

For $\hbar\Omega \gg t$, where t is the hopping parameter, Eq. (51) can be reduced to an effective static, time-independent Hamiltonian $H^{\rm eff}_{s\eta}(t)$ using Floquet theory [240]. $H^{\rm eff}_{s\eta}(t)$ is defined through the time evolution operator over one period

$$\hat{U} = \hat{T}\exp[-i\int_0^T H_{s\eta}(t)dt] = \exp[-iH^{\rm eff}_{s\eta}T], \tag{53}$$

where $\hat{T}$ is time ordering operator. Using perturbation theory and expanding $\hat{U}$ in the limit of large frequency Ω, we obtain

$$H^{\rm eff}_{s\eta} = H^0_{s\eta} + \frac{[V_{-1} - V_1]}{\hbar\Omega} + O(\Omega^{-2}), \tag{54}$$

where $V_m = (1/T)\int_0^T e^{-im\Omega t}V(t)dt$ is the m-th Fourier harmonic of the time-periodic Hamiltonian. Corrections to Eq. (54), to all orders of $1/\Omega$, can be obtained by the method of Ref. [259]. Here we neglect them because we treat only the case $\hbar\Omega \gg t$. Using Eqs. (51) and (54) we obtain

$$H^{\rm eff}_{s\eta} \;=\; v_F[\eta\sigma_x p_x + \sigma_y p_y] + (\Delta + p\eta\Delta_\Omega)\sigma_z + \lambda_v\sigma_0\eta s + \lambda_R(\eta s_y\sigma_x - s_x\sigma_y), \tag{55}$$

where $\Delta_\Omega = v_F^2 e^2 E_0^2/\hbar\Omega^3$ is the energy term due to the circularly polarized light, which essentially renormalizes the mass of the Dirac Fermions [240].

The diagonalization of Eq. (55) gives the dispersion

$$E^{\eta p}_\xi(k) \;=\; l\{G_\eta + 2\lambda_R^2 + \epsilon_k^2 + 2s\sqrt{\Upsilon}\}^{1/2}. \tag{56}$$

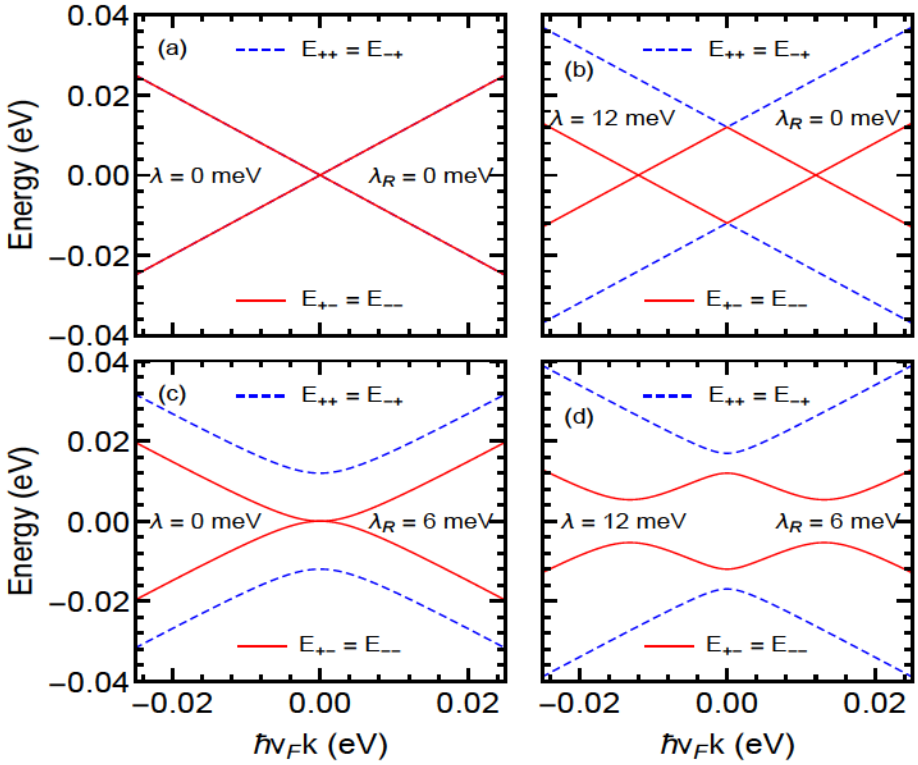

Figure 5.2: Energy dispersion curves around K and K' of a graphene/WSe_2 heterostructure for $\Delta = 1$ meV, $\lambda_v = 4$ meV, and $\lambda_R = 2$ meV. The left panel shows the inverted band regime, with strong spin mixing of different states with black/red shading, obtained when $\Delta_\Omega < \Delta + \lambda_v$. The right panel shows direct band regime with nearly full spin polarization and obtained when $\Delta_\Omega > \Delta + \lambda_v$. The marking of all curves resulting from Eq. (8), with $p = 1$ for all of them and not specified, is shown inside the panels.

where $\xi = \{l, s\}$ and $G_\eta = \lambda_v^2 + \bar{\Delta}_{\eta p}^2$, $\Upsilon = \epsilon_k^2 \bar{\lambda}^2 + (\lambda_R^2 - \lambda_v \bar{\Delta}_{\eta p})^2$ with $\epsilon_k = \hbar v_F k$, $\bar{\Delta}_{\eta p} = \Delta + \eta p \Delta_\Omega$ and $\bar{\lambda}^2 = \lambda_R^2 + \lambda_v^2$. Further, $l = +1(-1)$ denotes the conduction (valence) band and $s = +1(-1)$ represents the spin-up (spin-down) branches. The normalized eigenfunctions for both valleys are

$$\psi_\xi^{+p}(k) = \frac{N_\xi^{+p}}{\sqrt{S_0}} \begin{pmatrix} 1 \\ A_\xi^{\eta p} e^{i\phi} \\ -iB_\xi^{\eta p} e^{i\phi} \\ -iC_\xi^{\eta p} e^{2i\phi} \end{pmatrix} e^{i\mathbf{k}\cdot\mathbf{r}}, \qquad \psi_\xi^{-p}(k) = \frac{N_\xi^{-p}}{\sqrt{S_0}} \begin{pmatrix} -A_\xi^{\eta p} e^{i\phi} \\ 1 \\ iC_\xi^{\eta p} e^{2i\phi} \\ -iB_\xi^{\eta p} e^{i\phi} \end{pmatrix} e^{i\mathbf{k}\cdot\mathbf{r}}, \tag{57}$$

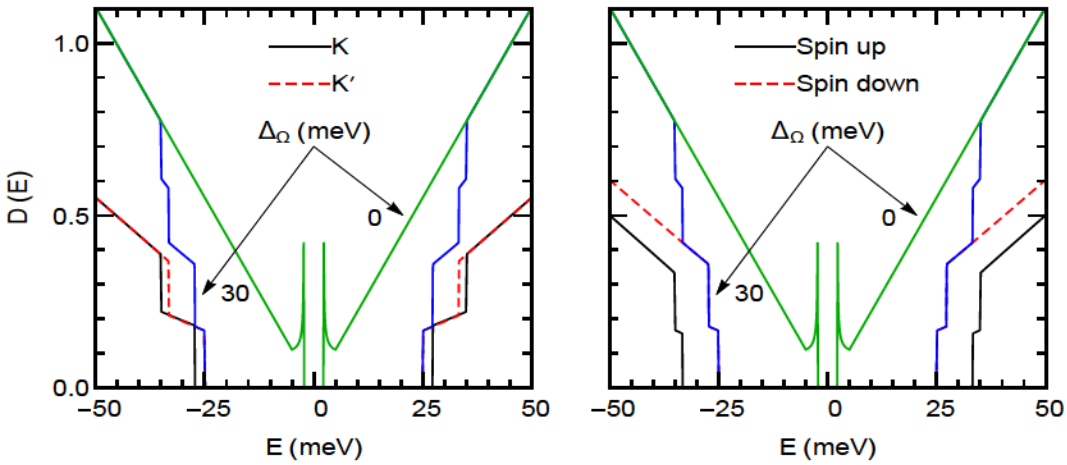

Figure 5.3: Density of states for two values of Δ_Ω, as indicated, and $\Gamma = 0.01$ meV. The left panel shows the valley components of the DOS, with both spins included, whereas the right panel shows the spin components of the DOS, with both valleys included. In both panels the curves indicated by arrows show the total DOS. The parameters Δ, λ_v, and λ_R are the same as in Fig. 5.2. The marking of the curves is shown inside the panels. In the left panel both spin contributions are included, in the right one both valley contributions are included.

respectively, with

$$N_\xi^{\eta p} = l\left[1 + (A_\xi^{\eta p})^2 + (B_\xi^{\eta p})^2 + (C_\xi^{\eta p})^2\right]^{-1/2}, \tag{58}$$

$S_0 = L_x L_y$ the area of the sample, and $\phi = \tan^{-1}(k_y/k_x)$. Further, $A_\xi^{\eta p} = \{E_\xi^{\eta p} - \eta\alpha_1^\eta\}/\epsilon_k$, $B_\xi^{\eta p} = 2\lambda_R\{(E_\xi^{\eta p})^2 - (\alpha_1^\eta)^2\}/\epsilon_k\{(E_\xi^{\eta p} + \eta\alpha_1^\eta)(E_\xi^{\eta p} - \eta\alpha_2^\eta) - \epsilon_k^2\}$, and $C_\xi^{\eta p} = 2\lambda_R\{E_\xi^{\eta p} - \eta\alpha_1^\eta\}/\{(E_\xi^{\eta p} + \eta\alpha_1^\eta)(E_\xi^{\eta p} - \eta\alpha_2^\eta) - \epsilon_k^2\}$ with $\alpha_1^\eta = \bar{\Delta}_{\eta p} + \lambda_v$, and $\alpha_2^\eta = \bar{\Delta}_{\eta p} - \lambda_v$.

In numerical calculations throughout the manuscript, we use values of the parameters Δ, λ_v, and λ_R somewhat larger than those of [209] to have well-resolved spin and valley splittings since the overall physics of the system is not changed when we do so. As for the values of Δ_Ω, it is known that the off-resonant light does not directly excite the electrons; instead, it modifies the electron bands through virtual photon absorption processes. To study the topological transitions of bands, this light must satisfy the condition $\hbar\Omega \gg t_j$. Accordingly, we will use the values of Δ_Ω from Refs. [240, 252].

The typical band structure (56) for both valleys is illustrated in Fig. 5.2 for $p = +1$, $\Omega_\Omega < \Delta + \lambda_v$ (inverted band regime), and $\Delta_\Omega > \Delta + \lambda_v$ (direct band regime). The left panel shows the inverted

band regime. The inversion occurs due to the anticrossing of the bands with opposite spins and in the presence of the Rashba SOC. The right panel depicts the direct band regime with simple parabolic dispersion. It is found that the spin and valley degeneracies are completely lifted when $\Delta_\Omega > \Delta + \lambda_v$, whereas the valley degeneracy is restored in the opposite limit similar to silicene [261]. The valleys are interchanged if proximitized graphene is irradiated by a right circularly polarized light $p = -1$ (not shown here).

5.3.1 Limiting cases and density of states (DOS)

i) Setting $\Delta = 0$ in Eq. (56), we obtain

$$E_\xi^{\eta p}(k) = l\{\lambda_v^2 + \Delta_\Omega^2 + 2\lambda_R^2 + \epsilon_k^2 + 2s\sqrt{Y}\}^{1/2}, \tag{59}$$

with $Y = \epsilon_k^2\bar{\lambda}^2 + (\lambda_R^2 - \eta\lambda_v\Delta_\Omega)^2$.

ii) In the limit $\lambda_R = 0$, Eq. (56) reduces

$$E_\xi^{\eta p}(k) = l\left[\epsilon_k^2 + \bar{\Delta}_{\eta p}^2\right]^{1/2} + s\lambda_v. \tag{60}$$

The DOS per unit area corresponding to Eq. (56) is given by

$$D(E) = \frac{|E|v_F^{-2}}{2\pi\hbar^2}\sum_{\eta p}\left[\frac{\theta(|E| - |E_{1g}^{\eta p}|)}{1 - \bar{\lambda}/M^+} + \frac{\theta(|E| - |E_{2g}^{\eta p}|)}{1 + \bar{\lambda}/M^-}\right], \tag{61}$$

with

$$\begin{aligned} E_{1g}^{\eta p} &= \lambda_v + \bar{\Delta}_{\eta p}, \quad E_{2g}^{\eta p} = \left[(\lambda_v - \bar{\Delta}_{\eta p})^2 + 4\lambda_R^2\right]^{1/2} \\ M^\pm &= \left[(\lambda_R^2 - \lambda_v\bar{\Delta}_{\eta p})^2 + \hbar^2 v_F^2\bar{\lambda}^2\epsilon_\pm\right]^{1/2} \\ \hbar^2 v_F^2\epsilon_\pm &= E^2 + \lambda_v^2 - \bar{\Delta}_{\eta p}^2 \pm 2\left[\bar{\lambda}^2E^2 - \lambda_R^2(\lambda_v + \bar{\Delta}_{\eta p})^2\right]^{1/2}. \end{aligned} \tag{62}$$

In Fig. 5.3 we plot the DOS given by Eq. (61). The two jumps in the DOS indicate that two gaps open at each valley, displaying the clear signature of lifting the spin and valley degeneracies, when graphene on WSe_2 substrate is in the direct band regime. The spin and valley degeneracies are

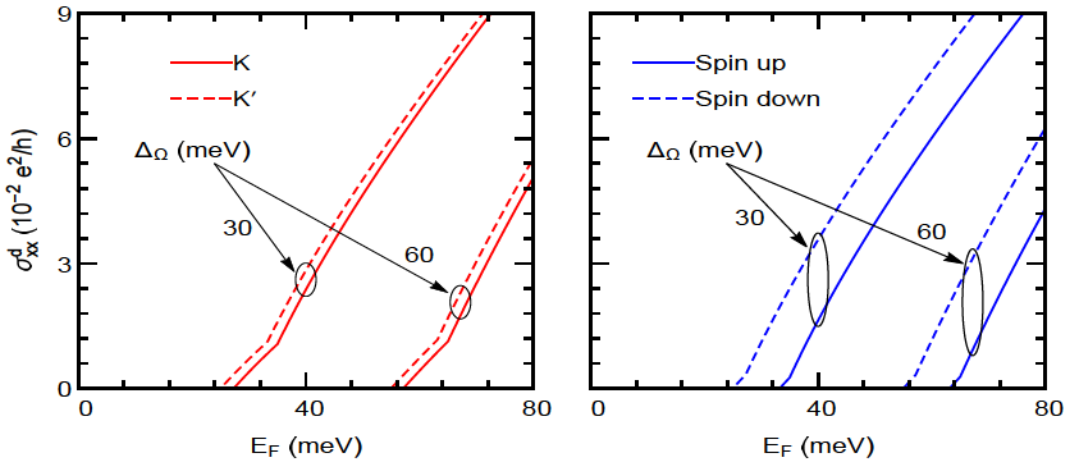

Figure 5.4: Longitudinal conductivity vs Fermi energy E_F for $T = 0$ K, and $\tau_F = 1 \times 10^{-15}$ s. The other parameters are the same as in Fig. 5.2.

completely lifted in the direct band regime while only the spin degeneracy is lifted in the inverted band regime. Note that the DOS diverges in the inverted band regime as $D(E) \propto (E - \Delta_1)^{-1/2}$ with $\Delta_1 = \lambda_R(\lambda_v + \Delta)/(\lambda_R^2 + \lambda_v^2)^{1/2}$ (see green curves in both panels). This divergence is due to the mexican-hat energy dispersion [217], cf. Fig. 5.2. In passing we may add that this behaviour of the DOS remains the same as the broadened one provided the level width Γ is small, $\Gamma < 0.5$ meV. For higher Γ the small structure of the DOS curves is smoothened out.

5.4 Conductivities

We consider a many-body system described by the Hamiltonian $H = H_0 + H_I - \mathbf{R} \cdot \mathbf{F}(t)$, where H_0 is the unperturbed part, H_I is a binary-type interaction (e.g., between electrons and impurities or phonons), and $-\mathbf{R} \cdot \mathbf{F}(t)$ is the interaction of the system with the external field F(t) [128]. For conductivity problems we have $\mathbf{F}(t) = e\mathbf{E}(t)$, where $\mathbf{E}(t)$ is the electric field, e the electron charge, $\mathbf{R} = \sum_i \mathbf{r}_i$, and $\mathbf{r}_i$ the position operator of electron i. In the representation in which H_0 is diagonal the many-body density operator $\rho = \rho^d + \rho^{nd}$ has a diagonal part ρ^d and a nondiagonal part ρ^{nd}. Correspondingly, for weak electric fields and weak scattering potentials, for which the first Born approximation applies, the conductivity tensor has a diagonal part $\sigma^d_{\mu\nu}$ and a nondiagonal part $\sigma^{nd}_{\mu\nu}$; the total conductivity is $\sigma^T_{\mu\nu} = \sigma^d_{\mu\nu} + \sigma^{nd}_{\mu\nu}, \mu, \nu = x, y$.

In general we have two kinds of currents, diffusive and hopping, with $\sigma^d_{\mu\nu} = \sigma^{dif}_{\mu\nu} + \sigma^{col}_{\mu\nu}$, but

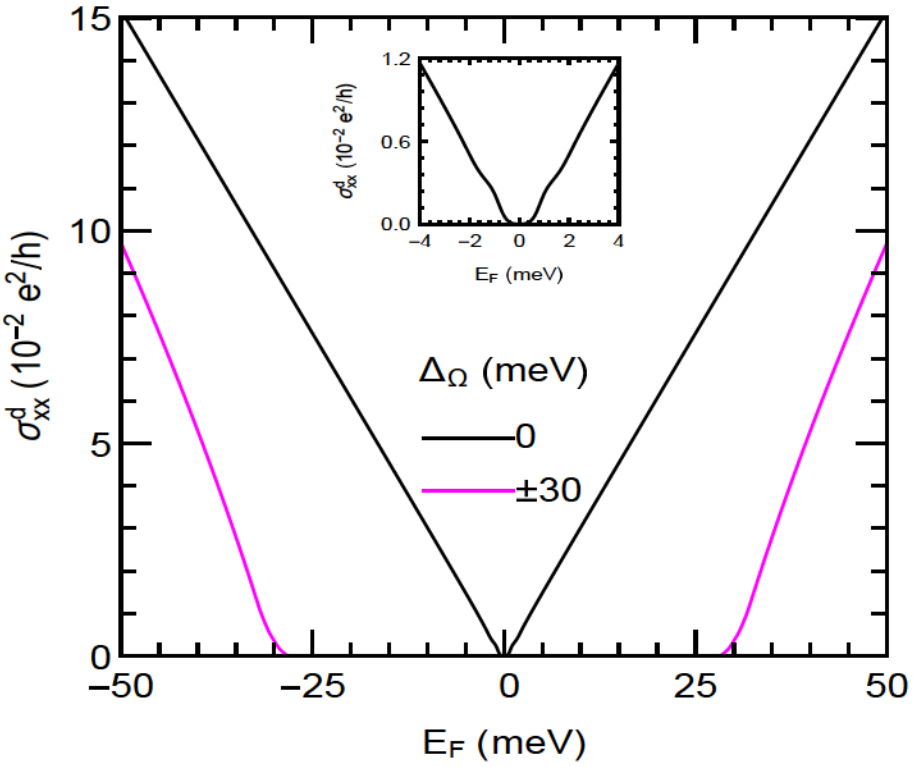

Figure 5.5: Total longitudinal conductivity vs Fermi energy E_F. The parameters are $\Delta = 0.54$ meV, $\lambda_R = 0.56$ meV, and $\lambda_v = 1.22$ meV [209].

usually only one of them is present. If no magnetic field is present, the hopping term $\sigma^{col}_{\mu\nu}$ vanishes identically and only the term $\sigma^{dif}_{\mu\nu}$ survives. For elastic scattering it is given by [128]

$$\sigma^{d}_{\mu\nu} = \frac{\beta e^2}{S_0} \sum_{\zeta} f_\zeta (1 - f_\zeta) v_{\nu\zeta}\, v_{\mu\zeta}\, \tau_\zeta, \tag{63}$$

with τ_ζ the momentum relaxation time, and $v_{\mu\zeta}$ the diagonal matrix elements of the velocity operator. Further, $f_\zeta = \left[1 + \exp[\beta(E_\zeta - E_F)]\right]^{-1}$ is the Fermi-Dirac distribution function, $\beta = 1/k_B T$, and T the temperature.

Regarding the contribution $\sigma^{nd}_{\mu\nu}$ one can use the identity $f_\zeta(1 - f_{\zeta'})\left[1 - \exp[\beta(E_\zeta - E_{\zeta'})]\right] = f_\zeta - f_{\zeta'}$ and cast the original form [128] in the more familiar one

$$\sigma^{nd}_{\mu\nu} = \frac{i\hbar e^2}{S_0} \sum_{\zeta \neq \zeta'} \frac{(f_\zeta - f_{\zeta'})\, v_{\nu\zeta\zeta'}\, v_{\mu\zeta\zeta'}}{(E_\zeta - E_{\zeta'})(E_\zeta - E_{\zeta'} - i\Gamma)}, \tag{64}$$

where the sum runs over all quantum numbers ζ and ζ' with $\zeta \neq \zeta'$. The infinitesimal quantity ϵ , in

the original form of the conductivity, has been replaced by Γ_ζ to phenomenologically account for the broadening of the energy levels. One should keep in mind that disorder leads to some modification of the Hall conductivity. However, this problem is not studied here. In Eq. (64) $v_{\nu\zeta\zeta'}$ and $v_{\mu\zeta\zeta'}$ are the off-diagonal matrix elements of the velocity operator. The relevant velocity operators are given by $v_x = \partial H/\hbar\partial k_x$ and $v_y = \partial H/\hbar\partial k_y$. With $\zeta = \{l, s, k, \eta, p\} = \{\xi, k, \eta, p\}$ for brevity, they read

$$\langle\zeta| v_x |\zeta'\rangle = v_F N_\xi^{\eta p} N_{\xi'}^{\eta p} (D_{\xi,\xi'}^{\eta p} e^{i\phi} + F_{\xi,\xi'}^{\eta p} e^{-i\phi}) \delta_{\eta,\eta'} \delta_{k,k'}, \tag{65}$$

$$\langle\zeta'| v_y |\zeta\rangle = i v_F N_\xi^{\eta p} N_{\xi'}^{\eta p} (D_{\xi,\xi'}^{\eta p} e^{-i\phi} - F_{\xi,\xi'}^{\eta p} e^{i\phi}) \delta_{\eta,\eta'} \delta_{k,k'}, \tag{66}$$

where $D_{\xi,\xi'}^{\eta p} = A_{\xi'}^{\eta p} + B_\xi^{\eta p} C_{\xi'}^{\eta p}$ and $F_{\xi,\xi'}^{\eta p} = A_\xi^{\eta p} + B_{\xi'}^{\eta p} C_\xi^{\eta p}$.

The diagonal velocity matrix elements $v_{x\zeta} = \partial E_\xi^{\eta p}/\hbar\partial k_x$ from Eq. (56) can be readily found

$$v_{x\zeta} = \frac{l\hbar v_F^2 k_x}{E_\xi^{\eta p}} \left[1 + \frac{s\bar{\lambda}^2}{\sqrt{\Upsilon}}\right]. \tag{67}$$

It's worth pointing out that our approach for evaluating the conductivity tensor is the same or similar with that followed in Refs. [231, 262] for MoS_2, [263, 162, 264] for silicene, and [153] for WSe_2. In all of them a perpendicular electric field, not the source-to-drain one, was included in H_0. This is similar to our inclusion of the off-resonant light term $V(t)$ and was also the case of Ref. [260].

We now calculate the conductivity σ_{yx}^{nd} given by Eq. (64). Further, the velocity matrix elements (80) and (81) are diagonal in k, therefore k will be suppressed in order to simplify the notation. The summation in Eq. (64) runs over all quantum numbers ξ, ξ', η, η', and k. The parameter $\Gamma_\zeta = \Gamma_{\eta\eta'}^{\xi\xi'}$, that takes into account the level broadening, is assumed independent of the band and valley indices, i.e., $\Gamma_{\eta\eta'}^{\xi\xi'} = \Gamma$. Using Eqs. (80) and (81) we can express Eq. (64) as

$$\begin{aligned} \mathrm{Re}\sigma_{yx}^{nd}(\xi,\xi',\eta,p) &= \frac{2e^2\hbar^2 v_F^2}{h} \int dk k \frac{(N_\xi^{\eta p} N_{\xi'}^{\eta p})^2 (f_{\xi k}^{\eta p} - f_{\xi' k}^{\eta p})}{(\Delta_{\xi\xi'}^{\eta p})^2 + \Gamma^2} \left[(D_{\xi,\xi'}^{\eta p})^2 - (F_{\xi,\xi'}^{\eta p})^2\right], \\ \mathrm{Im}\sigma_{yx}^{nd}(\xi,\xi',\eta,p) &= 0, \end{aligned} \tag{68}$$

where $\Delta_{\xi\xi'}^{\eta p} = E_{\xi k}^{\eta p} - E_{\xi' k}^{\eta p}$.

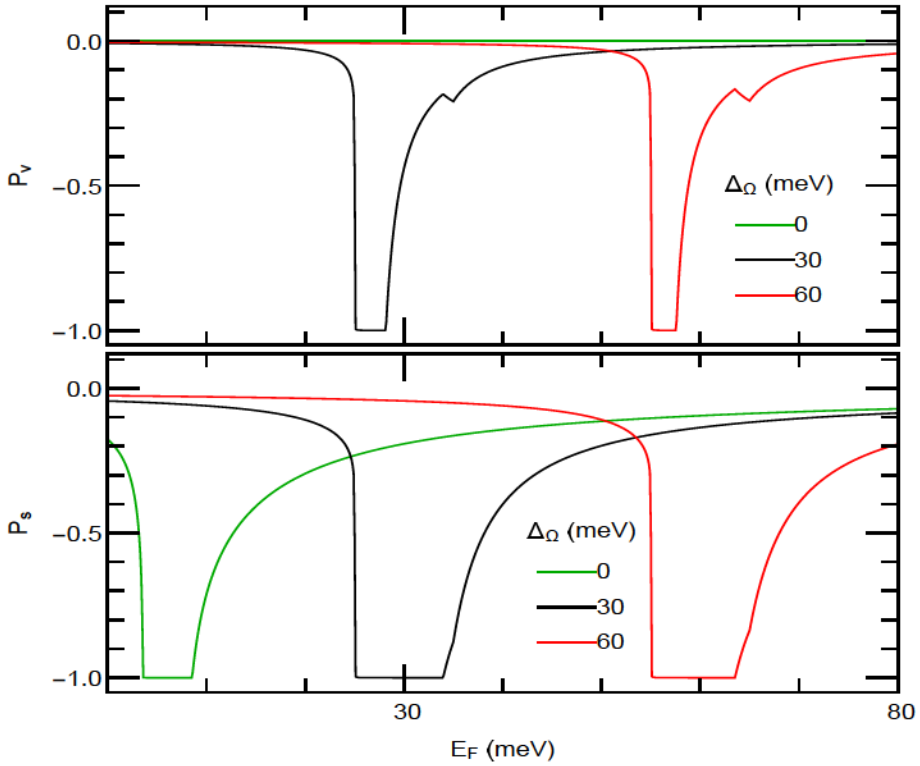

Figure 5.6: Valley P_v and spin P_s polarization vs E_F for different values of Δ_Ω, as indicated, and $\lambda_R = 4$ meV. The other parameters are the same as in Fig. 5.4. Notice that $P_v = 0$ for $\Delta_\Omega = 0$ while $P_s \neq 0$.

For $\lambda = \Delta = \Delta_\Omega = 0$ and $\lambda_R \neq 0$, Eq. (68) vanishes because the factor $(D^{\eta p}_{\xi,\xi'})^2 - (F^{\eta p}_{\xi,\xi'})^2$ becomes zero. Ignoring skew and intervalley scatterings, the valley-Hall conductivity (σ^v_{yx}) obtained from Eq. (68) can be evaluated as

$$\sigma^v_{yx} = \sum_{\xi\xi' p} \left[\sigma^{nd}_{yx}(\xi,\xi',+,p) - \sigma^{nd}_{yx}(\xi,\xi',-,p)\right], \tag{69}$$

where we set $\mathrm{Re}\sigma^{nd}_{yx}(\xi,\xi',\eta,p) \equiv \sigma^{nd}_{yx}(\xi,\xi',\eta,p)$. The spin-Hall conductivity σ^s_{yx} corresponding to Eq. (68) is finite only when both KM and staggered SOCs are present [203]. Therefore, σ^s_{yx} vanishes even in the presence of Rashba SOC. Even if it does not in graphene on WSe_2, it is assumed negligible in the regime $\lambda_v >> \lambda_{so}$ that we treat and we neglect it altogether, see also Sec. II, above Eq. (51). As usual, we have to multiply σ^v_{yx} by $1/2e$ [271].

We can find a simple analytical result from Eq. (86) for the specific case $\lambda_v, \lambda_R = 0$ in the low

temperature limit. It is

$$\sigma_{yx}^{v}=\begin{cases}\dfrac{e}{2h}, & -(\Delta+\eta p\Delta_{\Omega})<E_F<\Delta+\eta p\Delta_{\Omega}\\ \\ \dfrac{e}{2h}\dfrac{\eta\Delta+p\Delta_{\Omega}}{E_F}, & E_F>\Delta+\eta p\Delta_{\Omega}\end{cases} \tag{70}$$

Equations (16)-(17) of Ref. [231] in the limit $\lambda\to 0$ are similar to Eq. (70). For $\Delta_{\Omega}\to 0$, Eq. (70) reduces to a result reported in Ref. [130]. Further, we find the charge Hall conductivity

$$\sigma_{yx}^{c}=\sum_{p\eta\eta'\xi\xi'}\sigma_{yx}^{nd}(\xi,\xi',\eta,\eta',p)=\begin{cases}0, & \Delta_{\Omega}=0\\ \\ \neq 0, & \Delta_{\Omega}\neq 0\end{cases} \tag{71}$$

In the limit $\Delta_{\Omega}\to 0$, σ_{yx}^{c} vanishes.

We now consider the diagonal component σ_{xx}^{d} given by Eq. (63). Using Eq. (80), with $\xi=\xi'$, we obtain

$$\sigma_{xx}^{d}(\xi,\eta,p) \;=\; \frac{e^2v_F^2\beta}{\pi}\int dk\,k\,(N_{\xi}^{\eta p})^4 f_{\xi k}^{\eta p}(1-f_{\xi k}^{\eta p})(A_{\xi}^{\eta p}+B_{\xi}^{\eta p}C_{\xi}^{\eta p})^2\,\tau_{\xi k}^{\eta p}. \tag{72}$$

At very low temperatures we can make the approximation $\beta f_{\xi k}^{\eta p}(1-f_{\xi k}^{\eta p})\approx\delta(E_{\xi}^{\eta p}-E_F)$ and $\tau_{\xi k}^{\eta p}=\tau_{\xi k_F}^{\eta p}$. We find $r=\sigma_{xx}^{nd}(\xi,\eta,p)/\sigma_{xx}^{d}(\xi,\eta,p)<<1$, mainly because $\sigma_{xx}^{nd}(\xi,\eta,p)\propto\Gamma$. The precise value of r depends on the scattering strength through Γ and τ appearing in $\sigma_{xx}^{d}(\xi,\eta,p)$. In what follows we neglect $\sigma_{xx}^{nd}(\xi,\eta,p)$.

After evaluating the integral over k, Eq. (72) becomes

$$\begin{aligned}\sigma_{xx}^{d}(\xi,\eta,\quad p\quad) &= \frac{e^2\tau_F E_F}{\pi\hbar^2}\Big[(A_{\xi}^{\eta p}+B_{\xi}^{\eta p}C_{\xi}^{\eta p})^2(N_{\xi}^{\eta p})^4\frac{\theta(E_F-E_{1g}^{\eta p})}{1-\bar{\lambda}^2/M}\Big|_{\epsilon_{+F}}\\ &+\;(A_{\xi}^{\eta p}+B_{\xi}^{\eta p}C_{\xi}^{\eta p})^2(N_{\xi}^{\eta p})^4\,\frac{\theta(E_F-E_{2g}^{\eta p})}{1+\bar{\lambda}^2/M}\Big|_{\epsilon_{-F}}\Big],\end{aligned} \tag{73}$$

where $\tau_F\equiv\tau_{\xi k_F}^{\eta p}$ is the relaxation time evaluated at the Fermi level. As indicated, the 1st and 2nd

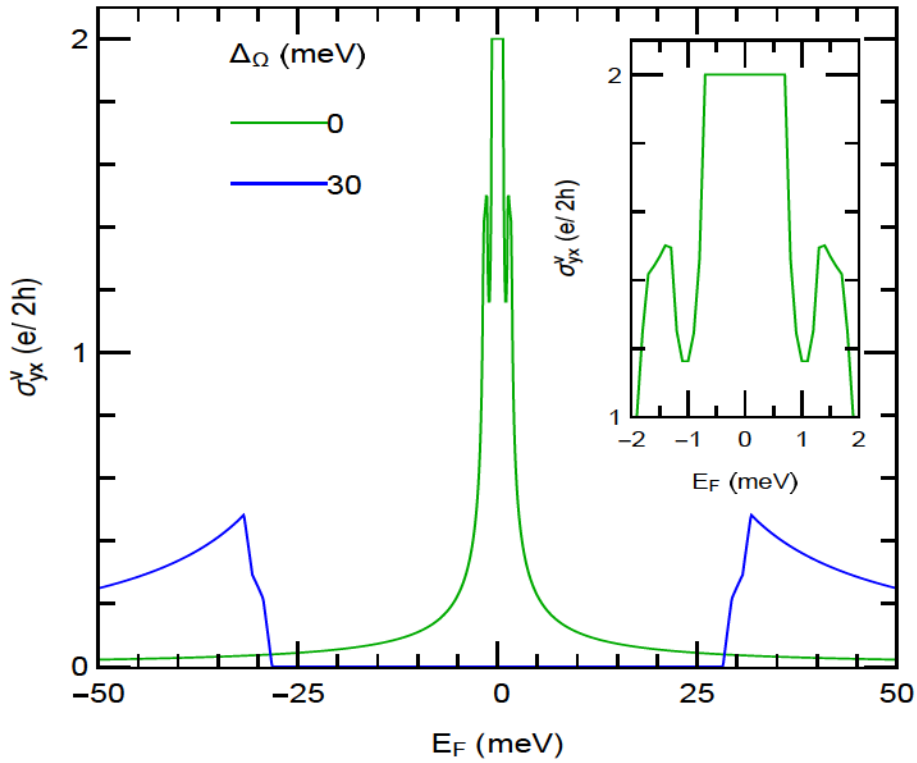

Figure 5.7: Valley-Hall conductivity vs. E_F for $T = 1$ K and $\Gamma = 0$. The other parameters are $\Delta = 0.54$ meV, $\lambda_R = 0.56$ meV, and $\lambda_v = 1.22$ meV [209]. The green curve is measured in units of e/h and the blue one in units of $e/10h$. The inset is a blowup of the region -2 meV $\leq E_F \leq 2$ meV.

line in the square brackets are to be evaluated at ϵ_{+F} and ϵ_{-F}, respectively, where $\epsilon_{\pm F}$ is obtained from Eq. (62) for $E = E_F$. To evaluate Eq. (72) numerically we used a Lorentzian broadening of $\delta(E_\xi^{\eta p} - E_F)$.

The valley P_v and spin P_s polarizations, corresponding to Eq. (72), are

$$P_v = \sum_{\xi p} \frac{\sigma_{xx}^d(l,s,+,p) - \sigma_{xx}^d(l,s,-,p)}{\sigma_{xx}^d(l,s,+,p) + \sigma_{xx}^d(l,s,-,p)}, \tag{74}$$

and

$$P_s = \sum_{\eta p l} \frac{\sigma_{xx}^d(l,+,\eta,p) - \sigma_{xx}^d(l,-,\eta,p)}{\sigma_{xx}^d(l,+,\eta,p) + \sigma_{xx}^d(l,-,\eta,p)}. \tag{75}$$

In Fig. 5.4 we plot the conductivity, given by Eq. (72), as a function of the Fermi energy E_F by evaluating the integral over k numerically for two values of the parameter Δ_Ω and $p = +1$.

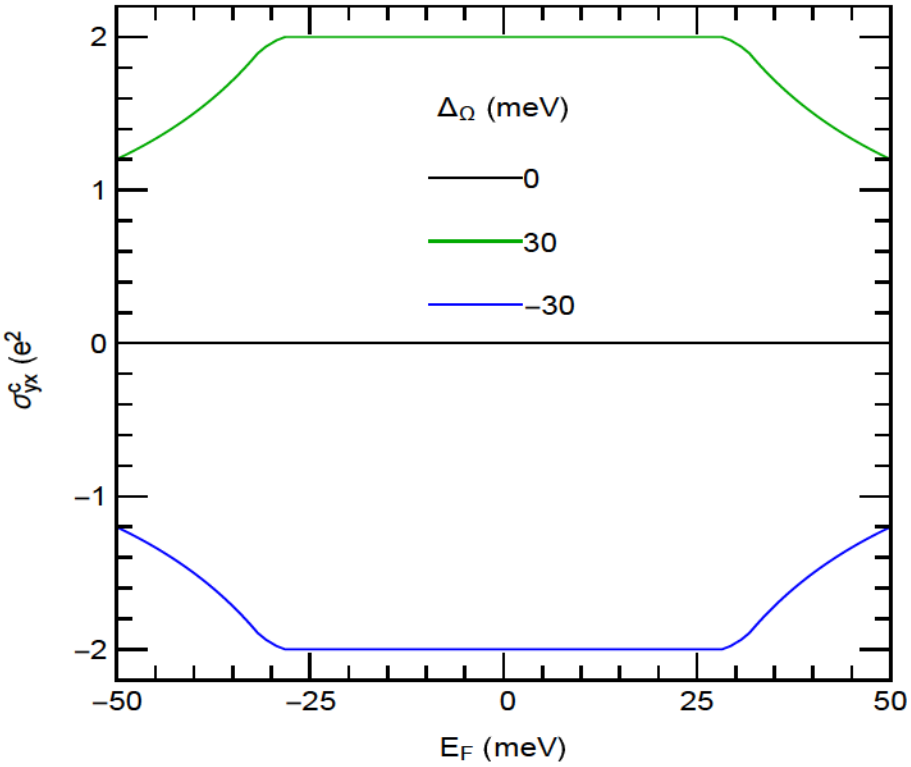

Figure 5.8: Charge Hall conductivity vs. E_F for different values of Δ_Ω. The other parameters are the same as in Fig. 5.7. It vanishes for $\Delta_\Omega = 0$ and changes sign when Δ_Ω is changed to $-\Delta_\Omega$.

Further, the left panel represents the valley-dependent contribution of Eq. (72), with both spins included, whereas the right one depicts its spin-dependent contribution with both valleys included. To display the result clearly, we set $\Delta = 1$ meV, $\lambda_R = 2$ meV, $\lambda_v = 4$ meV, and $\tau_F = 1 \times 10^{-15}$ sec. We find that $\sigma^d_{xx}(\xi, \eta, p)$ vanishes when E_F is in the gap while it increases linearly when E_F is outside the gap. The kink appears when E_F crosses the conduction band ($E^{\eta+}_{++}$). Moreover, we find $\sigma^d_{xx}(\xi, +, +) = \sigma^d_{xx}(\xi, -, +)$ in the inverted band regime ($\Delta_\Omega = 0$) while $\sigma^d_{xx}(\xi, +, +) \neq \sigma^d_{xx}(\xi, -, +)$ in the direct band regime ($\Delta_\Omega \neq 0$). We also verified that the analytical result (Eq. (73)) agrees well with the numerical one obtained from Eq. (72).

We plot the total longitudinal conductivity, with both valleys and spins included, in Fig. 5.5 for different values of Δ_Ω. As expected, σ^d_{xx} is an even function of Δ_Ω. In addition, the band gap increases with Δ_Ω.

The valley P_v and spin P_s polarizations versus E_F are shown in Fig. 5.6 for $\lambda_R = 4$ meV and three different values of Δ_Ω. It can be seen that $P_v = 0$ in the inverted band regime while

$P_v \neq 0$ in the direct band one. In other words, the valley polarization can be switched on and off by controlling the parameter Δ_Ω. On the other hand, $P_s \neq 0$ in both band regimes. It is interesting to study P_v in the direct band regime ($\Delta_\Omega \neq 0$). The contribution of $\sigma^d_{xx}(\xi,+)$ to P_v is zero in the range $\lambda_v + \Delta - \Delta_\Omega \leqslant E_F < \lambda_v + \Delta + \Delta_\Omega$. Thus, $P_v = 1$, which is a pure K' valley polarization for $\Delta_\Omega \neq 0$. When we change the polarization of light to $p = -1$, a pure K valley polarization is obtained. That is, one can easily reverse the valley polarization by reversing that of the circularly polarized light. This result may be useful in valleytronics applications, such as making valley valves [129].

In Fig. 5.7 we show the numerically evaluated valley-Hall conductivity σ^v_{yx}, from Eq. (86), in the inverted ($\Delta_\Omega = 0$) and direct ($\Delta_\Omega \neq 0$) band regimes for $l = l'$ with $s \neq s'$, as well as for $l \neq l'$ with $s = s'$ and $s \neq s'$. We used a sufficiently low temperature ($T = 1$ K) to ensure that thermal vibrations of atoms have a negligible contribution to the electron transport. σ^v_{yx} is quantized and has the universal value $2e^2/h$ when the Fermi level is in the gap -1 meV $\leq E_F \leq 1$ meV (see green curve, compare with the DOS in Fig. 2). Its absolute value is reduced outside the gap as E_F increases. The two peaks, to the left and right of the gap, at $E_F \approx \pm 1.5$ meV, appear due to the inverted band structure or the mexican hat-like dispersion as can be seen in the inset of Fig. 5.7. σ^v_{yx} vanishes when E_F is in the gap in the direct band regime $\Delta_\Omega \neq 0$ as the blue curve shows. The reason is that in this case electrons from both valleys flow in opposite directions and their contributions to the valley current exactly cancel each other. A non zero valley-Hall current is produced when E_F crosses the conduction and valence bands. When E_F grows further, the conductivity decreases. It is also worth noticing that the valley conductivity changes sign (not shown) if proximitized graphene is irradiated by a right circularly polarized light ($p = -1$).

For $\Delta_\Omega = 0$ a quantized valley-Hall conductivity of $2e^2/h$ is obtained in the band gap as can be seen from the green curve in the inset of Fig. 5.7. On the other hand, for $\Delta_\Omega \neq 0$ the valley-Hall conductivity is quenched to zero within the band gap (see the blue curve of Fig. 5.7), while a quantized charge Hall conductivity of $2e^2/h$ and $-2e^2/h$ is obtained for the left- and right-handed circularly polarized light, respectively, as shown in Fig. 5.8. The reason for the change $2e^2/h \rightarrow -2e^2/h$ is that this nondiagonal contribution to the conductivity is an odd function of Δ_Ω.

5.5 Summary and conclusion

We investigated the valley-dependent dc transport by employing the linear response formalism and Floquet theory in the high-frequency limit as well as the energy dispersion in the presence of proximity-induced gaps. We derived analytical expressions for the energy dispersion relation of Dirac fermions, the DOS, and the diagonal and nondiagonal parts of the conductivity. We found that a transition occurs from an inverted band regime to a direct one for $\Delta_\Omega > \Delta + \lambda_v$ (see Fig. 5.2). In addition, the energy dispersion shows a complete lifting of the *fourfold* spin and valley degeneracies in the direct band structure while it has a *twofold* valley degeneracy in the inverted band phase. We demonstrated that the DOS exhibits a van Hove singularity due to the inverted band structure, which remained unchanged as long as $\Delta_\Omega < \Delta + \lambda_v$. The four jumps in the DOS are due to the lifting of the fourfold spin and valley degeneracy in the direct band regime in contrast to pristine graphene, cf. Fig. 5.3.

We showed that the valley polarization P_v vanishes for $\Delta_\Omega < \Delta + \lambda_v$ while for $\Delta_\Omega > \Delta + \lambda_v$ it is finite, $P_v \neq 0$; this might be useful in the design of valleytronics devices such as optically controlled valley filters and valves based on proxitimized graphene. On the other hand, $P_s \neq 0$ in both band regimes. Further, 100% K or K' valley polarization is achieved in the range $\lambda_v + \Delta - \Delta_\Omega \leqslant E_F < \lambda_v + \Delta + \Delta_\Omega$ when the handedness of the light polarization changes.

We found that, when E_F in the gap, $\sigma^v_{yx} = 2e^2/h$ in the invert band regime while $\sigma^v_{yx} = 0$ in the direct band regime. Peaks are found in the curve of σ^v_{yx} versus E_F when E_F crosses the inverted dispersion, see the green curve in Fig. 5.7. Moreover, for $\Delta_\Omega > \Delta + \lambda_v$, we have $\sigma^v_{yx} \neq 0$ when E_F crosses the conduction and valence bands. The valley-Hall conductivity tends to $\sigma^v_{yx} = 0$ for both invert and direct band regimes in the limit $E_F \to \pm\infty$. A last finding is that the charge Hall conductivity is finite for $\Delta_\Omega \neq 0$ and changes sign when the handedness of the light polarization changes.

Our results may be pertinent to developing future spintronics and valleytronics devices such as field-effect tunnelling transistors, memory devices, phototransistors, etc.

5.6 Acknowledgments

M. Z. and P. V. acknowledge the support of the Concordia University Grant No. NGR034 and a Concordia University Merit Fellowship. The work of M. T. was supported by Colorado State University.

Chapter 6

Transport in armchair graphene nanoribbons and in ordinary waveguides

6.1 Abstract

We study dc and ac transport along armchair graphene nanoribbons using the $\mathbf{k}\cdot\mathbf{p}$ spectrum and eigenfunctions and general linear-response expressions for the conductivities. Then we contrast the results with those for transport along ordinary waveguides. In all cases we assess the influence of elastic scattering by impurities, describe it quantitatively with a Drude-type contribution to the current previously not reported, and evaluate the corresponding relaxation time for long- and short-range impurity potentials. We show that this contribution dominates the response at very low frequencies. In both cases the conductivities increase with the electron density and show cusps when new subbands start being occupied. As functions of the frequency the conductivities in armchair graphene nanoribbons exhibit a much richer peak structure than in ordinary waveguides: in the former intraband and interband transitions are allowed whereas in the latter only the intraband ones occur. This difference can be traced to that between the corresponding spectra and eigenfunctions.

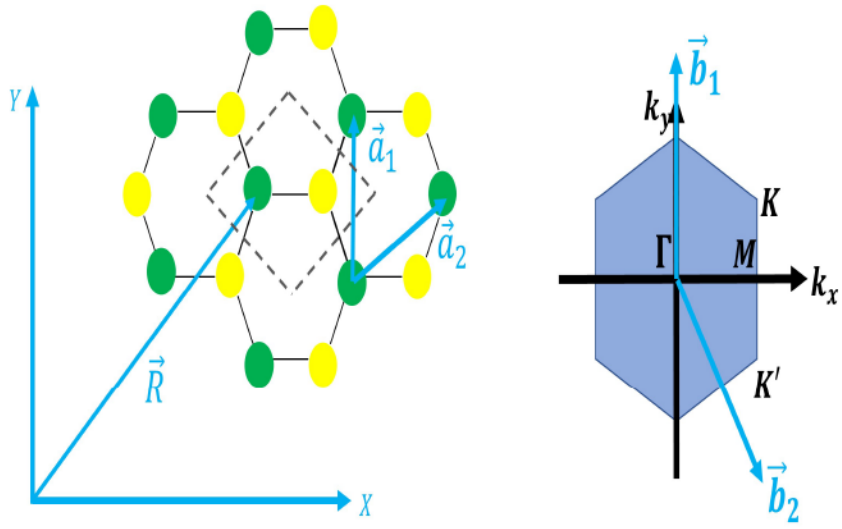

Figure 6.1: Left panel: Graphene unit cell (dashed rhombus) and its primitive vectors $\vec{a}_1$ and $\vec{a}_2$. Right panel: The corresponding Brillouin zone with $\vec{b}_1$ and $\vec{b}_2$ the reciprocal lattice vectors.

6.2 Introduction

Graphene nanoribbons have been studied extensively theoretically and experimentally. Previous studies focused on their electronic structure, spectrum, and eigenfunctions [265], optical properties [266, 267], elementary excitations [268], magnetic susceptibility [269, 270], excitonic effects [271]. A short review of transport properties, focused on localization concepts, appeared in Ref. [272], some numerical results in Ref. [273], numerically studied thermal transport in Ref. [274], and spin tranport in substitutionally doped, zig-zag graphene nanoribbons in Ref. [275]. Experimental results have also been reported [276]. The influence of impurity scattering or disorder though has received a limited attention [275]. In particular, we are not aware of any study of dc and ac transport, say, within linear-response theory, that takes into account scattering by randomly distributed impurities, most of the studies use scattering-independent Kubo formulas or consider scattering numerically.

In this work we study dc and ac transport along armchair graphene nanoribbons (AGNRs) or ordinary waveguides using linear-response, scattering-dependent and scattering-independent expressions for the conductivities. In the former case we evaluate the relaxation time for long- and short-range impurity potentials. We present the basics in Sec. 6.3 and the conductivities in Sec. 6.4. A summary follows in Sec. 6.5.

6.3 AGNRs, ordinary waveguides

6.3.1 AGNRs

Graphene is a two-dimensional, one-atom thick planar sheet of bonded carbon atoms densely packed in a honeycomb structure as shown in the left panel of Fig. 6.1. In it the ribbon extends along the x axis while the graphene sheet is confined along the y axis. The lattice structure can be viewed as a triangular lattice with two sites A (green filled circles) and B (yellow filled circles) per unit cell as shown by the rectangular box in the left panel of Fig. 6.1. The arrows indicate the primitive lattice vectors $\vec{a}_1 = a(0,1)$ and $\vec{a}_2 = a(1/2, \sqrt{3}/2)$, with a the triangular lattice constant of the structure, and span the graphene lattice. Further, $\vec{a}_1$ and $\vec{a}_2$ generate the reciprocal lattice vectors of the Brillouin zone, cf. Fig. 6.1, given by $\vec{b}_2 = 4\pi/\sqrt{3}a(\sqrt{3}/2, -1/2)$ and $\vec{b}_1 = 4\pi/\sqrt{3}a(0,1)$. From the explicit expressions of $\vec{b}_1$ and $\vec{b}_2$ we find the two inequivalent Dirac points (valleys) given by $\vec{K} = 4\pi/3a(0,1)$ and $\vec{K}' = 4\pi/3a(0,-1)$. The $\mathbf{k}\cdot\mathbf{p}$ Hamiltonian near the Dirac points reads

$$H = \hbar v_F \begin{pmatrix} 0 & k_- & 0 & 0 \\ k_+ & 0 & 0 & 0 \\ 0 & 0 & 0 & k_+ \\ 0 & 0 & k_- & 0 \end{pmatrix}, \tag{76}$$

where $\hbar$ is Plank's constant, v_F the Fermi velocity, and $k_\pm = k_y \pm i k_x$. The resulting eigenfunctions of Eq. (76) for AGNRs, shown in Fig. 6.2, take the form

$$\psi_{n,\eta,k_x} = \frac{1}{2\sqrt{LW}} \begin{pmatrix} \eta e^{-i\theta_{k_{yn},k_x}} e^{ik_{yn}y} \\ e^{ik_{yn}y} \\ -\eta e^{-i\theta_{k_{yn},k_x}} e^{-ik_{yn}y} \\ e^{-ik_{yn}y} \end{pmatrix} e^{ik_x x}, \tag{77}$$

where $\theta_{k_{yn},k_x} = \tan^{-1}(k_x/k_{yn})$. The energy dispersion of graphene AGNRs corresponding to Eq. (76) is [265]

$$E^n_{\eta,k_x} = \eta\hbar v_F \varepsilon, \quad \varepsilon = [k_{yn}^2 + k_x^2]^{1/2}, \tag{78}$$

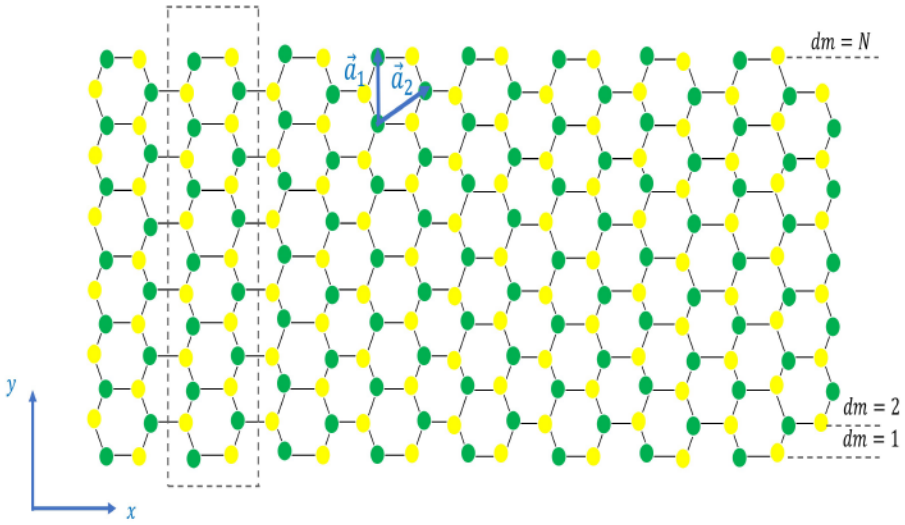

Figure 6.2: Geometry of an AGNR. The dashed box shows the unit cell and dm represents the dimmer number.

where $\eta = +1(-1)$ stands for the conduction (valence) band. The allowed values of k_{yn} are [265, 266, 268, 269]

$$k_{yn} = \frac{n\pi}{W} - \frac{4\pi}{3a} = \frac{2\pi(3n - 2(dm+1))}{3a(dm+1)}; \tag{79}$$

here $W = a(dm+1)/2$ is the ribbon width, dm the number of rows of AGNRs, $a = \sqrt{3}a_{cc}$, $a_{cc} \approx 1.42$ Å is the carbon-carbon distance, and $n = 1, 2, ..., N$ is the subband index with N the maximum number of dimmers. It follows from Eq. (79), if $3n - 2(dm+1) = 0$, then $k_{yn} = 0$ for particular n. So, a zero energy state appears near $k_x \to 0$ as in graphene, whereas the other states have band gap because $3n - 2(dm+1) \neq 0$. The energy dispersions for semiconducting $(dm = 4)$ and metallic $(dm = 5)$ nanoribbons are shown in Fig. 6.3.

Velocity matrix elements. To evaluate the various conductivities we need the matrix elements of the velocity operators $v_x = \partial H/\hbar\partial k_x$ and $v_y = \partial H/\hbar\partial k_y$. With

$$v_x = v_F \begin{pmatrix} \sigma_y & 0 \\ 0 & -\sigma_y \end{pmatrix}, \; v_y = v_F \begin{pmatrix} \sigma_x & 0 \\ 0 & \sigma_x \end{pmatrix}, \tag{80}$$

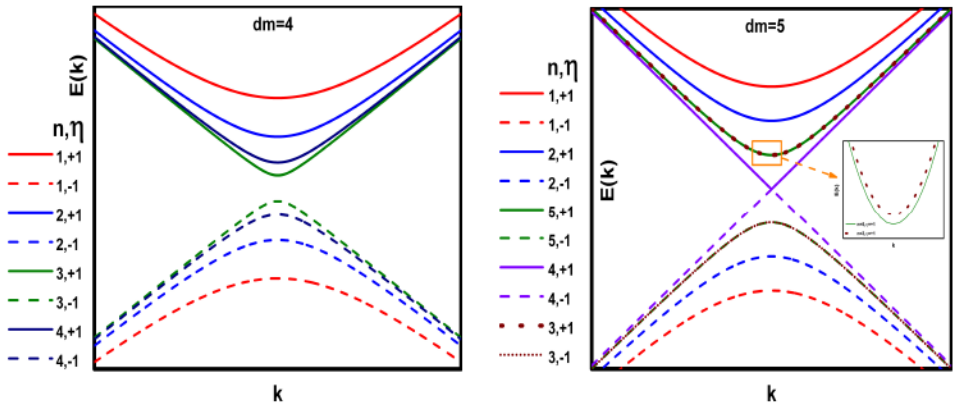

Figure 6.3: Single-particle energy dispersion in AGNRs with $k = ak_x$. The left panel is for semiconducting (dm=4) and the right one for metallic (dm=5) AGNRs. The insect in the right panel shows the dispersion for $\eta = +1$ and n=3, 5 .

their matrix elements ($|\zeta\rangle = |n, \eta, k_x\rangle$) are

$$\langle\zeta'|\, v_x \,|\zeta\rangle = N(\eta e^{i\theta_{k'_{yn},k'_x}} - \eta' e^{-i\theta_{k_{yn},k_x}})\delta_{n,n'}\delta_{k_x,k'_x} \tag{81}$$

$$\langle\zeta|\, v_y \,|\zeta'\rangle = M(\eta' e^{i\theta_{k_{yn},k_x}} + \eta e^{-i\theta_{k'_{yn},k'_x}})\delta_{k_x,k'_x},\ n \neq n', \tag{82}$$

with $e^{\pm i\theta_{k_{yn},k_x}} = (k_{yn} \pm ik_x)/\varepsilon_{k_x}$, $N = -iv_F/2$, and $M = -iv_F/\pi(n-n')$.

6.3.2 Ordinary waveguides

In Fig. 6.4 we consider an ordinary quantum wire along the x axis generated by confining a 2DEG along the y direction. We assume the confining potential $V(y)$ to be parabolic, i.e., $V(y) = m^*\omega_0^2 y^2/2$. The eigenvalues are

$$E_{nk_x} = (n + 1/2)\hbar\omega_0 + \hbar^2 k_x^2/2m^*, \tag{83}$$

and the corresponding eigenfunctions

$$\psi_{nk_x} = (2^n n!\sqrt{\pi}\ell)^{-1/2} H_n(y/\ell)\, e^{-y^2/2\ell^2} e^{ik_x x} \tag{84}$$

with $\ell = (\hbar/m^*\omega_0)^{1/2}$ and $H_n(y/\ell)$ the Hermite polynomials. Here only the diagonal matrix elements $v_x = \hbar k_x/m^*$ are relevant since the nondiagonal ones ($\langle\zeta'|\, v_x \,|\zeta\rangle$) vanish. However, the

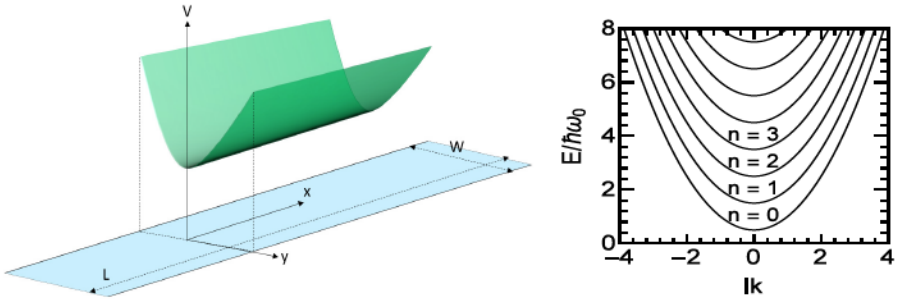

Figure 6.4: Geometry of a parabolically confined (left panel), along the y direction, quantum wire of width $L_y = W$ and length $L_x = L$. The right panel shows the wire's spectrum.

nondiagonal velocity matrix elements ($\langle\zeta|\, v_y \,|\zeta'\rangle$) along the confinement direction are non zero and given as

$$\langle\zeta|\, v_y \,|\zeta'\rangle \;=\; N_n\big[(n'+1)\delta_{n'+1,n} - (1/2)\delta_{n'-1,n}\big]\delta_{k_x k'_x} \tag{85}$$

where $N_n = (i\hbar/m^*\ell)(2^{n'}n'!/2^n n!)^{1/2}$. It is evident from the right panel of Fig. 6.4 that the spectrum consists of a set of equidistant, oscillator subbands due to the harmonic confinement along the y direction.

6.4 Conductivities

We consider a many-body system described by the Hamiltonian $H = H_0 + H_I - \mathbf{R}\cdot\mathbf{F}(t)$, where H_0 is the unperturbed part, H_I is a binary-type interaction (e.g., between electrons and impurities or phonons), and $-\mathbf{R}\cdot\mathbf{F}(t)$ is the interaction of the system with the external field F(t) [128]. For conductivity problems we have $\mathbf{F}(t) = e\mathbf{E}(t)$, where $\mathbf{E}(t)$ is the electric field, e the electron charge, $\mathbf{R} = \sum_{\mathbf{r_i}}$, and $\mathbf{r_i}$ the position operator of electron i. In the representation in which H_0 is diagonal the many-body density operator $\rho = \rho^d + \rho^{nd}$ has a diagonal part ρ^d and a nondiagonal part ρ^{nd}. For weak electric fields and weak scattering potentials, for which the first Born approximation applies, the conductivity tensor has a diagonal part $\sigma^d_{\mu\nu}$ and a nondiagonal part $\sigma^{nd}_{\mu\nu}$; the total conductivity is $\sigma^T_{\mu\nu} = \sigma^d_{\mu\nu} + \sigma^{nd}_{\mu\nu}, \mu, \nu = x, y$.

In general we have two kinds of currents, diffusive and hopping, with $\sigma^d_{\mu\nu} = \sigma^{dif}_{\mu\nu} + \sigma^{col}_{\mu\nu}$, but usually only one of them is present. If no magnetic field is present, the hopping term $\sigma^{col}_{\mu\nu}$ vanishes

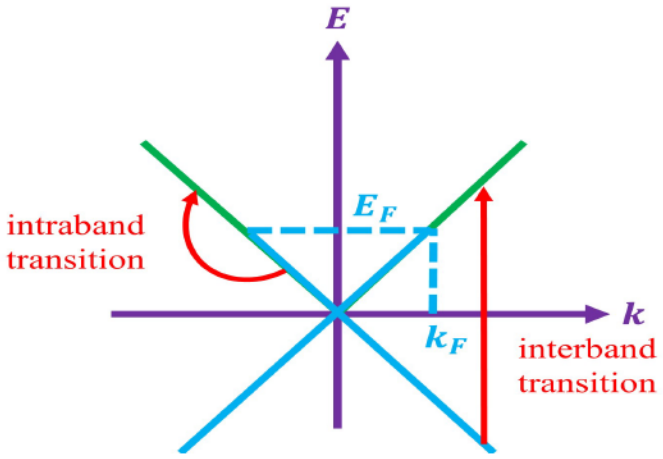

Figure 6.5: Schematic representation of intraband and interband transitions in the energy dispersion of a metallic AGNR.

identically [128] and only the term $\sigma_{\mu\nu}^{dif}$ survives. For elastic scattering it is given by [128, 215]

$$\sigma_{\mu\nu}^{d}(\omega) = \frac{\beta e^2}{S_0} \sum_{\zeta} f_\zeta (1 - f_\zeta) \frac{v_{\nu\zeta} v_{\mu\zeta} \tau_\zeta}{1 + i\omega\tau_\zeta}, \tag{86}$$

where τ_ζ is the momentum relaxation time, ω the frequency, and $v_{\mu\zeta}$ the diagonal matrix elements of the velocity operator. Further, $f_\zeta = [1 + \exp\beta(E_\zeta - E_F)]^{-1}$ is the Fermi-Dirac distribution function, $\beta = 1/k_B T$, T the temperature, k_B the Boltzmann constant, and S_0 the area of the sample.

Regarding the contribution $\sigma_{\mu\nu}^{nd}$ one can use the identity $f_\zeta(1 - f_{\zeta'})[1 - \exp\beta(E_\zeta - E_{\zeta'})] = f_\zeta - f_{\zeta'}$ and cast the original form in the more familiar one [128, 215]

$$\sigma_{\mu\nu}^{nd}(\omega) = \frac{i\hbar e^2}{S_0} \sum_{\zeta \neq \zeta'} \frac{(f_\zeta - f_{\zeta'}) v_{\nu\zeta\zeta'} v_{\mu\zeta\zeta'}}{(E_\zeta - E_{\zeta'})(E_\zeta - E_{\zeta'} + \hbar\omega - i\Gamma)}, \tag{87}$$

where the sum runs over all quantum numbers $|\zeta\rangle$ and $|\zeta'\rangle$ with $\zeta \neq \zeta'$. The infinitesimal quantity ϵ in the original form [128] has been replaced by Γ_ζ to account for the broadening of the energy levels. In Eq. (87) $v_{\nu\zeta\zeta'}$ and $v_{\mu\zeta\zeta'}$ are the nondiagonal matrix elements of the velocity operator. Further, diagonal and nondiagonal contributions describe intraband and interband transitions, respectively, as shown schematically in Fig. 6.5.

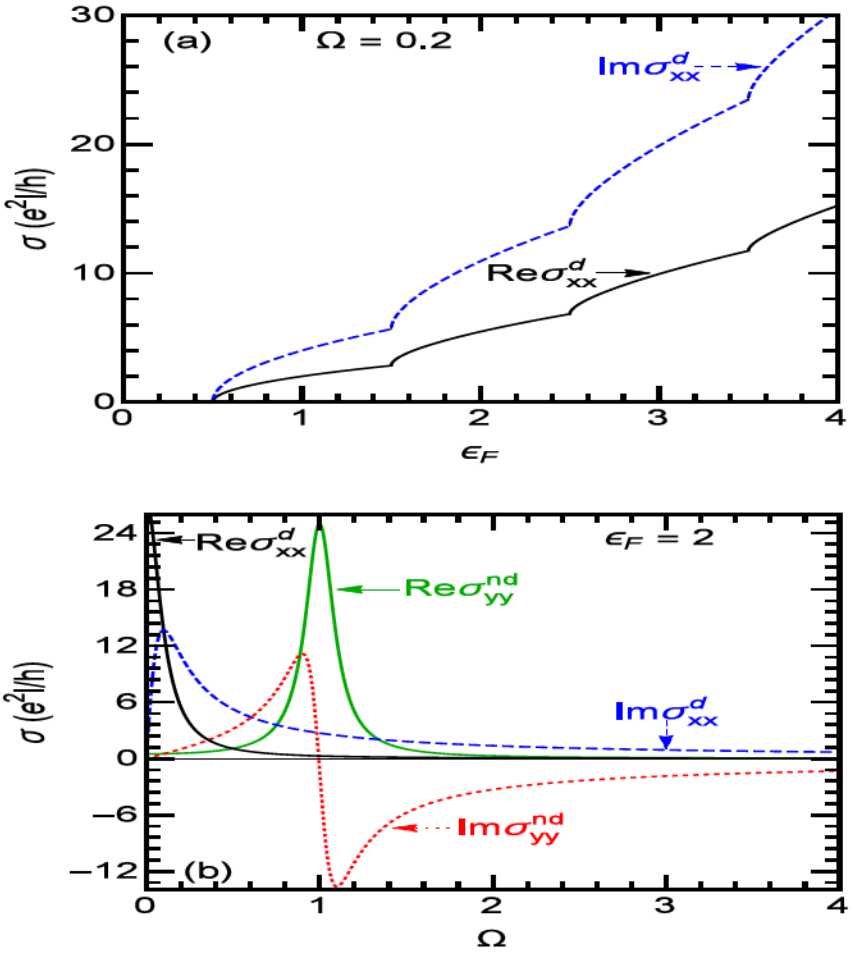

Figure 6.6: Diagonal conductivity, in units of $e^2\ell/h$ of an ordinary waveguide vs $\varepsilon_F = E_F/\hbar\omega_0$ in (a) and vs photon energy ($\Omega = \omega/\omega_0$) in (b). The black (blue) curves are for Reσ^d_{xx} (Imσ^d_{xx}) and the dark green (red dotted) ones are for Reσ^{nd}_{yy} (Imσ^{nd}_{yy}). Here we used $\gamma = \Gamma/\hbar\omega_0 = 0.1$.

6.4.1 Diagonal conductivity in ordinary waveguides

For $\omega = 0$ and $\mu = \nu = x$ Eq. (86) becomes

$$\sigma_{xx} = \frac{\beta e^2}{L}\sum_{nk_x} f_{nk_x}(1 - f_{nk_x})\, v_x^2\, \tau_{nk_x}. \tag{88}$$

For very low temperatures, we make the approximation $\beta f_{nk_x}(1 - f_{nk_x}) \approx \delta(E_{nk_x} - E_F)$, replace τ_ζ by τ_F, and use the prescription $\sum_{k_x} \to (L_x/2\pi)\int dk_x$. Then Eq. (88), with $v_x = \hbar k_x/m^*$,

takes the form

$$\sigma^{d}_{xx}(i\omega) = \frac{\sigma_0\tau_F}{(1+i\omega\tau_F)}\sum_n \sqrt{E_F - E_n}, \tag{89}$$

where $E_n = (n+1/2)\hbar\omega_0$ and $\sigma_0 = e^2/\pi\hbar\sqrt{2m^*}$. For the dc conductivity we simply set $\omega = 0$.

In Fig. 6.6 we show the diagonal conductivity as a function of E_F (upper panel) and photon energy (lower panel) for $\hbar\omega_0 = 0.5$ meV [277]. The conductivity increases with the increase of E_F but cusps appear due to the presence of discrete levels in the lateral direction produced by the parabolic confinement. In addition, σ^{d}_{xx} vanishes when the Fermi level is in the range $0 \leqslant \varepsilon_F \leqslant 0.5$ since the electron density is null in this range of energy. We can see that $\mathrm{Re}\sigma^{d}_{xx}$ has a Drude-type peak around $\Omega = 0$ while $\mathrm{Im}\sigma^{d}_{xx}$ has peak around $\Omega = 0.1$ as can be seen in the lower panel of Fig. 6.6. Furthermore, it can also be seen that the Drude-type contribution survives at low frequencies while it vanishes at higher frequencies. Note that the nondiagonal contribution σ^{nd}_{xx} to the conductivity of 2DEG when confined in a ribbon vanishes, since the velocity matrix elements are diagonal, whereas we will find below that it survives in graphene ribbons.

6.4.2 Nondiagonal conductivity in ordinary waveguides

With the help of matrix elements (85) and $|\zeta\rangle = |n, k_x\rangle$, we can recast Eq. (87) as

$$\begin{aligned}\sigma^{nd}_{yy}(i\omega) = & -\frac{ie^2}{4\pi\sqrt{2m^*}}\sum_n \int_{|E_n|}^{E_m} dE \frac{(n+1)(f^n_{k_x} - f^{n+1}_{k_x})}{[E-E_n]^{1/2}} \\ & \times\left[\frac{\hbar\omega_0 + \hbar\omega + i\Gamma}{(\hbar\omega_0+\hbar\omega)^2+\Gamma^2} - \frac{\hbar\omega_0 - \hbar\omega - i\Gamma}{(\hbar\omega_0-\hbar\omega)^2+\Gamma^2}\right]\end{aligned} \tag{90}$$

where $E_m = E_n + \hbar^2k_m^2/2m^*$. In the limit $\Gamma = \omega = 0$, one can show that $\sigma^{nd}_{yy}(i\omega)$ vanishes.

In Fig. 6.6 (b), we have plotted the numerically evaluated $\mathrm{Re}\sigma^{nd}_{yy}$ (dark green curve) and $\mathrm{Im}\sigma^{nd}_{yy}$ (red dotted curve) as functions of the dimensionless photon energy ($\Omega = \omega/\omega_0$). We can see that $\mathrm{Re}\sigma^{nd}_{yy}$ is finite at $\Omega = 0$, due to $\Gamma \neq 0$, and attains a maximum value at $\Omega = 1$. Upon further increasing $\Omega(\geqslant 1)$ we see that $\mathrm{Re}\sigma^{nd}_{yy}$ approaches to zero. On the other hand, we observe that $\mathrm{Im}\sigma^{nd}_{yy}$ acquires positive and negative values due to the $\hbar\omega_0 - \hbar\omega$ factor in Eq. (90). For $\hbar\omega_0 > \hbar\omega$, the second term of Eq. (90) is greater than the first one and we find the positive peak. However,

we obtain a negative absorption peak for $\hbar\omega_0 < \hbar\omega$. It can also be seen from Eq. (90) that only intraband transitions occur in contrast to AGNRs where both intraband and interband transitions occur, see Eqs. (103)-(104) below.

6.4.3 Diagonal conductivity in AGNRs

τ = constant

From Eq. (78) we readily find the velocity

$$v_x = \eta v_F k_x/\varepsilon. \tag{91}$$

Substituting Eq. (91) in Eq. (86), using $\beta f^n_{\eta k_x}(1 - f^n_{\eta k_x}) \approx \delta(E^n_{\eta k_x} - E_F)$ and $\tau^n_{\eta k_x} = \tau_F$ at zero temperature, and performing the integration over $k_x((L_x/2\pi)\int dk_x)$, we find the conductivity expression of AGNRs for finite ω as

$$\sigma^d_{xx}(i\omega) = \frac{e^2 v_F \tau_F}{h(1+i\omega\tau_F)} \sum_n \frac{X_{Fn}}{\varepsilon_F}, \tag{92}$$

where $X_{Fn} = [\varepsilon_F^2 - k_{yn}^2]^{1/2}, \varepsilon_F = E_F/\hbar v_F$, and the summation terminates at the last occupied level. Equation (92) is only valid for $\varepsilon_F \geqslant k_{yn}$. For $k_{yn} = 0$ it reduces to

$$\sigma^d_{xx}(i\omega) = \frac{e^2 v_F \tau_F}{h(1+i\omega\tau_F)}\, n_F, \tag{93}$$

where n_F is the number of occupied levels.

$\tau \neq$ constant

Long-range impurities. Using Eqs. (91), (120), and the same assumptions, as given above Eq. (92), in Eq. (86) we obtain for $\omega = 0$ and $\eta = +1$

$$\sigma^d_{xx}(0) = \frac{e^2 A}{h} \sum_n \frac{X^2_{Fn}}{\varepsilon^2_F} \Big[\frac{k_s^2 + 4X^2_{Fn}}{k_s + [k_s^2 + 4X^2_{Fn}]^{1/2}}\Big], \tag{94}$$

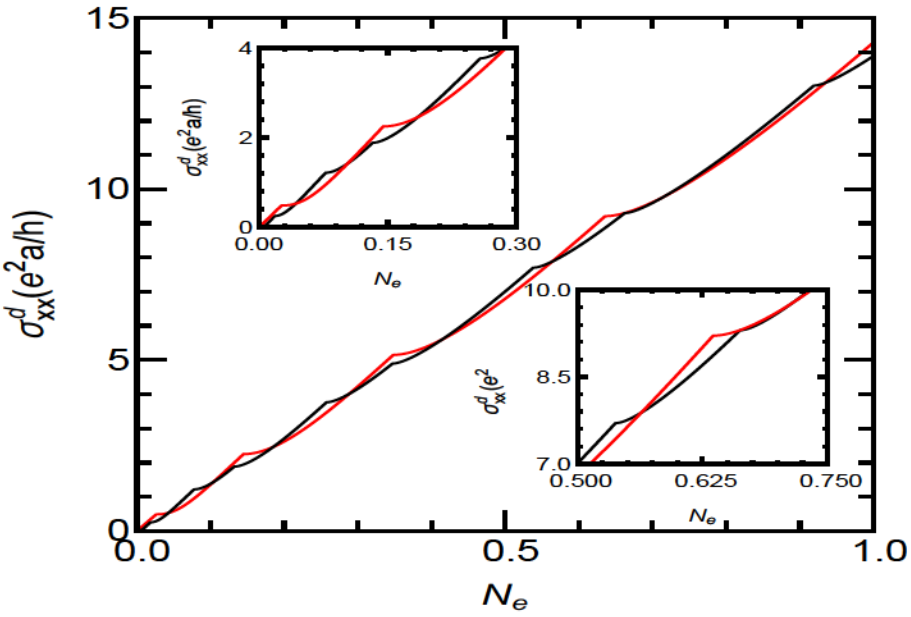

Figure 6.7: Conductivity σ^d_{xx} for screened Coulomb scatterers as a function of the dimensionless carrier density ($N_e = an_e/2\pi$) for semiconducting (black curves) and metallic (red curves) nanoribbons. Cusps in the curves appear when new subbands are occupied by increasing the electron density. For further clarity the ranges $0-0.3$ and $0.5-75$ are shown in the insets.

with $A = 2\hbar^2 v_F^2/n_i U_s^2$. For $k_{yn} = 0$ Eq. (94) becomes

$$\sigma^d_{xx}(0) = \frac{e^2 A}{h} \frac{k_s^2 + 4\varepsilon_F^2}{k_s + [k_s^2 + 4\varepsilon_F^2]^{1/2}}\, n_F. \tag{95}$$

Short-range impurities. We consider the potential $U(x) = U_0\, \delta(x - x_i)$ with U_0 its constant strength and x_i the position of the impurity. Corresponding to Eq. (94) we find the dc conductivity is now given by

$$\sigma^d_{xx}(0) \;=\; \frac{e^2 B}{h} \sum_n \frac{X^2_{Fn}}{\varepsilon_F^2}, \tag{96}$$

where $B = \pi\hbar^2 v_F^2/2n_i U_0^2$. For $k_{yn} = 0$ Eq. (96) becomes

$$\sigma^d_{xx}(0) = \frac{e^2 B}{h} n_F. \tag{97}$$

For the finite frequency ω results we simply divide those of Eqs. (94)-(97) by $1 + i\omega\tau_F$.

In Fig. 6.7, we plot σ^d_{xx} as a function of the dimensionless carrier density ($N_e = an_e/2\pi$)

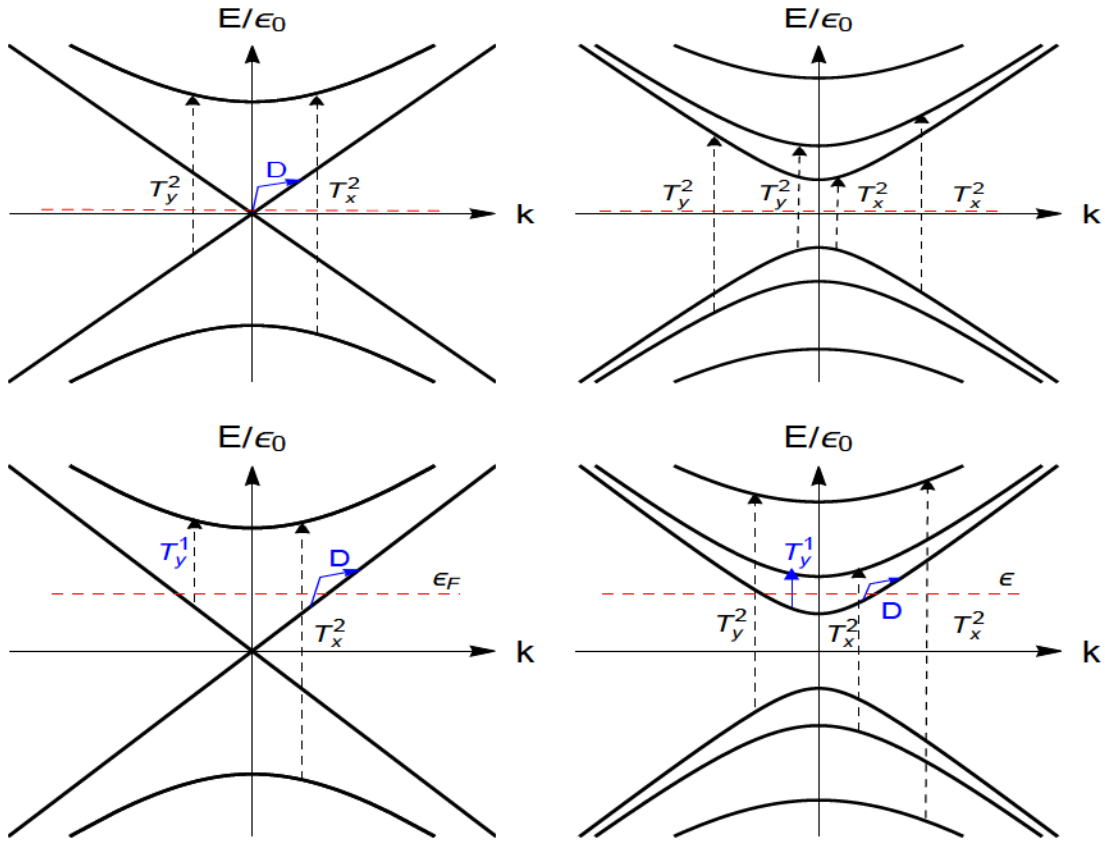

Figure 6.8: Schematic representation of some allowed transitions indicated by arrows. The horizontal red dashed lines show the Fermi level. T_y^i and T_x^i denote intraband $(i = 1)$ and interband $(i = 2)$ transitions, respectively at the peaks of σ_{yy} and σ_{xx} in Fig. 6.9, see Eqs. (100)-(104), while D represents the Drude-type intraband transition, cf. Eq. (92).

for $dm = 4$ (black line) and $dm = 5$ (red line). The relevant relaxation time is given by Eq. (120) in appendix. The factor k_s can be approximated by the Thomas-Fermi wave vector $k_s = (2\pi e^2/\epsilon)D(E_F)$ with ϵ the relative dielectric constant and $D(E_F)$ the density of states at the Fermi level. We can see that σ_{xx}^d increases almost linearly from 0 with the peaks at critical value of N_e. These peaks appear when the subbands start to be occupied by electrons,. Also, this behaviour is consistent with the band structures, cf. Fig. 6.3. These jumps are absent in the conductivity of graphene [218, 219]. Further, we observe the richer structure of peaks for semiconducting ribbons than metallic ones due to the opening of gaps among the subbands of semiconducting nanoribbons as can be seen by comparing the left and right panels of Fig. 6.3. It is worth mentioning that this scattering-dependent contribution was not accounted for in previous studies, see, e.g., Refs. [266, 269].

6.4.4 Nondiagonal conductivity in AGNRs

With $|\zeta\rangle = |n, \eta, k_x\rangle$ Eq. (87) becomes

$$\sigma_{xx}^{nd}(i\omega) = \frac{i\hbar e^2}{L_x} \sum_{\eta\eta' nn' k_x k_x'} \frac{f_{\eta k_x}^n - f_{\eta' k_x}^{n'}}{E_{\eta k_x}^n - E_{\eta' k_x}^{n'}} \frac{v_{x\eta\eta' k_x}^{nn'} v_{x\eta'\eta k_x}^{n'n}}{E_{\eta k_x}^n - E_{\eta' k_x}^{n'} + \hbar\omega + i\Gamma_{\eta\eta' k_x k_x'}^{nn'}}, \tag{98}$$

where $v_{x\eta\eta' k_x}^{nn'} = \langle n', \eta', k_x'|v_x|n, \eta, k_x\rangle$ and $v_{x\eta'\eta k_x}^{n'n} = \langle n', \eta', k_x'|v_x|n, \eta, k_x\rangle$ are the nondiagonal matrix elements of the velocity operator. Further, the velocity matrix element (81) is diagonal in k_x, therefore k_x will be suppressed in order to simplify the notation. The summation in Eq. (98) runs over all quantum numbers n,n', η, η', and k_x. The parameter $\Gamma_{\eta\eta'}^{nn'}$, that takes into account the level broadening, is assumed to be independent of the band and subband indices i.e. $\Gamma_{\eta\eta'}^{nn'} = \Gamma$. Also, we will simplify the notation over summation by considering the subband orthogonality $\delta_{k_{yn}k_{yn}'}$. Hence, after expanding the fraction, Eq. (98) can be rewritten as

$$\sigma_{xx}^{nd}(i\omega) = \frac{i\hbar e^2}{L_x} \sum_{\eta\eta' n k_x} \frac{(f_{\eta k_x}^n - f_{\eta' k_x}^n) v_{x\eta\eta' k_x}^{nn} v_{x\eta'\eta k_x}^{nn}}{E_{\eta k_x}^n - E_{\eta' k_x}^n} \frac{E_{\eta k_x}^n - E_{\eta' k_x}^n + \hbar\omega - i\Gamma}{(E_{\eta k_x}^n - E_{\eta' k_x}^n + \hbar\omega)^2 + \Gamma^2}. \tag{99}$$

We evaluate Eq. (99) by considering the summation over $\eta = +1$, $\eta' = -1$, and $\eta = -1$, $\eta' = +1$, denoted by $\sum_{-+}$ and $\sum_{+-}$. For $\eta = \eta'$ the contributions $\sum_{++}$ and $\sum_{--}$ to $\mathrm{Re}\sigma_{xx}^{nd}(i\omega)$ are not allowed due to the condition $\zeta \neq \zeta'$, cf. Eqs. (81) and (86). Hence, the summation over $\eta = \eta'$ is given only by the Drude-type, intraband contribution $\sigma_{xx}^{d}(i\omega)$ to the total conductivity, see Eqs. (90) and (92).

The real and imaginary parts corresponding to Eq. (99) read

$$\mathrm{Re}\sigma_{xx}^{nd}(i\omega) = -\frac{e^2 v_F}{4\pi} \sum_n \int_{|k_{yn}|}^{\varepsilon_m} d\varepsilon \frac{k_{yn}^2 (f_{-k_x}^n - f_{+k_x}^n)}{\varepsilon^2 [\varepsilon^2 - k_{yn}^2]^{1/2}} (C_+ + C_-), \tag{100}$$

and

$$\mathrm{Im}\sigma_{xx}^{nd}(i\omega) = -\frac{e^2 v_F}{4\pi} \sum_n \int_{|k_{yn}|}^{\varepsilon_m} d\varepsilon \frac{k_{yn}^2 (f_{-k_x}^n - f_{+k_x}^n)}{\varepsilon^2 [\varepsilon^2 - k_{yn}^2]^{1/2}} (R_+ - R_-), \tag{101}$$

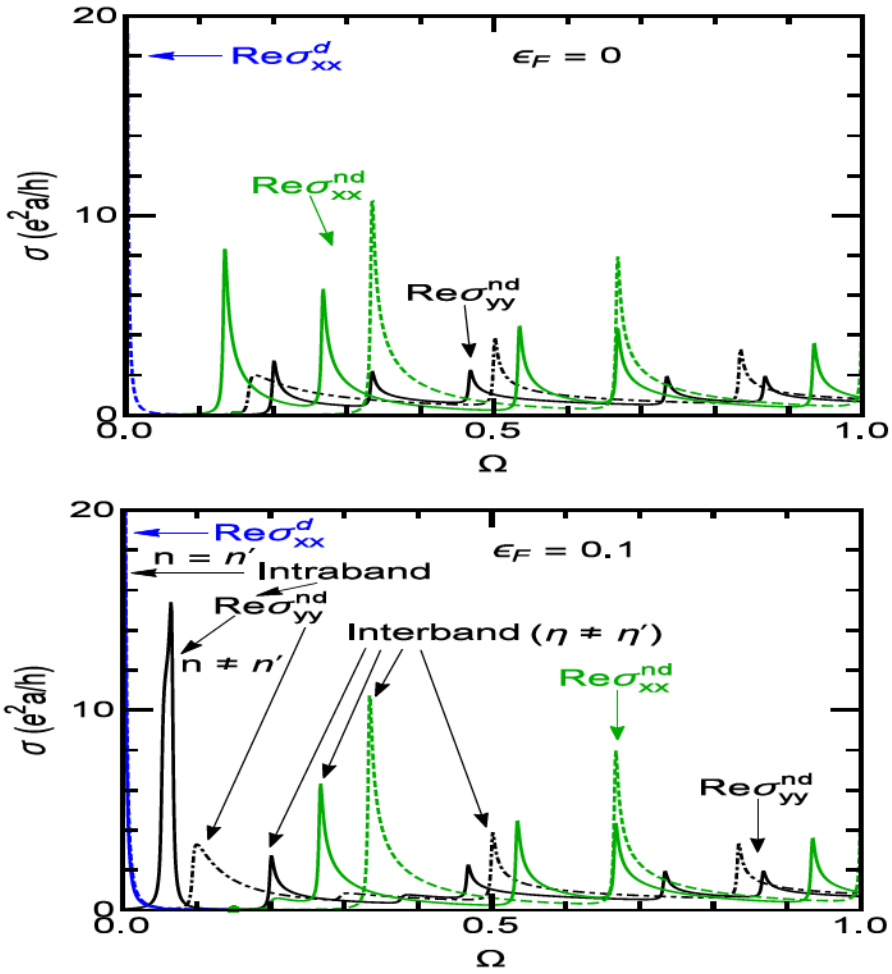

Figure 6.9: Real part of the conductivity vs frequency for $\varepsilon_F = 0$ (upper panel) and $\varepsilon_F = 0.1$ (lower panel, $k_BT/\varepsilon_0 = 0.001$, and $\Gamma/\varepsilon_0 = 0.002$. The solid curves are for semiconducting nanoribbons ($dm = 4$) and the dotted ones are for metallic ribbons ($dm = 5$).

with $\varepsilon_m = (k_m^2 + k_{yn}^2)^{1/2}$ and k_m the maximum value of k_x below for which the $\mathbf{k}\cdot\mathbf{p}$ theory is valid. Further, $v^{nn}_{x-+k_x}v^{nn}_{x+-k_x} = v^{nn}_{x+-k_x}v^{nn}_{x-+k_x} = v_F^2k_{yn}^2/\varepsilon^2$ [see Eq. (81)], $C_\pm = \Gamma((2\hbar v_F\varepsilon \pm \hbar\omega)^2 + \Gamma^2)^{-1}$, and $R_\pm = (2\hbar v_F\varepsilon \pm \hbar\omega)((2\hbar v_F\varepsilon \pm \hbar\omega)^2 + \Gamma^2)^{-1}$. In the limit $k_{yn} = 0$, the real and imaginary parts of the nondiagonal conductivity will vanish as is evident from Eqs. (100)-(101). Further, for $\omega = 0$ and $\Gamma \neq 0$, the real part [see Eq. (100)] of the nondiagonal conductivity survives whereas the imaginary one vanishes [see Eq. (101)]. Also, it can be seen from Eqs. (100) and (101) that transitions occur between the valence and conduction band with the same index n. Some of these transitions are shown schematically in Fig. 6.8 for two values of the Fermi level (dashed red lines) with T_y^i and T_x^i denoting the intraband ($i = 1$) and interband ($i = 2$) ones, respectively at the

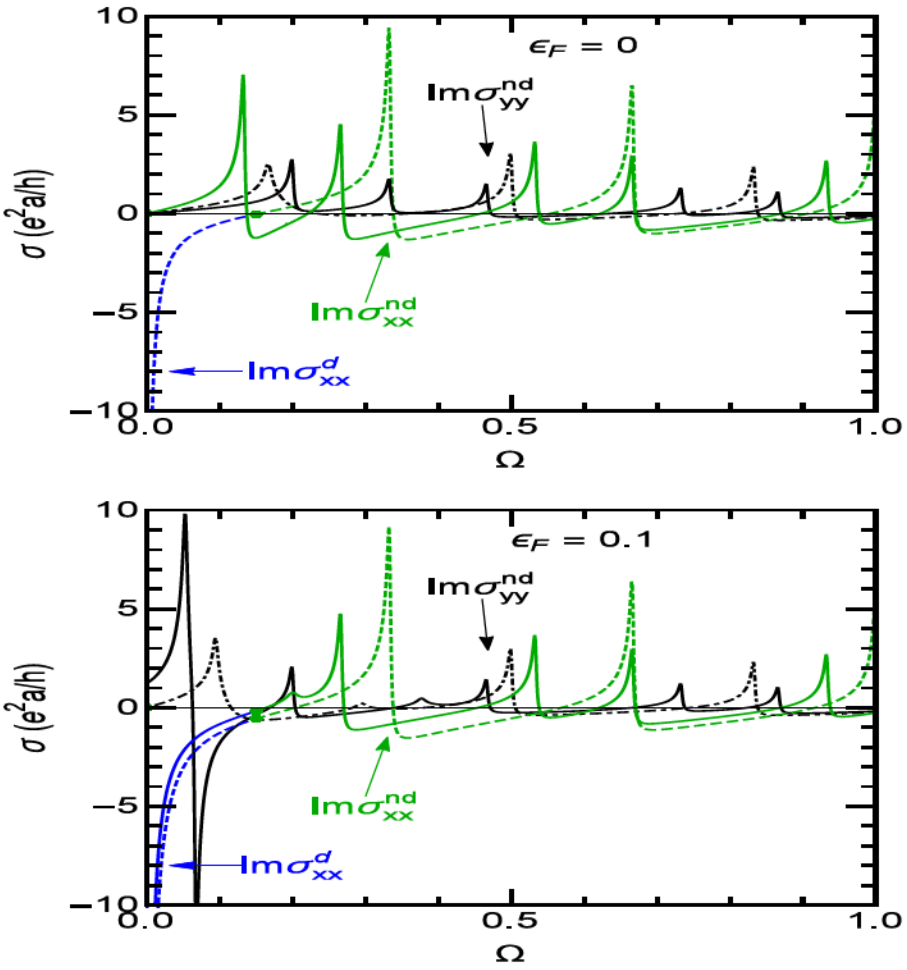

Figure 6.10: As in Fig. 6.9 but for the imaginary part of the total conductivity vs frequency.

peaks of σ^{nd}_{xx} and σ^{nd}_{yy}.

For $T = 0$ and E_F in the gap we have $f^n_{-k_x} = 1$ and $f^n_{+k_x} = 0$. After evaluating the integrals over ε in Eqs. (100)-(101) we rewrite them in the combined form

$$\sigma^{nd}_{xx}(i\omega) \;=\; \frac{ie^2U_+}{h(\omega_1^2+\Gamma_1^2)}\sum_n\left[1+\frac{2iU_+k^2_{yn}}{(\omega_1^2+\Gamma_1^2)p}\ln\frac{Q_+}{Q_-}\right], \tag{102}$$

where $\omega_1 = \hbar\omega/\hbar v_F$, $\Gamma_1 = \Gamma/\hbar v_F$, $U_\pm = (\omega_1 \pm i\Gamma_1)$, $p = (4k^2_{yn} - U^2_-)^{1/2}$, and $Q_\pm = p \pm iU_-$.

For $\mathrm{Re}\sigma^{nd}_{yy}(i\omega)$ we follow the same procedure and from the sum over $n'(\neq n)$, cf. Eq. (82), we

keep only the dominant terms $n' = n \pm 1$. We then obtain

$$\begin{aligned} \mathrm{Re}\sigma_{yy}^{nd}(i\omega) &= \frac{e^2\hbar v_F}{h\pi^2}\sum_n \int_0^{k_m} dk_x \Bigg[\frac{(f_+^n - f_+^{n\pm1})D_+ - (f_-^n - f_-^{n\pm1})D_-}{\varepsilon_{k_x}^n - \varepsilon_{k_x}^{n\pm1}} \\ &+ \frac{(f_+^n - f_-^{n\pm1})D_+ - (f_-^n - f_+^{n\pm1})D_-}{\varepsilon_{k_x}^n + \varepsilon_{k_x}^{n\pm1}}\Bigg] \end{aligned} \tag{103}$$

and

$$\begin{aligned} \mathrm{Im}\sigma_{yy}^{nd}(i\omega) &= \frac{e^2\hbar v_F}{h\pi^2}\sum_n \int_0^{k_m} dk_x \Bigg[\frac{(f_+^n - f_+^{n\pm1})E_+ + (f_-^n - f_-^{n\pm1})E_-}{\varepsilon_{k_x}^n - \varepsilon_{k_x}^{n\pm1}} \\ &+ \frac{(f_+^n - f_-^{n\pm1})E_+ + (f_-^n - f_+^{n\pm1})E_-}{\varepsilon_{k_x}^n + \varepsilon_{k_x}^{n\pm1}}\Bigg], \end{aligned} \tag{104}$$

where $D_\pm = \Gamma((\hbar v_F\varepsilon_{k_x}^n - \hbar v_F\varepsilon_{k_x}^{n\pm1} \pm \hbar\omega)^2 + \Gamma^2)^{-1}$, and $E_\pm = (\hbar v_F\varepsilon_{k_x}^n + \hbar v_F\varepsilon_{k_x}^{n\pm1} \pm \hbar\omega)((\hbar v_F\varepsilon_{k_x}^n + \hbar v_F\varepsilon_{k_x}^{n\pm1} \pm \hbar\omega)^2 + \Gamma^2)^{-1}$ with $\varepsilon_{k_x}^n = (k_{yn}^2 + k_x^2)^{1/2}$. According to Eqs. (103) and (104), the absorption occurs between the valence band with index n and the conduction band with $n \pm 1$. The integrals over k_x in Eqs. (103) and (104) are not tractable and we evaluate them numerically.

In Fig. 6.9 we show $\mathrm{Re}\sigma_{xx}$ and $\mathrm{Re}\sigma_{yy}$ as functions of Ω for $\varepsilon_F = 0$ (upper panel) and $\varepsilon_F = 0.1$ (lower panel). The solid curves are for semiconducting nanoribbons ($dm = 4$) and the dotted ones for metallic ribbons ($dm = 5$). The optical selection rules ($n - n' = \Delta n$) allow subband index n to change by only 0 along the x (wire) direction. However, we have $\Delta n = \pm 1$ along the y (confinement) direction, but the amplitude of the peaks is small. Hereafter, we call the transitions satisfying $\Delta n = 0$ direct transitions and those satisfying $\Delta n = \pm 1$ indirect transitions. In addition, one needs to go from occupied to unoccupied states through the absorption of photons. The series of peaks corresponding to $\mathrm{Re}\sigma_{xx}$ and $\mathrm{Re}\sigma_{yy}$ occur at $\hbar\omega = -E_{-k_x}^n + E_{+k_x}^n$ and $\hbar\omega = -E_{-k_x}^n + E_{+k_x}^{n+1}$, respectively. These peaks correspond to the allowed interband transitions in the energy spectrum. The position of the absorption peaks follows the same order as indicated in Fig. 6.8. These results for AGNRs are similar to those in Ref. [269] apart from the contribution $\sigma_{\mu\mu}^d(i\omega)$ which is completely absent and only the real parts of the conductivities $\sigma_{\mu\mu}^{nd}(i\omega)$ are plotted.

In the upper panel of Fig. 6.9 in which Fermi level is in gap i.e., $\varepsilon_F = 0$, we can see that a Drude-type intraband transition is allowed in $\mathrm{Re}\sigma_{xx}$ for $dm = 5$ due to the nonvanshing v_x velocity

matrix elements with $\Delta n = 0$ [see Eq. (81) and transition D in Fig. 6.8]. On the other hand, we cannot see any type of intraband transitions in $\mathrm{Re}\sigma_{yy}$ because v_y the velocity matrix elements vansh as can be seen from Eq. (81). However, for $dm = 4$, only interband absorption transitions are allowed due to the Pauli exclusion principle in both $\mathrm{Re}\sigma_{xx}$ and $\mathrm{Re}\sigma_{yy}$. But, when we move the Fermi level to 0.1 [see the red dashed curve in Fig. 6.8], the absorption peak, say T_x^1, in $\mathrm{Re}\sigma_{xx}$ is suppressed due to the Pauli exclusion principle for $dm = 4$ in the range $0.017 \leqslant \Omega \leqslant 0.27$ whereas a absorption peak due to intraband transition (T_y^1) appears in $\mathrm{Re}\sigma_{yy}$ as can be seen in the lower panel of Fig. 6.9. Moreover, a Drude absorption peaks appear at low Ω in $\mathrm{Re}\sigma_{xx}$ for both $dm = 4$ and $dm = 5$. One note worthy feature is that resonance energies $E^n_{+k_x} - E^{n+1}_{-k_x}$ of indirect transitions are appeared between the $E^n_{+k_x} - E^n_{-k_x}$ that are the energies corresponding to absorption peaks of direct transitions.

We have plotted $\mathrm{Im}\sigma_{xx}$ and $\mathrm{Im}\sigma_{yy}$ versus the dimensionless photon energy (Ω) in Fig. 6.10. The absorption peaks in $\mathrm{Im}\sigma_{xx}$ have negative and positive values due to the negative sign between R_+ and R_- terms in Eq. (101), and the peaks corresponding to the transitions $-n \rightarrow n$ and $n \rightarrow -n$ have slightly different energies. This mismatch creates positive and negative peaks in the conductivity. However, the amplitude of the negative peaks is small as compared to that of the positive ones. This argument applies also to $\mathrm{Im}\sigma_{yy}$ [see Eq. (104)].

6.5 Summary and conclusion

We studied dc and ac transport in both metallic and semiconducting AGNRs. We derived analytical expressions for the diagonal and nondiagonal conductivities by employing linear response theory. We found that semiconducting to metallic transitions occur by changing the number of rows (dm) [see Fig. 6.3] in contrast to ordinary waveguides in which such transitions do not occur, see Fig. 6.4. In addition, the diagonal conductivity for scattering by screened Coulomb impurities was shown to depend approximately linearly on the carrier density and exhibits upward cusps when the Fermi level crosses the subbands. Further, we showed that the diagonal conductivity varies approximately linearly with the electron concentration in AGNRs, cf. Fig. 6.7.

Importantly, in all cases we showed that the scattering-dependent conductivity is described

quantitatively by a Drude-type contribution $\sigma^d_{xx}(i\omega)$ which, to our knowledge, was not previously reported or explicitly evaluated. We did show that this contribution dominates the response at very low frequencies at which the usual, scattering-independent contribution near vanishes.

Moreover, we obtained the optical selection rules $\Delta n = 0$ along the wire and $\Delta n = \pm 1$ along the confinement direction of AGNRs. We have demonstrated that the peak amplitude of the indirect transitions is suppressed contrary to that of the direct ones. Also, we showed that the absoption of low-energy photons is sensitive to the variation of the Fermi level, in contrast to monolayer WSe_2 [53], in which the spectral weight of the interband peaks is continuously redistributed into the intraband ones [see Fig. 6.9] similar to that of other 2D materials [161, 163] like graphene, silicene, $\alpha - T_3$, and topological insulators. A similar behaviour was found for the imaginary part of the conductivity. Furthermore, only intraband transitions occur in ordinary waveguides, cf. Fig. 6.6 (b) and Eq. (90), in contrast to AGNRs in which both intra- and inter-band transitions occur [see Figs. (6.9)-(6.10) and Eqs. (103)- (104)].

The details of the previous paragraphs could best be tested, we think, by optical experiments in AGNRs and by contrasting their results with those in unconfined graphene or other 2D materials and standard waveguides. The peak positions, that are sensitive to the dm-dependent energy gap between the subbands, cf. Eq. (3), could be tuned by a careful choice of dm in experiments performed in the far infrared (IR) range. This could lead to the development of new optical devices, in particular novel IR photodetectors based on photon absorption rather than on thermionic emission or tunnelling in arrays of GRNs proposed in Ref. [279]. Moreover, the scattering-dependent contribution $\sigma^d_{xx}(i\omega)$ to the power spectrum should be evident at very low frequencies at which the other conductivity contributions $\sigma^{nd}_{\mu\nu}(i\omega)$, as well as $\sigma^d_{yy}(i\omega)$ in our case, vanish ($\Gamma = 0$) or nearly so ($\Gamma \neq 0$) and $\sigma^d_{xx}(i\omega)$ dominates the spectrum, cf. Ref. [215]. We are not aware of any such experiments but hope that they will be carried out and also test the selection rules $\Delta n = 0$ and $\Delta n = \pm 1$ mentioned above.

6.6 Acknowledgments

M. Z. and P. V. acknowledge the support of the Concordia University Grant No. VB0038 and a Concordia University Graduate Fellowship.

Chapter 7

Conclusion and future directions

In chapter 2 we studied the effect of perpendicular electric (E_z) and magnetic (B) fields on the quantum magnetotransport of bilayer MoS_2. For $E_z, B = 0$, bands are spin and valley degenerate, while both spin and valley degeneracies are lifted in valence band for $E_z \neq 0$. However, there is no spin and valley splitting in the conduction band in the presence of perpendicular E_z. On the other hand, spin and valley degeneracies are fully lifted in conduction band for $E_z = 0$ and $B \neq 0$. Further, we found that strength of layer splitting and band gap can be controlled by the external parameter such as E_z. Spin and valley polarizations show beating behavior at low B while it is replaced by SdH oscillations at high B similar to monolayer MoS_2 [55] and the conventional 2DEG [146]. Moreover, we showed that the combined action of spin and valley Zeeman fields and interlayer splitting allow for inter LL transitions and lead to new quantum Hall plateaux. The field E_z modifies the layer splitting. As a result, steps of various heights, in multiples of e^2/h, occur in the Hall conductivity.

In chapter 3 we found that, when present, Δ and the SOI not only modify the band structure of bilayer WSe_2, but also significantly affect the spin- and valley-controlled magnetotransport in the presence and absence of electric E_z and magnetic B fields. We showed that the energy spectra for $B, E_z = 0$ and $B, E_z \neq 0$ no longer mirror each other. We point out that interband optical transitions, from level n in the valence band to level $n+1$ in the conduction band, no longer have the same energy as those from level $n+1$ to level n; this splits the corresponding absorption line in the real part of the longitudinal conductivity. The large values of Δ, λ_c and λ_v terms not only

force the conductivity peaks to vary linearly with B, but also guarantee the equidistant spacing between the Landau levels (LLs). A similar peak behavior was found in the imaginary part of the Hall conductivity. Also, we may expect that the values of Δ and SOI can be determined by carefully tuning the strength of E_z and B. Furthermore, the semiclassical limit of the magnetoconductivity is affected by the variation of B and Fermi energy E_F .

In chapter 4 we studied the effect of valley Zeeman and Rashba SOC on the energy dispersion of graphene/WSe_2 heterostructures as well as on the transport coefficients. We derived the effective Hamiltonian from the tight-binding (TB) model. We found that density of states shows finite values in both cases $\lambda \neq 0, \lambda_R = 0$ and $\lambda = 0, \lambda_R \neq 0$. While a square root singularity is found when both λ and λ_R are present. The presence of λ_R not only changes the sign of valley Hall conductivity, but also it enhances the gap between the bands. Also we found that effect of screening on diffusive conductivity dominates as long as $\lambda_R \neq 0$, while it is significantly suppressed for $\lambda \neq 0, \lambda_R = 0$. Further, a Drude response can be switched on and off with the variation of E_F. This behavior could be useful in technological applications.

In chapter 5 we investigated the influence of off-resonant circularly polarized light on the band structured of proximitized graphene as well as on the valley-dependent dc transport by employing the linear response formalism and Floquet theory. It was found that there is a transition from inverted band to direct one for $\Delta_\Omega > \Delta + \lambda_v$. In this band regime, spin and valley degeneracies are completely lifted. Further, we showed that valley polarization vanishes for $\Delta_\Omega < \Delta + \lambda_v$, while it get finite value for $\Delta_\Omega > \Delta + \lambda_v$. Moreover, we predicted that valley-Hall conductivity takes the quantized value $\sigma^v_{yx} = 2e^2/h$ in gap when $\Delta_\Omega < \Delta + \lambda_v$, while it vanishes for $\Delta_\Omega > \Delta + \lambda_v$. On the other hand, charge Hall conductivity has finite values when $\Delta_\Omega > \Delta + \lambda_v$, while it goes to zero in the opposite limit. In addition, valley and charge Hall conductivities does not switch sign unless the handedness of the light switches sign.

In chapter 6 we found a semiconductor-to-metal transition in AGNRs by changing the number of rows (dm), while there was no such transition in ordinary waveguides. In addition, we showed that the screened diagonal conductivity varies linearly with the carrier density and exhibits cusps when the Fermi level crosses the subbands. Further, we predicted different optical selection rules along the wire (x) and the direction of confinement (y) in AGNRs. Both inter- and intra-band

transitions occur in AGNRs whereas in ordinary waveguides only the intra-band one occurs. The amplitudes of the direct transition peaks are larger than those of the indirect ones. Moreover, we showed that the absorption of low-energy photons is sensitive to the variation of the Fermi level. Also, we found a similar behavior in the imaginary part of the conductivity.

In chapters 2-5 our focus was the study of multiple aspects of spin and valley transport in TMDCs such as MoS_2, WSe_2 as well as in graphene/TMDCs heterostructures. We predicted significant spin and valley splittings as well as topological transitions in their novel heterostructures in the presence and absence of externally applied perpendicular magnetic and electric fields. Moreover, we predicted a topological transition between different phases, e.g., the valley-Hall phase to the anomalous Hall one, in graphene/TMDCs heterostructure under an off-resonant light. Also, we pointed out a remarkable valley polarization, which can be switched on and off by controlling the intensity of the off-resonant light, in these heterostructures.

In chapter 6, we predicted a semiconductor-to-metal transition in AGNRs by changing the number of rows dm. Due to such peculiar behaviors, we expect that these materials could find novel uses in electronics, spintronics and valleytronics such as making IR photodectors, thermalassisted switching, valley valves, etc.

7.1 Future research plans

In the near future I plan to explore many-body phenomena in the above mentioned low dimensional systems. In more detail I plan to undertake the following subjects.

7.1.1 Spintronics and valleytronics based on magnetic 2D materials

Ferromagnetism, which by itself is an interesting correlation phenomenon, can also lead to great theoretical and technological potentials when combined with spintronics or valleytronics. One subject I would like to explore, which is timely and can be immediately rewarding, is the correlation among electronic structure, transport, and magnetic order in ferromagnets based on van der Waals heterostructures of novel graphene-like 2D materials such as in TMDCs, phosphorene, etc. The long-term goal of this research direction is to achieve a coherent understanding of spin and valley

degrees of freedom in magnetic 2D materials and hopefully to set the stage for a completely new paradigm of information processing beyond conventional semiconductor electronics.

7.1.2 Light-matter interaction and Floquet topological phases

Floquet lattice models as a marriage of optics and electronics is an active and exciting research direction. Therefore, my plan is to study different low-dimensional systems taking into account the effects of weak and strong light-matter interaction, and in particular to study many-body interactions in driven systems. As a start, I will try to contribute to understanding the physics of novel systems such as Floquet-Chern fractional insulators, flat bands, and generally symmetry-breaking phases in nonequilibrium states. This project belongs to the interdisciplinary area between optics, physics, and materials science.

Appendix A

Chapter 3

A.1 Zero-level Hall conductivity

Using Eq. (10), and Eq. (12) the off-diagonal velocity matrix elements for $n = 0$ are

$$\langle 0,\mu,s,\tau|\, v_x \,|n',\mu',s',\tau'\rangle = \tau v_F\, \varrho^{s,\tau}_{0,\mu}\varrho^{s',\tau'}_{n',\mu'}\delta_{s,s'} \times \left\{\sqrt{n'}/\varepsilon_{n,d_2'} + k^{s,\tau}_{0,\mu}k^{s',\tau'}_{n',\mu'}/\varepsilon_{0,d_4}\right\}\delta_{0,n'-1} \quad (105)$$

$$\langle n',\mu',s',\tau'|\, v_y \,|0,\mu,s,\tau\rangle = \tau i v_F\, \varrho^{s,\tau}_{0,\mu}\varrho^{s',\tau'}_{n',\mu'}\delta_{s,s'} \times \left\{\sqrt{n'}/\varepsilon_{n,d_2'} + k^{s,\tau}_{0,\mu}k^{s',\tau'}_{n',\mu'}/\varepsilon_{0,d_4}\right\}\delta_{0,n'-1} \quad (106)$$

$$\begin{aligned} \langle 0,+-,\tau|\, v_x \,|n',\mu',s',\tau'\rangle &= \tau v_F Y, \quad \langle n',\mu',s',\tau'|\, v_y \,|0,+-,\tau\rangle = \tau i v_F Y, \\ Y &= \varrho^{s',\tau'}_{n',\mu'}k^{s',\tau'}_{n',\mu'}\delta_{s,s'}\,\delta_{0,n'}. \end{aligned} \quad (107)$$

Using these expressions, the conductivities take the form

$$\begin{aligned} \begin{pmatrix} \mathrm{Re}\,\sigma^{nd}_{xx} \\ \\ \mathrm{Im}\,\sigma^{nd}_{xy} \end{pmatrix} &= \mp\frac{e^2}{2h}\sum_{s,\tau,\mu,\mu'}\eta^{s,\tau}_{0,1,\mu,\mu'}\left[\frac{1}{\left(\varepsilon^{s,\tau}_{0,\mu}-\varepsilon^{s,\tau}_{1,\mu}+\bar{\omega}\right)^2+\bar{\Gamma}^2} \pm \frac{1}{\left(\varepsilon^{s,\tau}_{0,\mu}-\varepsilon^{s,\tau}_{1,\mu}-\bar{\omega}\right)^2+\bar{\Gamma}^2}\right], \\ &= \mp\frac{e^2}{2h}\sum_{s,\tau,\mu'}\upsilon^{s,\tau}_{0,+-,\mu'}\left[\frac{1}{\left(\varepsilon^{s,\tau}_{0,+-}-\varepsilon^{s,\tau}_{0,\mu}+\bar{\omega}\right)^2+\bar{\Gamma}^2} \pm \frac{1}{\left(\varepsilon^{s,\tau}_{0,+-}-\varepsilon^{s,\tau}_{0,\mu}-\bar{\omega}\right)^2+\bar{\Gamma}^2}\right], \end{aligned} \quad (108)$$

where

$$\begin{aligned}
\eta^{s,\tau}_{0,1,\mu,\mu'} &= \bar{\Gamma}\big(\varrho^{s,\tau}_{0,\mu}\varrho^{s,\tau}_{1,\mu'}\big)^2\Big[\frac{1}{\varepsilon'_{1,d_2}}+\frac{k^{s,\tau}_{0,\mu}k^{s,\tau}_{1,\mu'}}{\varepsilon_{0,d_4}}\Big]^2\frac{f^{s,\tau}_{0,\mu}-f^{s,\tau}_{1,\mu'}}{\varepsilon^{s,\tau}_{0,\mu}-\varepsilon^{s,\tau}_{1,\mu'}},\\
\upsilon^{s,\tau}_{0,+-,\mu'} &= \bar{\Gamma}\big(\varrho^{s,\tau}_{0,\mu'}k^{s,\tau}_{0,\mu'}\big)^2\,\frac{f^{s,\tau}_{0,+-}-f^{s,\tau}_{0,\mu'}}{\varepsilon^{s,\tau}_{+-}-\varepsilon^{s,\tau}_{0,\mu'}}.
\end{aligned}\tag{109}$$

Appendix B

Chapter 4

B.1 Relaxation time

The relaxation time is generally a function of the incoming electron's wave vector and at low temperatures only states near the Fermi level will contribute to transport and single-particle properties. Below we provide expressions for the relaxation time at the Fermi energy in the limiting cases $\Delta, \lambda \neq 0, \lambda_R = 0$ and $\Delta, \lambda = 0, \lambda_R \neq 0$, because in these cases the summation over final states can be performed analytically. Within the first Born approximation the standard formula for the momentum relaxation time has the form

$$\frac{1}{\tau_\zeta} = \frac{1}{\tau^\eta_{\xi k}} = \frac{2\pi n_i}{\hbar} \sum_{\xi',\eta',k'} |\left\langle \xi, \eta, k \right| U(\mathbf{r}) \left| \xi', \eta', k' \right\rangle|^2 \delta(E_{\xi k} - E_{\xi' k'})(1 - \cos\theta), \tag{110}$$

where $U(\mathbf{r})$ is the impurity potential, n_i the impurity density, and θ the angle between the initial k and final k' wave vectors. Equation (110) holds only for elastic scattering ($\xi = \xi', \eta = \eta', k = k'$) and for central potentials $U(\mathbf{r})$ i.e. $U(\mathbf{r}) = U(r)$. The results for two types of impurity potentials are as follows.

Short-range impurities. We have $U(\mathbf{r}) = U_0 \delta(\mathbf{r} - \mathbf{r_i})$ where $\mathbf{r}$ and $\mathbf{r_i}$ are the position vectors of the electron and impurity, respectively, and U_0 is the strength of potential. In this case $U(\mathbf{q}) = U_0$ is the Fourier transform of $U(\mathbf{r}) = (1/\sqrt{L_x L_y}) \sum_q U(q) e^{i\mathbf{q}.\mathbf{r}}$ with $|\mathbf{q}| = 2k \sin(\theta/2)$. The results are:

i) $\lambda_R = 0$

$$\frac{1}{\tau^{\eta}_{sk_F}} = \frac{V_0^2 n_i (N_s^{\eta})^4}{\hbar} \frac{\sqrt{\Delta^2 + (\hbar v_F k)^2}}{(\hbar v_F)^2} \left[(A_s^{\eta})^4 - (A_s^{\eta})^2 + 1 \right]. \tag{111}$$

In the limit $\Delta, \lambda = 0$, the above result reduces to graphene's scattering time Eq. (24) of Ref. [218]

$$\frac{1}{\tau_{k_F}} = \frac{V_0^2 n_i k}{4\hbar^2 v_F}. \tag{112}$$

Also, for $\lambda = 0$ Eq. (111) agrees with the result for topological insulators [215].

ii) $\Delta, \lambda = 0$

$$\begin{aligned} \frac{1}{\tau^{\eta}_{sk_F}} = & \frac{V_0^2 n_i (N_s^{\eta})^4 \sqrt{\lambda_R^2 + (\hbar v_F k)^2}}{\hbar^3 v_F^2} \Big[[(A_s^{\eta})^2 + (B_s^{\eta})^2]^2 + (C_s^{\eta})^4 - [1 + (C_s^{\eta})^2] \\ & [(A_s^{\eta})^2 + (B_s^{\eta})^2] - 2(C_s^{\eta})^2 + 1 \Big]. \end{aligned} \tag{113}$$

Long-range impurities. We assume $U(\mathbf{r}) = eQe^{-k_s r}/4\pi\epsilon_0\epsilon r$, where k_s is the screening wave vector, Q is the charge of the impurity, and ϵ the dielectric constant. In this case $U(q) = 2\pi U_0/\sqrt{k_s^2 + q^2}$ with $U_0 = eQ/4\pi\epsilon_0\epsilon$. The results are:

i) $\lambda_R = 0$

$$\begin{aligned} \frac{1}{\tau^{\eta}_{sk_F}} = & \frac{V_0^2 n_i (N_s^{\eta})^4 \sqrt{\Delta^2 + (\hbar v_F k)^2}}{2\hbar^3 v_F^2 k^2} \Big[[1 + (A_s^{\eta})^4] [1 - \frac{a_s}{\sqrt{a_s^2 + 1}}] + 2(A_s^{\eta})^2 \\ & [2a_s^2 - \frac{a_s(2a_s^2 + 1)}{\sqrt{a_s^2 + 1}}] \Big]. \end{aligned} \tag{114}$$

In the limit $\Delta = \lambda = 0$ we set $a_s = k_s/2k$ and obtain the relaxation time in pristine graphene [220]

$$\frac{1}{\tau_{k_F}} = \frac{V_0^2 n_i \, (a_s - \sqrt{a_s^2 + 1})^2}{4\hbar^2 v_F k}. \tag{115}$$

Moreover, for $\lambda = 0$ Eq. (114) gives the relaxation time for topological insulators [215].

ii) $\Delta, \lambda = 0$

$$\frac{1}{\tau^{\eta}_{sk_F}} = \frac{V_0^2 n_i (N_s^{\eta})^4 \sqrt{\lambda_R^2 + (\hbar v_F k)^2}}{2\hbar^3 v_F^2 k^2} \Big[1 + [(A_s^{\eta})^2 + (B_s^{\eta})^2]^2 + (C_s^{\eta})^4 [1 - \frac{a_s}{\sqrt{a_s^2+1}}]$$
$$+2[1 + (C_s^{\eta})^2][A_s^{\eta})^2 + (B_s^{\eta})^2]\big[2a_s^2 - \frac{a_s(2a_s^2+1)}{\sqrt{a_s^2+1}}]$$
$$-2(C_s^{\eta})^2\big[1 + \frac{a_s}{\sqrt{a_s^2+1}} + 8a_s^3\sqrt{a_s^2+1} - 8a_s^2(2a_s^2+1)\big]\Big]. \quad (116)$$

Appendix C

Chapter 6

C.1 Relaxation time

Within the first Born approximation, the standard formula for relaxation time takes the form

$$\frac{1}{\tau_\zeta} = \frac{1}{\tau^n_{\eta k_x}} = \frac{2\pi n_i}{\hbar L_x} \sum_{n',\eta',k'_x} |\langle n,\eta,k_x| U_x |n',\eta',k'_x\rangle|^2 \delta(E^n_{\eta k_x} - E^{n'}_{\eta' k'_x})(1-\cos\theta), \quad (117)$$

where $U_x = U(x)$ is the impurity potential, n_i the impurity density, and θ the angle between the initial (k_{yn}, k_x) and final (k'_{yn}, k'_x) wave vectors. Equation (117) holds only for the elastic scattering. The results for two types of impurity potentials are as follows.

Long-range impurities: For screened, Coulomb-type impurities we consider the model potential [278]

$$U_x = U_0 e^{-k_s|x|}/\sqrt{|x|}, \quad (118)$$

where $U_0 = 2\pi e^2\sqrt{c}/\epsilon_0\epsilon_r$, k_s is the screening wave vector, ϵ_0 the free space permittivity, ϵ_r the static dielectric constant, and c is the constant of order 1 in units of inverse length. In this case, we write $U_x = \sum_{q_x} U_{q_x} e^{iq_x x}$ with $U_{q_x} = U_0\{[k_s + \sqrt{k_s^2+q_x^2}]/(k_s^2+q_x^2)\}^{1/2}$ the Fourier transform of U_x. We obtain

$$|\langle n,\eta,k_x| e^{iq_x x} |n',\eta',k'_x\rangle|^2 = |\eta\eta' + e^{-i\varphi}|^2 |U_{q_x}|^2 \delta_{n,n'}\delta_{k'_x+q_x,k_x}, \quad (119)$$

with $q_x = k_x - k'_x$ and $\varphi = \theta_{k_{yn},k_x} - \theta_{k'_{yn},k'_x}$. The integration over q_x is straightforward. That over k'_x is carried out using the properties of the δ function and only the root $k'_x = -k_x$ of the equation $E^n_{\eta k_x} - E^{n'}_{\eta' k'_x} = 0$ contributes to the integral. For simplicity we also take $\varphi \approx 0$ and use $\theta \approx \pi$. With k_x evaluated at the Fermi level the final result is

$$\frac{1}{\tau_F} = \frac{n_i U_0^2}{2\hbar^2 v_F} \frac{\sqrt{k_{yn}^2 + |k_F|^2}\,(k_s + k_{sF})}{|k_F|\, k_{sF}^2}, \tag{120}$$

where $k_{sF}^2 = k_s^2 + 4|k_F|^2$. The term k_{yn} in Eq. (120) denotes the Fermi wave vector for the nth subband. In the limit $k_{yn} = 0$ Eq. (120) becomes

$$\frac{1}{\tau_F} = \frac{n_i U_0^2}{2\hbar^2 v_F} \frac{k_s + k_{sF}}{k_{sF}^2}. \tag{121}$$

Further, for $k_s \gg k_F$, Eq. (121) reduces to

$$\frac{1}{\tau_F} = \frac{n_i U_s^2}{\hbar^2 v_F k_s}. \tag{122}$$

Short-range impurities: we have $U(x) = U_0 \delta(x - x_i)$ with U_0 the constant strength of potential and x_i the position of the impurity. In this case, the matrix element becomes $|\langle n, \eta, k_x| U_x |n', \eta', k'_x\rangle|^2 = U_0^2$. This leads to

$$\frac{1}{\tau_F} = \frac{2 n_i U_0^2}{\pi \hbar^2 v_F} \frac{\sqrt{k_{yn}^2 + |k_F|^2}}{|k_F|}. \tag{123}$$

For $k_{yn} = 0$ Eq. (123) reduces to

$$\frac{1}{\tau_F} = \frac{2 n_i U_0^2}{\pi \hbar^2 v_F}. \tag{124}$$

Bibliography

[1] P. R. Wallace, Phys. Rev. **71**, 622 (1947).

[2] H. P. Boehm, A. Clauss, G. O. Fischer, and U. Hofmann, Z. Naturforsch **17**, 150 (1962).

[3] J. W. May, Surf. Sci. **17**, 267 (1969).

[4] K. S. Novoselov, A. K. Geim, S. V. Morozov, D. Jiang, Y. Zhang, S. V. Dubonos, I. V.Grigorieva, and A. A. Firsov, Science **306**, 666 (2004).

[5] The official website of the Nobel prize (www.nobelprize.org).

[6] K. S. Novoselov, A. K. Geim, S. V. Morozov, D. Jiang, M. I. Katsnelson, I. V. Grigorieva, S. V. Dubonos, and A. A. Firsov, Nature **438**, 197 (2005).

[7] Y. Zhang, Y.-W. Tan, H. L. Stormer, and P. Kim, Nature **438**, 201 (2005).

[8] X. Du, I. Skachko, F. Duerr, A. Luican, and E. Y. Andrei, Nature **462**, 192 (2009).

[9] K. I. Bolotin, K. J. Sikes, Z. Jiang, M. Klima, G. Fudenberg, J. Hone, P. Kim, and H.L.Stormer, Solid State Commun. **146**, 351 (2008).

[10] ISI web of knowledge service (www.wokinfo.com).

[11] S. Dresselhaus and H. Aoki, Physics of graphene (Nanoscience and Technology) (2014).

[12] M. Liu, X. B. Yin, E. Ulin-Avila, B. S. Geng, T. Zentgraf, L. Lu, F. Wang, and X. Zhang, Nature **474** , 64 (2011).

[13] S. K. Kim, Y. Zhao, H. Jang, S. Y. Lee, J. M. Kim, K. S. Kim, J. Y. Ahn, P. Kim, J. Y. Choi, and B. H. Hong, Nature **457**, 706 (2009).

[14] Y. W. Zhu, S. Murali, M. D. Stoller, K. J. Ganesh, W. W. Cai, P. J. Ferreira, A. Pirkle, R. M. Wallace, K. A. Cychosz, M. Thommes, D. Su, E. A. Stach, and R. S. Ruoff, Science **332**, 1537 (2011).

[15] M. F. El-Kady, V. Strong, S. Dubin, and R. B. Kaner, Science **335**, 6074 (2012).

[16] X. Yang, M. S. Xu, W. M. Qiu, X. Q. Chen, M. Deng, J. L. Zhang, H. Iwai, E. Watanabe, and H. Z. Chen, J. Mater. Chem. **21**, 8096 (2011).

[17] A. Geim, K. S. Novoselov, Nat. Mater. **6**, 183 (2007).

[18] M. Deng, X. Yang, M. Silke, W. M. Qiu, M. S. Xu, G. Borghs, and H. Z. Chen, Sensors Actuators B: Chem. **158**, 176 (2011).

[19] M. Xu, D. Fujita, and N. Hanagata, Small **5**, 2638 (2009).

[20] S. Garaj, W. Hubbard, A. Reina, J. Kong, D. Branton and J. A. Golovchenko, Nature **467**, 190 (2010).

[21] M. S. Xu, Y. Gao, X. Yang, and H. Z. Chen, Chin. Sci. Bull. **57**, 3000 (2012).

[22] Y.-M. Lin, C. Dimitrakopoulos, K. A. Jenkins, D. B. Farmer, H.-Y. Chiu, A. Grill, and P. Avouris, Science **327**, 662 (2010).

[23] M. I. Katsnelson, Materials Today **10**, 20 (Jan-Feb. 2007).

[24] M. P. Ramuz, M. Vosgueritchian, P. Wei, Ch. Wang, Y. Gao, Y. Wu, Y. Chen, and Zh. Bao, ACS Nano. **6**, 10384 (2012).

[25] F. Bonaccorso, Z. Sun, T. Hasan, and A. C. Ferrari, Nat. Photon. **4**, 611 (2010).

[26] S. Bae, H. Kim, Y. Lee, X. Xu, J. S. Park, Y. Zheng, J. Balakrishnan, T. Lei, H. R.Kim, Y. I. Song, Y. J. Kim, K. S. Kim, B. Ozyilmaz, J. H. Ahn, B. H. Hong, and S. Iijima, Nat. Nanotech. **5**, 574 (2010).

[27] C. R. Dean, A. F. Young, I. Meric, C. Lee, L. Wang, S. Sorgenfrei, K. Watanabe, T.Taniguchi, P. Kim, K. L. Shepard, and J.Hone, Nat. Nanotech. **5**, 722 (2010).

[28] K. I. Bolotin, K. J. Sikes, J. Hone, H. L. Stormer, and P. Kim, Phys. Rev. Lett. **101**, 096802 (2008).

[29] X. Du, I. Skachko, A. Barker, and E. Y. Andrei, Nat. Nanotech. **3**, 491 (2008).

[30] F. Schwierz, Nature Nanotech. **5**, 487 (2010).

[31] Y. Kimura, T. Wakabayashi, K. Okada, T. Wada, and H. Nishikawa, Wear **232**, 199 (1999).

[32] Y. Kubota, K. Watanabe, O. Tsuda, and T. Taniguchi, Science **317**, 932 (2007).

[33] L. Britnell, R. V. Gorbachev, R. Jalil, B. D. Belle, F. Schedin, M. I. Katsnelson, L. Eaves, S. V. Morozov, A. S. Mayorov, N. M. R. Peres, A. H. C. Neto, J. Leist, A. K. Geim, L. A. Ponomarenko, and K. S. Novoselov, Nano Lett. **12**, 1707 (2012).

[34] N. R. Jungwirth and G. D. Fuchs, Phys. Rev. Lett. **119**, 057401 (2017).

[35] G. G. Guzm´an-Verri and L. C. Lew Yan Voon, Phys. Rev. B **76**, 075131 (2007); S. Lebégue and O. Eriksson, *ibid.* **79**, 115409 (2009).

[36] P. Vogt, P. De Padova, C. Quaresima, J. Avila, E. Frantzeskakis, M. C. Asensio, A. Resta, B. Ealet, and G. Le Lay, Phys. Rev. Lett. **108**, 155501 (2012); A. Fleurence, R. Friedlein, T. Ozaki, H. Kawai,Y. Wang, and Y. Yamada-Takamura, *ibid.* **108**, 245501 (2012).

[37] D.Chiappe, E. Scalise, E. Cinquanta, C. Grazianetti, B. V. Broek, M. Fanciulli, M. Houssa, and A. Molle, Adv. Mater. **26**, 2096 (2014).

[38] Z. Ni, Q. Liu, K. Tang, J. Zheng, J. Zhou, Rui Qin, Z. Gao, D. Yu, and Jing Lu, Nano Lett. **12**, 113 (2012); L. Chen, H. Li, B. Feng, Z. Ding, J. Qiu, P. Cheng, K. Wu, and S. Meng, Phys. Rev. Lett. **110**, 085504 (2013); M. Neek-Amal, A. Sadeghi, G. R. Berdiyorov, and F. M. Peeters, Appl. Phys. Lett. **103**, 261904 (2013).

[39] C.-C. Liu, W. Feng, and Y. Yao, Phys. Rev. Lett. **107**, 076802 (2011); X.-L. Zhang, L.-F. Liu, and W.-M. Liu, Sci. Rep. **3**, 2908 (2013); M. Tahir, A. Manchon, K. Sabeeh, and U. Schwingenschlögl, Appl. Phys. Lett. **102**, 162412 (2013).

[40] M. Ezawa, Phys. Rev. Lett. **109**, 055502 (2012).

[41] A. Kara, H. Enriquez, A. P. Seitsonen, L. C. Lew Yan Voon, S. Vizzini, B. Aufray, and H. Oughaddoub, Surf. Sci. **67**, 1 (2012).

[42] X. Zhai and G. Jin, Condens. Matt. **26**, 015304 (2014).

[43] Z. Y. Zhu, Y. C. Cheng and U. Schwingenschlögl, Phys. Rev. B **84**, 153402 (2011).

[44] K. F. Mak, C. Lee, J. Hone, J. Shan, and T. F. Heinz, Phys. Rev. Lett. **105**, 136805 (2010).

[45] A. Splendiani, L. Sun, Y. B. Zhang, T. S. Li, J. Kim, C. Y. Chim, G. Galli, and F. Wang, Nano Lett. **10**, 1271 (2010).

[46] A. Kuc, N. Zibouche, and T. Heine, Phys. Rev. B **83**, 245213 (2011).

[47] L. Sun, J. Yan, D. Zhan, L. Liu, H. Hu, H. Li, B. K. Tay, J.-L. Kuo, C.-C. Huang, D. W. Hewak, P. S. Lee, and Z. X. Shen, Phys. Rev. Lett. **111**, 126801 (2013).

[48] B. Radisavljevic, A. Radenovic, J. Brivio, V. Giacometti, and A. Kis, Nature Nanotech. **6**, 147 (2011).

[49] H. Wang, L. Yu, Y.-H. Lee, Y. Shi, A. Hsu, M. L. Chin, L.-J. Li, M. Dubey, J. G. Kong, and T. Palacios, Nano Lett. **12**, 4674 (2012).

[50] O. Lopez-Sanchez, D. Lembke, M. Kayci, A. Radenovic, and A. Kis, Nat. Nanotechnol. **8**, 497 (2013).

[51] B. Radisavljevic, M. B. Whitwick, and A. Kis, Appl. Phys. Lett. **101**, 043103 (2012).

[52] X. Zhou, Y. Liu, M. Zhou, H. H. Shao, and G. H. Zhou, Appl. Phys. Express **7**, 021201 (2014).

[53] M. Tahir and P. Vasilopoulos, Phys. Rev. B **94**, 045415 (2016).

[54] X. Zhou, Y. Liu, M. Zhou, D. Tang, and G. Zhou, J. Phys.: Condens. Matt. **26**, 485008 (2014).

[55] M. Tahir, P. Vasilopoulos, and F. M. Peeters, Phys. Rev. B **93**, 035406 (2016).

[56] A. Kormányos, P. Rakyta, and G. Burkard, New J. Phys. **17**, 103006 (2015).

[57] X. Cui, G.-H. Lee, Y. D. Kim, G. Arefe, P. Y. Huang, C.-H. Lee, D. A. Chenet, X. Zhang, L. Wang, F. Ye, F. Pizzocchero, B. S. Jessen, K. Watanabe, T. Taniguchi, D. A. Muller, T. Low, P. Kim, and J. Hone, Nat. Nanotechnol. **10**, 534 (2015).

[58] M. Tahir, Physica E (Amsterdam) **97**, 184 (2018).

[59] D. Xiao, G.-B. Liu, W. Feng, X. Xu and W. Yao, Phys. Rev. Lett. **108**, 196802 (2012).

[60] K. F. Mak, K. He, J. Shan and T. F. Heinz, Nature Nanotech. **7**, 494 (2012).

[61] T. Cao, G. Wang, W. Han, H. Ye, C. Zhu, J. Shi, Q. Niu, P. Tan, E. Wang, B. Liu and J. Feng, Nature Commun. **3**, 887 (2012).

[62] M. Yankowitz, J. Xue, D. Cormode, J. D. S.-Yamagishi, K. Watanabe, T. Taniguchi, P. J.-Herrero, P. Jacquod and B. J. LeRoy, Nat. Phys. **8**, 382 (2012).

[63] L. A. Ponomarenko, R. V. Gorbachev, G. L. Yu, D. C. Elias, R. Jalil, A. A. Patel, A. Mishchenko, A. S. Mayorov, C. R. Woods, J. R. Wallbank, M. M.-Kruczynski, B. A. Piot, M. Potemski, I. V. Grigorieva, K. S. Novoselov, F. Guinea, V. I. Fal'ko and A. K. Geim, Nature **497**, 594 (2013).

[64] C. R. Dean, L. Wang, P. Maher, C. Forsythe, F. Ghahari, Y. Gao, J. Katoch, M. Ishigami, P. Moon, M. Koshino, T. Taniguchi, K. Watanabe, K. L. Shepard, J. Hone and P. Kim, Nature **497**, 598 (2013).

[65] B. Hunt, J. D. S.-Yamagishi1, A. F. Young1, M. Yankowitz, B. J. LeRoy, K. Watanabe, T. Taniguchi, P. Moon, M. Koshino, P. J.-Herrero1 and R. C. Ashoori, Science **340**, 1427 (2013).

[66] G. L. Yu, R. V. Gorbachev, J. S. Tu, A. V. Kretinin, Y. Cao, R. Jalil, F. Withers, L. A. Ponomarenko, B. A. Piot, M. Potemski, D. C. Elias, X. Chen, K. Watanabe, T. Taniguchi, I. V.

Grigorieva, K. S. Novoselov, V. I. Fal'ko, A. K. Geim and A. Mishchenko, Nat. Phys. **10**, 525 (2014).

[67] J. R. Wallbank, A. A. Patel, M. Mucha-Kruczynski, A. K. Geim, and V. I. Falko, Phys. Rev. B **87**, 245408 (2013).

[68] A. N. Grigorenko, M. Polini, and K. S. Novoselov, Nat. Photonics **6**, 749 (2012).

[69] S. Dai1, Z. Fei1, Q. Ma, A. S. Rodin, M. Wagner, A. S. McLeod, M. K. Liu, W. Gannett, W. Regan, K. Watanabe, T. Taniguchi, M. Thiemens, G. Dominguez, A. H. Castro Neto, A. Zettl, F. Keilmann, P. J.-Herrero, M. M. Fogler, and D. N. Basov, Science **343**, 1125(2014).

[70] A. Woessner, M. B. Lundeberg, Y. Gao, A. Principi, P. A.-González, M. Carrega, K. Watanabe, T. Taniguchi, G. Vignale, M. Polini, J. Hone, R. Hillenbrand, and F. H. L. Koppens, Nat. Mater. **14**, 421 (2015).

[71] K. Zhang, F. L. Yap, K. Li, C. T. Ng, L. J. Li, and K. P. Loh, Adv. Funct. Mater. **24**, 731 (2014).

[72] S. Dai, Q. Ma, M. K. Liu, T. Andersen, Z. Fei, M. D. Goldflam, M. Wagner, K. Watanabe, T. Taniguchi, M. Thiemens, F. Keilmann, G. C. A. M. Janssen, S-E. Zhu, P. J.-Herrero, M. M. Fogler, and D. N. Basov, Nat. Nanotechnol. **10**, 682 (2015).

[73] V. W. Brar, M. S. Jang, M. Sherrott, S. Kim, J. J. Lopez, L. B. Kim, M. Choi, and H. Atwater, Nano. Lett. **14**, 3876 (2014).

[74] A. Tomadin, F. Guinea, and M. Polini, Phys. Rev. B **90**, 161406 (2014).

[75] G.-H. Lee, Y.-J. Yu, C. Lee, C. Dean, K. L. Shepard, P. Kim, and J. Hone, Appl. Phys. Lett. **99**, 243114 (2011).

[76] L. Britnel, R. V. Gorbachev, R. Jalil, B. D. Belle, F. Schedin, A. Mishchenko, T. Georgiou, M. I. Katsnelson, L. Eaves, S. V. Morozov, N. M. R. Peres, J. Leist, A. K. Geim1, K. S. Novoselov, and L. A. Ponomarenko, Science **335**, 947 (2012).

[77] T. Georgiou, R. Jalil, B. D. Belle, L. Britnell, R. V. Gorbachev, S. V. Morozov, Y.-J. Kim, A. Gholinia, S. J. Haigh, O. Makarovsky, L. Eaves, L. A. Ponomarenko, A. K. Geim, K. S. Novoselov, and A. Mishchenko, Nat. Nanotechnol. **8**, 100 (2013).

[78] M. S. Choi, G.-H. Lee, Y.-J. Yu, D.-Y. Lee, S. H. Lee, P. Kim, J. Hone, and W. J. Yoo, Nat. Commun. **4**, 1624 (2013).

[79] H. Yang, J. Heo, S. Park, H. J. Song, D. H. Seo, K.-E. Byun, P. Kim, I. Yoo, H.-J. Chung, and K. Kim, Science **336**, 1140 (2012).

[80] A. Mishchenko, J. S. Tu, Y. Cao, R. V. Gorbachev, J. R. Wallbank, M. T. Greenaway, V. E. Morozov, S. V. Morozov, M. J. Zhu, S. L. Wong, F. Withers, C. R. Woods, Y-J. Kim, K. Watanabe, T. Taniguchi, E. E. Vdovin, O. Makarovsky, T. M. Fromhold, V. I. Fal'ko, A. K. Geim, L. Eaves, and K. S. Novoselov, Nat. Nanotechnol. **9**, 808 (2014).

[81] Y.-C. Lin, R. K. Ghosh, R. Addou, N. Lu, S. M. Eichfeld, H. Zhu, M.-Y. Li, X. Peng, M. J. Kim, L.-J. Li, R. M. Wallace, S. Datta, and J. A. Robinson, Nat. Commun. **6**, 7311 (2015).

[82] K. Roy, M. Padmanabhan, S. Goswami, T. P. Sai, G. Ramalingam, S. Raghavan, and A. Ghosh, Nat. Nanotechnol. **8**, 826 (2013).

[83] H. Fang, C. Battaglia, C. Carraro, S. Nemsak, B. Ozdol, J. S. Kang, H. A. Bechtel, S. B. Desai, F. Kronast, A. A. Unal, G. Conti, C. Conlon, G. K. Palsson, M. C. Martin, A. M. Minor, C. S. Fadley, E. Yablonovitch, R. Maboudian, and A. Javey, Proc. Natl. Acad. Sci. U.S.A. **111**, 6198 (2014).

[84] P. Rivera, J. R. Schaibley, A. M. Jones, J. S. Ross, S. Wu, G. Aivazian, P. Klement, K. Seyler, G. Clark, N. J. Ghimire, J. Yan, D. G. Mandrus, W. Yao, and X. Xu , Nat. Commun. **6**, 6242 (2015).

[85] L. Britnell, R. M. Ribeiro, A. Eckmann, R. Jalil, B. D. Belle, A. Mishchenko, Y.-J. Kim, R. V. Gorbachev, T. Georgiou, S. V. Morozov, A. N. Grigorenko, A. K. Geim, C. Casiraghi, A. H. Castro Neto, and K. S. Novoselov, Science **340**, 1311 (2013).

[86] G. W. Mudd, S. A. Svatek, L. Hague, O. Makarovsky, Z. R. Kudrynskyi, C. J. Mellor, P. H. Beton, L. Eaves, K. S. Novoselov, Z. D. Kovalyuk, E. E. Vdovin, A. J. Marsden , N. R. Wilson, and A. Patané, Adv. Mater. **27**, 3760 (2015).

[87] Y. Deng, Z. Luo, N. J. Conrad, H. Liu, Y. Gong, S. Najmaei, P. M. Ajayan, J. Lou, X. Xu, and P. D. Ye, ACS Nano **8**, 8292 (2014).

[88] F. Withers, O. D. P.-Zamudio, A. Mishchenko, A. P. Rooney, A. Gholinia, K. Watanabe, T. Taniguchi, S. J. Haigh, A. K. Geim, A. I. Tartakovskii, and K. S. Novoselov, Nat. Mater. **14**, 301 (2015).

[89] F. Withers, O. Del P.-Zamudio, S. Schwarz, S. Dufferwiel, P. M. Walker, T. Godde, A. P. Rooney, A. Gholinia, C. R. Woods, P. Blake, S. J. Haigh, K. Watanabe, T. Taniguchi, I. L. Aleiner, A. K. Geim, V. I. Fal'ko, A. I. Tartakovskii, and K. S. Novoselov, Nano Lett. **15**, 8223 (2015).

[90] D. Pacilé, J. C. Meyer, Ç. Ö. Girit, and A. Zettl, Appl. Phys. Lett. **82**, 133107 (2015).

[91] J. N. Coleman, M. Lotya, A. O'Neill, S. D. Bergin, P. J. King, U. Khan, K. Young, A. Gaucher, S. De, R. J. Smith, I. V. Shvets, S. K. Arora, G. Stanton, H. Y. Kim, K. Lee, G. T. Kim, G. S. Duesberg, T. Hallam, J. J. Boland, J. J. Wang, J. F. Donegan, J. C. Grunlan, G. Moriarty, A. Shmeliov, R. J. Nicholls, J. M. Perkins, E. M. Grieveson, K. Theuwissen, D. W. McComb, P. D. Nellist, and V. Nicolosi, Science **331**, 568 (2011).

[92] R. J. Smith, P. J. King, M. Lotya, C. Wirtz, U. Khan, S. De, A. O'Neill, G. S. Duesberg, J. C. Grunlan, G. Moriarty, J. Chen, J. Z. Wang, A. I. Minett, V.Nicolosi, and J. N. Coleman, Adv. Mater. **23**, 3944 (2011).

[93] K. G. Zhou, N. N. Mao, H. X. Wang, Y. Peng, and H. L. Zhang, Angew. Chem. Int. Ed. **50**, 10839 (2011).

[94] M. F. El-Kady, V. Strong, S. Dubin, and R. B. Kaner, Science **335**, 6074 (2012).

[95] G. X. Ni, Y. Zheng, S. Bae, C. Y. Tan, O. Kahya, J. Wu, B. H. Hong, K. Yao, and B. Ozyilmaz, ACS Nano **6**, 3935 (2012).

[96] Y. Wang, Z. X. Shi, and J. J. Yin, Mater. Chem. **21**, 11371 (2011).

[97] A. Nag, K. Raidongia, K. P. S. S. Hembram, R. Datta, U. V. Waghmare, and C. N. R. Rao, ACS Nano, **4**, 1539 (2010).

[98] X. S. Li, W. W. Cai, J. An, S. Kim, J. Nah, D. X. Yang, R. Piner, A. Velamakanni, I. Jung, E. Tutuc, S. K. Banerjee, L. Colombo, and R. S. Ruoff, Science **324**, 1312 (2009).

[99] T. Hesjedal, Appl. Phys. Lett. **98**, 133106 (2011).

[100] M. S. Xu, D. Fujita, K. Sagisaka, E. Watanabe, and N. Hanagata, ACS Nano **5**, 1522 (2011).

[101] D. Fujita and K. Yoshihara, J. Vac. Sci. Technol. A **12**, 2134 (1994).

[102] D. Fujita and T. Homma, J. Vac. Sci. Technol. A **6**, 230 (1988).

[103] A. Ayari, E. Cobas, O. Ogundadegbe, and M. S. Fuhrer, J. Appl. Phys. **101**, 014507 (2007).

[104] F. Rose, M. O. Goerbig, and F. Piechon, Phys. Rev. B **88**, 125438 (2013).

[105] R.-L. Chu, X. Li, S. Wu, Q. Niu, W. Yao, X. Xu, and C. Zhang, Phys. Rev. B **90**, 045427 (2014).

[106] Y.-H. Ho, Y.-H. Wang, and H.-Y. Chen, Phys. Rev. B **89**, 155316 (2014).

[107] X. Li, F. Zhang, and Q. Niu, Phys. Rev. Lett. **110**, 066803 (2013).

[108] Q. Liu, L. Li, Y. Li, Z. Gao, Z. Chen, and J. Lu, J. Phys. Chem. C **116**, 21556 (2012).

[109] A. Ramasubramaniam, D. Naveh, and E. Towe, Phys. Rev. B **84**, 205325 (2011).

[110] N. Zibouche, P. Philipsen, A. Kuc, and T. Heine, Phys. Rev. B **90**, 125440 (2014).

[111] Z. Gong, G.-B. Liu, H. Yu, D. Xiao, X. Cui, X. Xu, and Wang Yao, Nat. Commu. **4**, 15 (2013).

[112] S. Wu, J. S. Ross, G. B. Liu, G. Aivazian, A. Jones, Z. Fei, W. Zhu, D. Xiao, W. Yao, D. Cobden, and X. Xu, Nat. Phys. **9**, 149 (2013).

[113] J. Lee, K. F. Mak, and J. Shan, Nat. Nanotech. **11**, 421 (2016).

[114] A. T. Neal, H. Liu, J. J. Gu, and P. D. Ye, ACS Nano **7**, 7077 (2013).

[115] F. Guinea, New J. Phys. **12**, 083063 (2010).

[116] F. Mireles and J. Schliemann, New J. Phys. **14**, 093026 (2012).

[117] J. Milton Pereira, Jr., F. M. Peeters, and P. Vasilopoulos, Phys. Rev. B **76**, 115419 (2007).

[118] M. Zarenia, P. Vasilopoulos, and F. M. Peeters, Phys. Rev. B **85**, 245426 (2012).

[119] M. Nakamura, L. Hirasawa, and K. I. Imura, Phys. Rev. B **78**, 033403 (2008).

[120] K. Lee, S. Kim, M. S. Points, T. E. Beechem, T. Ohta, and E. Tutuc, Nano Lett. **11**, 3624 (2011).

[121] M. A. Hidalgo, and R. Cangas, arXiv: 1602.02631.

[122] K. S. Novoselov, E. McCann, S. V. Morozov, V. I. Falko, M. I. Katsnelson, U. Zeitler, D. Jiang, F. Schedin, and A. K. Geim, Nat. Phys. **2**, 177 (2006).

[123] C. R. Dean, A. F. Young, I. Meric, C. Lee, L. Wang, S. Sorgenfrei, K. Watanabe, T. Taniguchi, P. Kim, K. L. Shepard, and J. Hone, Nat. Nanotech. **5**, 722726 (2010).

[124] E. McCann, Phys. Rev. B **74**, 161403 (2006).

[125] Y. Zhang, T.-T. Tang, C. Girit, Z. Hao, M. C. Martin, A. Zettl, M. F. Crommie, Y. R. Shen, and F. Wang, Nat. Phys. **459**, 820 (2009).

[126] T. Ohta, A. Bostwick, T. Seyller, K. Horn, and E. Rotenberg, Science **313**, 951 (2006).

[127] F. Xia, D. B. Farmer, Y. Lin, and P. Avouris, Nano Lett. **10**, 715 (2010).

[128] M. Charbonneau, K. M. Van Vliet, and P. Vasilopoulos, J. Math. Phys. **23**, 318 (1982).

[129] A. Rycerz, J. Tworzydlo, and C. W. J. Beenakker, Nature Phys. **3**, 172 (2007).

[130] D. Xiao, W. Yao, and Q. Niu, Phys. Rev. Lett. **99**, 236809 (2007).

[131] A. M. Jones, H. Yu, J. S. Ross, P. Klement, N. J. Ghimire, J. Yan, D. G. Mandrus, W. Yao and X. Xu, Nat. Phys. **10**, 130 (2014).

[132] S. Fang, R. K. Defo, S. N. Shirodkar, S. Lieu, G. A. Tritsaris, and E. Kaxiras, Phys. Rev. B **92**, 205108 (2015).

[133] A. Kormányos, V. Zólyomi, N. D. Drummond, and G. Burkard, Phys. Rev. X **4**, 011034 (2014).

[134] D. MacNeill, C. Heikes, K. F. Mak, Z. Anderson, A. Kormányos, V. Zólyomi, J. Park, and D. C. Ralph, Phys. Rev. Lett. **114**, 037401 (2015).

[135] A. Srivastava, M. Sidler, A. V. Allain, D. S. Lembke, A. Kis, and A. Imamoglu, Nat. Phys. **11**, 141 (2015).

[136] G. Aivazian, Z. Gong, A. M. Jones, R.-L. Chu, J. Yan, D. G. Mandrus, C. Zhang, D. Cobden, W. Yao, and X. Xu, Nat. Phys. **11**, 148 (2015).

[137] Y. Li, J. Ludwig, T. Low, A. Chernikov, X. Cui, G. Arefe, Y. D. Kim, A. M. van der Zande, A. Rigosi, H. M. Hill, S. H. Kim, J. Hone, Z. Li, D. Smirnov, and T. F. Heinz, Phys. Rev. Lett. **113**, 266804 (2014).

[138] Y. C. Cheng, Q. Y. Zhang, and U. Schwingenschlögl, Phys. Rev. B **89**, 155429 (2014).

[139] M. Koshino and T. Ando, Phys. Rev. B **81**, 195431 (2010).

[140] T. Cheiwchanchamnangij and W. R. L. Lambrecht, Phys. Rev. B **85**, 205302 (2012).

[141] A. Kumar and P. K. Ahluwalia, Modelling Simul. Mater. Sci. Eng. **21**, 065015 (2013).

[142] W. Jin, P.-C. Yeh, N. Zaki, D. Zhang, J. T. Sadowski, A. Al-Mahboob, A. M. v. d. Zande, D. A. Chenet, J. I. Dadap, I. P. Herman, P. Sutter, J. Hone, and R. M. Osgood, Jr., Phys. Rev. Lett. **111**, 106801 (2013).

[143] P. Koskinen, I. Fampiou, and A. Ramasubramaniam, Phys. Rev. Lett. **112**, 186802 (2014).

[144] P. M. Krstajic and P. Vasilopoulos, Phys. Rev. B **83**, 075427 (2011); *ibid.* **86** 115432 (2012).

[145] M. Tahir, A. Manchon, and U. Schwingenschlögl, Phys. Rev. B **90**, 125438 (2014).

[146] X. F. Wang and P. Vasilopoulos, Phys. Rev. B **72**, 085344 (2005); *ibid.* **67**, 085313 (2003).

[147] I. Zutic, J. Fabian, and S. Das Sarma, Rev. Mod. Phys. **76**, 323 (2004).

[148] J. A. Wilson and A. D. Yoffe, Adv. Phys. **18**, 193 (1969).

[149] A. Enyashin, S. Gemming, and G. Seifert, Eur. Phys. J. Spec. Top. **149**, 103 (2007).

[150] M. Bar-Sadan, I. Kaplan-Ashiri, and R. Tenne, Eur. Phys. J. Spec. Top. **149**, 71 (2007).

[151] R. Tenne and C. N. R. Rao, Philos. Trans. R. Soc. London A **362**, 2099 (2004).

[152] M. Zuabir, M. Tahir, P. Vasilopoulos, and K. Sabeeh, Phys. Rev. B **96**, 045405 (2017).

[153] M. Tahir, P. M. Krstajić, and P. Vasilopoulos, Phys. Rev. B **98**, 075429 (2018).

[154] N. Ubrig, S. Jo, M. Philippi, D. Costanzo, H. Berger, A. B. Kuzmenko, and A. F. Morpurgo, Nano Letters **17** (9), 5719 (2017).

[155] R. Suzuki, M. Sakano, Y. J. Zhang, R. Akashi, D. Morikawa, A. Harasawa, K. Yaji, K. Kuroda, K. Miyamoto, T. Okuda, K. Ishizaka, R. Arita, and Y. Iwasa, Nature Nano **9**, 611 (2014).

[156] R. Akashi, M. Ochi, S. Bordács, R. Suzuki, Y. Tokura, Y. Iwasa, and R. Arita, Phys. Rev. Applied **4**, 014002 (2015).

[157] J. Yan, J. Xia, X. Wang, L. Liu, J.-L. Kuo, B. K. Tay, S. Chen, W. Zhou, Z. Liu, and Z. X. Shen, Nano Lett. **15**, 8155 (2015).

[158] J. He, K. Hummer, and C. Franchini, Phys. Rev. B **89**, 075409 (2014).

[159] T. Brumme, M. Calandra, and F. Mauri, Phys. Rev B **91**, 155436 (2015).

[160] M. Koshino and T. Ando, Phys. Rev. B **77**, 115313 (2008).

[161] Z. Li, and J. P. Carbotte, Phys. Rev. B **88**, 045414 (2013).

[162] C. J. Tabert and E. J. Nicol, Phys. Rev. B **88**, 085434 (2013).

[163] E. Illes and E. J. Nicol, Phys. Rev. B **94**, 125435 (2016).

[164] V. P. Gusynin, S. G. Sharapov, and J. P. Carbotte, J. Phys.: Condens. Matter **19**, 026222 (2007); Phys. Rev. Lett. **98**, 157402 (2007).

[165] P. E. C. Ashby and J. P. Carbotte, Phys. Rev. B **87**, 245131 (2013).

[166] A. H. Castro Neto, F. Guinea, N. M. R. Peres, K. S. Novoselov, and A. K. Geim, Rev. Mod. Phys. **81**, 109 (2009).

[167] N. Tombros, C. Jozsa, M. Popinciuc, H. T. Jonkman, and B. J. van Wees, Nature **448**, 571 (2007).

[168] J. Ingla-Aynés, M. H. D. Guimarães, R. J. Meijerink, P. J. Zomer, and B. J. van Wees, Phys. Rev. B **92**, 201410(R) (2015).

[169] M. Drögeler, C. Franzen, F. Volmer, T. Pohlmann, L. Banszerus, M. Wolter, K. Watanabe, T. Taniguchi, C. Stampfer, and B. Beschoten, Nano Lett. **16**, 3533 (2016).

[170] C. L. Kane and E. J. Mele, Phys. Rev. Lett. **95**, 226801 (2005); ,**95**, 146802 (2005).

[171] Z. Qiao, S. A. Yang, W. Feng, W.-K. Tse, J. Ding, Y. Yao, Y. Wang and Q. Niu, Phys. Rev. B **82**, 161414 (2010); C.-X. Liu, S.-C. Zhang and X.-L. Qi, Annu. Rev. Condens. Matter Phys. **7**, 301 (2016); Y. Ren, Z. Qiao and Q. Niu, Rep. Prog. Phys. **79**, 066501 (2016); H. Weng, R. Yu, X. Hu, X. Dai and Z. Fang, Adv. Phys. **64**, 227 (2015).

[172] A. H. C Neto, and F. Guinea, Phys. Rev. Lett. **103**, 026804 (2009).

[173] C. Weeks, J. Hu, J. Alicea, M. Franz and R. Wu, Phys. Rev. X **1**, 021001 (2011).

[174] J. Ding, Z. Qiao, W. Feng, Y. Yao and Q. Niu, Phys. Rev. B **84**, 195444 (2011).

[175] J. Hu, J. Alicea, R. Wu and M. Franz, Phys.Rev. Lett. **109**, 266801 (2012).

[176] D. Ma, Z. Li and Z. Yang, Carbon **50**, 297 (2012).

[177] K.-H. Jin and S.-H. Jhi, Phys. Rev. B **87**, 075442 (2013).

[178] A. Ferreira, T. G. Rappoport, M. A. Cazalilla and A. H. C. Neto, Phys. Rev. Lett. **112**, 066601 (2014).

[179] A. A. Kaverzin and B. J. van Wees, Phys. Rev. B **91**, 165412 (2015).

[180] J. Balakrishnan, G. K. W. Koon, M. Jaiswal, A. H. C. Neto and B. C. Ozyilmaz, Nat. Phys. **9**, 284 (2013).

[181] X. Hong, S.-H. Cheng, C. Herding, and J. Zhu, Phys. Rev. B **83**, 085410 (2011).

[182] Z. Jia, B. Yan, J. Niu, Q. Han, R. Zhu, D. Yu and X. Wu, Phys. Rev. B **91**, 085411 (2015).

[183] U. Chandni, E. A. Henriksen and J. P. Eisenstein, Phys. Rev. B **91**, 245402 (2015).

[184] Y.-C. Lin, N. Lu, N. Perea-Lopez, J. Li, Z. Lin, X. Peng, C. H. Lee, C. Sun, L. Calderin, P. N. Browning, M. S. Bresnehan, M. J. Kim, T. S. Mayer, M. Terrones, and J. A. Robinson, ACS Nano **8**, 3715 (2014).

[185] M.-Y. Lin, C.-E. Chang, C.-H. Wang, C.-F. Su, C. Chen, S.-C. Lee, and S.-Y. Lin, Appl. Phys. Lett. **105**, 073501 (2014).

[186] A. Azizi, S. Eichfeld, G. Geschwind, K. Zhang, B. Jiang, D. Mukherjee, L. Hossain, A. F. Piasecki, B. Kabius, J. A. Robinson, and Nasim Alem, ACS Nano **9**, 4882 (2015).

[187] Y. Kim, D. Choi, W. J. Woo, J. B. Lee, G. H. Ryu, J. H. Lim, S. Lee, Z. Lee, S. Im, J.-H. Ahn, W.-H. Kim, J. Park, and H. Kim, Appl. Surf. Sci. **494**, 591 (2019).

[188] A. M. Alsharari, M. M. Asmar, and S. E. Ulloa, Phys. Rev. B **98**, 195129 (2018).

[189] L. A. Benítez, J. F. Sierra, W. Savero Torres, A. Arrighi, F. Bonell, M. V. Costache, and S. O. Valenzuela, Nat. Phys. **14**, 303 (2018).

[190] A. W. Cummings, J. H. Garcia, J. Fabian, and S. Roche, Phys. Rev. Lett. **119**, 206601 (2017).

[191] W. Han, R. K. Kawakami, M. Gmitra, and J. Fabian, Nat. Nanotechnol. **9**, 794 (2014).

[192] A. Kormányos, G. Burkard, M. Gmitra, J. Fabian, V. Zólyomi, N. D. Drummond, and V. Falḱo, 2D Mater. **2**, 022001 (2015).

[193] C.-P. Lu, G. Li, K. Watanabe, T. Taniguchi, and E. Y. Andrei, Phys. Rev. Lett. **113**, 156804 (2014).

[194] S. Larentis, J. R. Tolsma, B. Fallahazad, D. C. Dillen, K. Kim, A. H. MacDonald, and E. Tutuc, Nano Lett. **14**, 2039 (2014).

[195] L. Banszerus,T. Sohier, A. Epping,F. Winkler, F. Libisch, F. Haupt, K. Watanabe, T. Taniguchi, K. Muller-Caspary, N. Marzari, F. Mauri, B. Beschoten, and C. Stampfer, arXiv: 1909.09523.

[196] S. Bertolazzi, D. Krasnozhon, and A. Kis, ACS Nano **7**, 3246 (2013).

[197] W. Zhang, C.-P. Chuu, J.-K. Huang, C.-H. Chen, M.-L. Tsai, Y.-H. Chang, C.-T. Liang, Y.-Z. Chen, Y.-L. Chueh, J.-H. He, M.-Y. Chou, and L.-J. Li, Sci. Rep. **4**, 3826 (2014).

[198] N. A. Kumar, M. A. Dar, R. Gul, and J. Baek, Mater. Today **18**, 286 (2015).

[199] A. David, P. Rakyta, A. Kormányos, and Guido Burkard, Phys. Rev. B **100**, 085412 (2019).

[200] Y. Li and M. Koshino, Phys. Rev. B **99**, 075438 (2019).

[201] A. Avsar, J. Y. Tan, T. Taychatanapat, J. Balakrishnan, G. K. W. Koon, Y. Yeo, J. Lahiri, A. Carvalho, A. S. Rodin, E. C. T. O'Farrell, G. Eda, A. H. Castro Neto, and B. Özyilmaz, Nat. Commun. **5**, 4875 (2014).

[202] M. Gmitra, S. Konschuh, C. Ertler, C. Ambrosch-Draxl, and J. Fabian, Phys. Rev. B **80**, 235431 (2009).

[203] C. K. Safeer, J. Ingla-Aynés, F. Herling, J. H. Garcia, M. Vila, N. Ontoso, M. Reyes Calvo, S. Roche, L. E. Hueso, and F. Casanova, Nano Lett. 19, 1074 (2019).

[204] B. Yang, M.-F. Tu, J. Kim, Y. Wu, H. Wang, J. Alicea, R. Wu, M. Bockrath and J. Shi, 2D Mater. **3**, 031012 (2016).

[205] S. Zihlmann, A. W. Cummings, J. H. Garcia, M. Kedves, K. Watanabe, T. Taniguchi, C. Schonenberger, and P. Makk, Phys. Rev. B **97**, 075434(R) (2018).

[206] Z. Wang, D. K. Ki, H. Chen, H. Berger, A. H. MacDonald, and A. F. Morpurgo, Nat. Commun. **6**, 8339 (2015).

[207] Jose H. Garcia, Marc Vila, Aron W. Cummings, and Stephan Roche, Chem. Soc. Rev. **47**, 3359 (2018); A. Mreńca-Kolasińska, B. Rzeszotarski, and B. Szafran, Phys. Rev. B **98**, 045406 (2018).

[208] T. Völkl, T. Rockinger, M. Drienovsky, K. Watanabe, T. Taniguchi, D. Weiss, and J. Eroms, Phys. Rev. B **96**, 125405 (2017); B. Yang, E. Molina, J. Kim, D. Barroso, M. Lohmann, Y. Liu, Y. Xu, R. Wu, L. Bartels, K. Watanabe, T. Taniguchi, and Jing Shi, Nano Lett. **18**, 3580 (2018).

[209] M. Gmitra, D. Kochan, P. Högl, and J. Fabian, Phys. Rev. B **93**, 155104 (2016).

[210] M. Gmitra and J. Fabian, Phys. Rev. B **92**, 155403 (2015).

[211] M. Gmitra, D. Kochan, and J. Fabian, Phys. Rev. Lett. **110**, 246602 (2013).

[212] Z. Wang, D.-K. Ki, J. Y. Khoo, D. Mauro, H. Berger, L. S. Levitov, and A. F. Morpurgo, Phys. Rev. X **6**, 041020 (2016).

[213] Z. Li and J. P. Carbotte, Phys. Rev. B **86**, 205425 (2012).

[214] V. P. Gusynin, S. G. Sharapov, and J. P. Carbotte, Phys. Rev. Lett. **96**, 256802 (2006).

[215] V. Vargiamidis, P. Vasilopoulos and G-Q. Hai, J. Phys.: Condens. Matter **26**, 345303 (2014); V. Vargiamidis, and P. Vasilopoulos, J. Appl. Phys. **116**, 063713 (2014).

[216] D. S. L. Abergel and V. I. Fal´ko, Phys. Rev. B **75**, 155430 (2007).

[217] E. J. Nicol and J. P. Carbotte, Phys. Rev. B **77**, 155409 (2008).

[218] T. Stauber, N. M. R. Peres, and F. Guinea, Phys. Rev. B **76**, 205423 (2007).

[219] K. Nomura and A. H. MacDonald, Phys. Rev. Lett. **98**, 076602 (2007).

[220] A. A. Patel and S. Mukerjee, Phys. Rev. B **86**, 075411 (2012).

[221] J. Sichau, M. Prada, T. Anlauf, T. J. Lyon, B. Bosnjak, L. Tiemann, and R. H. Blick, Phys. Rev. Lett. **122**, 046403 (2019).

[222] T. Völkl, T. Rockinger, M. Drienovsky, K. Watanabe, T. Taniguchi, D.Weiss, and J. Eroms, Phys. Rev. B **96**, 125405 (2017).

[223] S. Omar and B. J. van Wees, Phys. Rev. B **95**, 081404(R) (2017).

[224] A. Dankert and S. P. Dash, Nat. Commun. **8**, 16093 (2017).

[225] M. Offidani, M. Milletarì, R. Raimondi, and A. Ferreira, Phys. Rev. Lett. **119**, 196801 (2017).

[226] S. Zihlmann, A. W. Cummings, J. H. Garcia, M. Kedves, K. Watanabe, T. Taniguchi, C. Schönenberger, and P. Makk, Phys. Rev. B **97**, 075434 (2018).

[227] J. H. Garcia, M. Vila, A. W. Cummings, and S. Roche, Chem. Soc. Rev. **47**, 3359 (2018).

[228] T. S. Ghiasi, J. Ingla-Aynés, A. A. Kaverzin, and B. J. van Wees, Nano Lett. **17**, 7528 (2017).

[229] D. Kochan, S. Irmer, and J. Fabian, Phys. Rev. B **95**, 165415 (2017).

[230] D. N. Basov, R. D. Averitt, and D. Hsieh, Nat. Mater. **16**, 1077 (2017).

[231] F. Krausz and M. I. Stockman, Nat. Photon. **8**, 205 (2014).

[232] D. Fausti, R. I. Tobey, N. Dean, S. Kaiser, A. Dienst, M. C. Hoffmann, S. Pyon, T. Takayama, H. Takagi, and A. Cavalleri, Science **331**, 189 (2011).

[233] M.Mitrano, A. Cantaluppi, D. Nicoletti, S. Kaiser, A. Perucchi, S. Lupi, P. Di Pietro, D. Pontiroli, M. Riccó, S. R. Clark, D. Jaksch, and A. Cavalleri, Nature **530**, 461 (2016).

[234] M. Rini, A. Cavalleri, R. W. Schoenlein, R. López, L. C. Feldman, R. F. Haglund, L. A. Boatner, and T. E. Haynes, Opt. Lett. **30**, 558 (2005).

[235] M. Liu, H. Y. Hwang, H. Tao, A. C. Strikwerda, K. Fan, G. R. Keiser, A. J. Sternbach, K. G. West, S. Kittiwatanakul, J. Lu, S. A. Wolf, F. G. Omenetto, X. Zhang, K. A. Nelson, and R. D. Averitt, Nature **487**, 345 (2012).

[236] E. Pomarico, M. Mitrano, H. Bromberger, M. A. Sentef, A. Al-Temimy, C. Coletti, A. Stöhr, S. Link, U. Starke, C. Cacho, R. Chapman, E. Springate, A. Cavalleri, and I. Gierz, Phys. Rev. B **95**, 024304 (2017).

[237] D. M. Kennes, E. Y. Wilner, D. R. Reichman, and A. J. Millis, Nat. Phys. **13**, 479 (2017).

[238] M. A. Sentef, Phys. Rev. B **95**, 205111 (2017).

[239] T. Oka and H. Aoki, Phys. Rev. B **79**, 081406(R) (2009).

[240] T. Kitagawa, T. Oka, A. Brataas, L. Fu, and E. Demler, Phys. Rev. B **84**, 235108 (2011).

[241] N. H. Lindner, G. Refael, and V. Galitski, Nat. Phys. **7**, 490 (2011).

[242] M. A. Sentef, M. Claassen, A. F. Kemper, B. Moritz, T. Oka, J. K. Freericks, and T. P. Devereaux, Nat. Commun. **6**, 7047 (2015).

[243] H. Hübener, M. A. Sentef, U. De Giovannini, A. F. Kemper, and A. Rubio, Nat. Commun. **8**, 13940 (2017).

[244] Y. H. Wang, H. Steinberg, P. Jarillo-Herrero, and N. Gedik, Science **342**, 453 (2013).

[245] F. Mahmood, C.-K. Chan, Z. Alpichshev, D. Gardner, Y. Lee, P. A. Lee, and N. Gedik, Nat. Phys. **12**, 306 (2016).

[246] H. Miyake, G. A. Siviloglou, C. J. Kennedy, W. C. Burton, and W. Ketterle, Phys. Rev. Lett. **111**, 185302 (2013).

[247] N. Fläschner, B. S. Rem, M. Tarnowski, D. Vogel, D.-S. Lühmann, K. Sengstock, and C.Weitenberg, Science **352**, 1091 (2016).

[248] M. C. Rechtsman, J. M. Zeuner, Y. Plotnik, Y. Lumer, D. Podolsky, F. Dreisow, S. Nolte, M. Segev, and A. Szameit, Nature **496**, 196 (2013).

[249] M. Aidelsburger, S. Nascimbene, and N. Goldman, C. R. Phys. **19**, 394 (2018).

[250] T. Ozawa, H. M. Price, A. Amo, N. Goldman, M. Hafezi, L. Lu, M. Rechtsman, D. Schuster, J. Simon, O. Zilberberg, and I. Carusotto, Rev. Mod. Phys. **91**, 015006 (2019).

[251] L. Asteria, D. T. Tran, T. Ozawa, M. Tarnowski, B. S. Rem, N. Fläschner, K. Sengstock, N. Goldman, and C. Weitenberg, Nat. Phys. **15**, 449 (2019).

[252] J. W. McIver, B. Schulte, F.-U. Stein, T. Matsuyama, G. Jotzu, G. Meier, and A. Cavalleri, Nat. Phys. **16**, 38 (2020).

[253] S. A. Sato, J. W. McIver, M. Nuske, P. Tang, G. Jotzu, B. Schulte, H. Hübener, U. De Giovannini, L. Mathey, M. A. Sentef, A. Cavalleri, and A. Rubio, Phys. Rev. B **99**, 214302 (2019).

[254] M. Bukov, L. D'Alessio, and A. Polkovnikov, Adv. Phys. **64**, 139 (2015).

[255] L. E. F. Foa Torres, P. M. Perez-Piskunow, C. A. Balseiro, and G. Usaj, Phys. Rev. Lett. **113**, 266801 (2014).

[256] G. Usaj, P. M. Perez-Piskunow, L. E. F. Foa Torres, and C. A. Balseiro, Phys. Rev. B **90**, 115423 (2014).

[257] H. Dehghani, T. Oka, and A. Mitra, Phys. Rev. B **90**, 195429 (2014).

[258] A. Kundu, H. A. Fertig, and B. Seradjeh, Phys. Rev. Lett. **113**, 236803 (2014).

[259] Takahiro Mikami, Sota Kitamura, Kenji Yasuda, Naoto Tsuji, Takashi Oka, and Hideo Aoki, Phys. Rev. B **93**, 144307 (2016).

[260] M. Tahir and P. Vasilopoulos, Phys. Rev. B **91**, 115311 (2015).

[261] C. J. Tabert and E. J. Nicol, Phys. Rev. B **87**, 235426 (2013).

[262] A. Kormanyos *et al.*, Phys. Rev. B **90**, 125438 (2014).

[263] C. J. Tabert *et al.*, Phys. Rev. Lett. **110**, 197402 (2013).

[264] Kh. Shakouri *et al.*, Phys. Rev. B **90**, 235423 (2014).

[265] L. Brey and H. A. Fertig,Phys. Rev. B **75**, 125434 (2007); H. Zheng, Z. F. Wang, Tao Luo, Q. W. Shi, and J. Chen, *ibid.* **75**, 044710 (2011).

[266] K.-I. Sakaki, K. Wakabayashi, and T. Enoki, J. Phys. Soc. Jpn. **80**, 044710 (2011); M.-F. Lin and F.-L. Shyu, *ibid.* **69**, 3529 (2000); K. Gundra and A. Shukla, Phys. Rev. B **83**, 075413 (2011).

[267] Ken-ichi Sasaki, K. Kato, Y. Tokura, K. Oguri, and T. Sogawa, Phys. Rev. B **84**, 085458 (2011).

[268] L. Brey and H. A. Fertig, Phys. Rev. B **73**, 235411 (2006); K. O. Wedel, N. A. Mortensen, K. S. Thygesen, and M. Wubs, Phys. Rev. Lett. **98**, 155412 (2018); M. Bahrami and P. Vasilopoulos, Optics Express **25**, 16840 (2017).

[269] Y. Ominato and M. Koshino, Phys. Rev. B **85**, 165454 (2012); Solid State Commun. **175-176**, 51 (2013).

[270] J. Liu, Z. Ma, A. R. Wright, and C. Zhang, J. Appl. Phys. **103**, 103711 (2008).

[271] Li Yang, M. L. Cohen, and S. G. Louie, Nano Lett. **7**, 3112 (2007).

[272] K. Wakabayashi, Y. Takane, M. Yamamoto, and M. Sigrist, New J. Phys. **11**, 095016 (2009).

[273] Thomas Aktor, Antti-Pekka Jauho, and Stephen R. Power, Phys. Rev. B **33**, 035446 (2016); J. Guo, D. Gunlycke, and C. T. White, Appl. Phys. Lett. **92**, 163109 (2008); P. Hawkins, M. Begliarbekov, M. Zivkovic, S. Strauf, and C. P. Search, J. Phys. Chem. C **116**, 18382 (2012).

[274] J. Lan, J.-S. Wang, C. K. Gan, and S. K. Chin, Phys. Rev. B **79**, 115401 (2009); Ming-Xing Zhai and Xue-Feng Wang, Sci. Rep. **6**, 36762 (2016).

[275] Ting-Ting Wu, Xue-Feng Wang, Ming-Xing Zhai, Hua Liu, Liping Zhou, and Yong-Jin Jiang, Appl. Phys. Lett. **100**, 052112 (2012).

[276] O. Grning, S. Wang, X. Yao, C. A. Pignedoli, G. B. Barin, C. Daniels, A. Cupo, V. Meunier, X. Feng, A. Narita, K. Múllen, P. Ruffieux, and R. Fasel, Nature **560**, 209 (2018); G. Z. Magda, X. Jin, I. Hagymasi, P. Vancso, Z. Osvath, P. Nemes-Incze, C. Hwang, L. P. Biro, and L. Tapaszto, Nature **514**, 608 (2014); M. Y. Han, J. C. Brant, and P. Kim, Phys. Rev. Lett. **104**, 056801 (2010).

[277] S. Zhang, R. Liang, E. Zhang, L. Zhang, and Y. Liu, Phys. Rev. B **73**, 155316 (2006).

[278] P. Vasilopoulos and F.M. Peeters, Phys. Rev. B **40**, 10079 (1989).

[279] V. Ryzhii, M Ryzhii, N. Ryabova, V. Mitin, and T. Otsuji, Jpn. J. Appl. Phys. **48**, 04C144 (2009).

[280] Y. H. Wang, H. Steinberg, P. jarillo-Herrero, and N. Gedik, science **342**, 453 (2013).

[281] H. C. Po, L. Zou, A. Vishwanath, and T. Senthil, Phys. Rev. X **8**, 031089 (2018).